Evolution of Mercury's Volatile-Bearing Crust within Raditladi Basin

Deborah Domingue[1], John Weirich[1], Alexis Rodriguez[2], Samuel Corville[1,3], Frank Chuang[1], Matthew Richardson[1], Bryan Travis[1], Eric Palmer[1], Mario Zarroca[4]

[1]Planetary Science Institute, 1700 E. Fort Lowell, Suite 106, Tucson, AZ 85719-2395, USA, [2]Marshall Space Flight Center, Huntsville AL 35812, USA,
[3]Arizona State University, School of Earth and Space Exploration, 781 Terrace Mall, Tempe, AZ 85287, USA
[4]External Geodynamics and Hydrogeology Group, Department of Geology, Autonomous University of Barcelona, E-08193 Bellaterra, Barcelona, Spain

Abstract

Mercury's surface presents significant challenges for understanding planetary volatile distribution. Previous studies have identified features including hollows, flows, and chaotic terrains as associated with the presence of volatiles. Their formation and connection to Mercury's volatile inventory remain incompletely characterized. Using Hapke's radiative transfer model, we conducted detailed photometric analyses of three distinct regions within Mercury's Raditladi Basin, that display hollows and flow-like morphologies, to quantify regolith properties and their relationship to volatile-driven processes, revealing three key findings: (1) The basin floor regolith exhibits distinct structural characteristics indicating a separate evolutionary pathway. (2) Hollows and surrounding halos demonstrate regolith properties (higher porosity, finer-grained) consistent with slow, low-energy sublimation processes that minimally disrupt inter-grain relationships. (3) Areas within the peak ring display photometric signatures indicative of volatile-rich mass wasting flows. The hollows and halos exhibit significantly higher single scattering albedo compared to other units, suggesting the presence of a unique residual material that remains after volatile sublimation that appears intimately mixed with common regolith components. Previously mapped flow-like features share regolith structural similarities with hollows supporting their derivation from a common volatile-rich layer (VRL). Regions along peak walls display distinctive photometric properties that likely represent remnants of VRL flow sources within the peak ring structure, suggesting that peak rings maintained their volatile composition throughout the flow process. The excavation of hollows-like regolith from impacts on the basin floor suggest either differentiation of the impact melt or burial of volatiles outgassed from the peak ring, deposited on the basin floor, and later buried.

Introduction

There is continually emerging evidence that Mercury is a volatile-rich planet, beginning with the detection of volatile elements, such as sodium (Na), chloride (Cl) (Evans et al. 2015), potassium (K) (Peplowski et al. 2012; Nittler et al. 2018), and sulfur (S) (Nittler et la. 2011; Evans et al. 2012) within the upper few centimeters to meters of the crust. Comparisons of K/Th and Cl/K ratios show Mercury has a volatile content similar to Mars and is enriched compared to Earth and Venus (e.g., Nittler and Weider 2019). For example, Mercury's surface sulfur content (~4 wt%) is an order of magnitude greater than the <0.1 wt% of Earth's crustal sulfur content (e.g., Nittler and Weider 2019). Geologic landforms associated with volatiles include hollows (Blewett et al. 2011, 2013, 2016, 2018; Thomas et al. 2014a, 2016; Barraud et al. 2020, 2023; De Toffoli et al. 2024), pyroclastic volcanic vents (Strom et al. 1975; Head et al. 2008; Goudge et al. 2014;

Rothery et al., 2014; 2021; Thomas et al. 2014b; Besse et al., 2015, 2020; Weider et al. 2016; Byrne et al. 2018; Jozwiak et al., 2018; Barraud et al. 2021; Pegg e t al. 2021; Galiano et al. 2022; Leon-Dasi et al. 2025), chaotic terrains (Rodriguez et al. 2020), and glacier-like flow features (labeled such by Rodriguez et al. (2023) due to their morphological structures); all indicating a volatile-rich reservoir at depth within the upper kilometers of the crust. Investigations of these geologic features show that Mercury has had a complex history of volatilization and volatile removal that spans billions of years and has had a role in shaping the surface morphology.

The presence of hollows (sublimation pits) implies that near-surface volatility still exists on Mercury and may be recently (<300Ma) active (Blewett et al. 2018). Examination of the surface for temporal changes over the course of the MESSENGER mission shows two hollows were active during the mission's time span (Speyerer et al. 2022). The hollows in Raditladi basin are considered some of the youngest of these hollows features (Blewett et al. 2018). Hollows are irregular, rimless, flat-floored, shallow depressions characterized by a blue spectral slope signature and often display high-reflectance halos and interiors (Blewett et al. 2018). Their occurrence within rayed craters, crisp morphology, associated fine structures, and lack of superposed craters all point to this young age (Blewett et al. 2016, 2018). They are found predominantly in terrains (spectral color units) with lower-than-average reflectance properties, such as low reflectance material (LRM), low-reflectance blue plains (LBP), and dark spots (Weider et al 2015; Blewett et al. Thomas et al. 2014; Denevi et al. 2016a); suggesting a link to the presence of carbon (Klima et al. 2018). However, more recent studies of the distribution of hollows, as a function of their developmental stage, demonstrate that they are not exclusive to LRM; only 5 – 7% are found in LRM (Deutsch et al. 2025; Bickel et al. 2025) and thus their connection to carbon is not a required characteristic for their formation. They are sometimes associated with pyroclastic deposits (Blewett et al. 2011, 2013, 2018; Barraud et al. 2020). Hollows predominantly occur within the interiors of impact craters or associated with impact generated terrains (Thomas et al. 2014, Deutsch et al. 2025). These geologically young features hold evidence for a poorly understood history of volatile loss, movement, and deposition on Mercury.

The formation hypotheses for hollows are all based on the existence of a volatile-rich layer (VRL) which is exposed to the surface, predominately by impact cratering. The formation of the VRL varies between hypotheses, where one formation theory suggests magmatic gasses and fumarolic minerals from eruptions condensed on low-temperature nightside surfaces, infilling pre-existing fractures which were subsequently covered and stabilized beneath volcanic flows (Blewett et al. 2011, 2013; Phillips et al. 2021). One variation of this hypothesis is similar to the formation of thermokarst landscapes, where sulfur-rich gases generated in fumarolic systems form patchy sulfur-rich layers at night that are subsequently exposed during the day to form hollows (Phillips et al. 2021; Lucchetti et al. 2021). Another formation hypothesis suggests the VRL is an inherent component of the upper crust (Blewett et al. 2013; Rodriguez et al. 2020). The former hypothesis suggests localized sources of the VRL, while the latter opens the possibility that the VRL is nearly-global in extent. Each implies a different compositional and evolutionary history for the crust and its volatile inventory during formation. Recent morphologic studies of hollows and glacier-like flows within Raditladi basin (Rodriguez et al. 2023), Borealis Chaos (Rodriguez et al. 2023) and the chaotic terrain antipodal to Caloris basin (Rodriguez et al. 2020), and impact craters within Praxiteles Basin (Galiano et al. 2024) provide evidence for a VRL that is wide-spread and present at multiple locations across the surface.

All these geologic features are the result of the removal and loss of a volatile phase, leaving behind the less volatile components of the VRL. The composition and source of the volatiles is

highly debated within the literature, with the majority of the evidence derived from MESSENGER's Mercury Dual Imaging System (MDIS), since the camera was able to spatially resolve these features.

Based on MDIS color spectra the volatiles are thought to potentially be sulfides (Vilas et al., 2016; Lucchetti et al., 2018 2021, Phillips et al. 2021; Barraud et al., 2023) and chlorides (Lucchetti et al. 2021, Rodriguez et al. 2023), whereas the residuals after devolatilization are speculated to contain carbon (Klima et al., 2018; Galliano et al. 2024). However, recent examination of the distribution of hollows compared to spectral color units show they are not bound to the high carbon units (Deutsche et al. 2025). Examination of hollows within Velazquez, Canova, and Dominici craters have shown possible detection of sulfides (Vilas et al., 2016; Lucchetti et al., 2018), but with the caveat that they are mixed with local bedrock-forming minerals indicative of pyroxenes with transitional elements (Cr, Ti, Ni) substituting for Mg and Fe (Lucchettie et al. 2018, 2021; Pajola et al. 2021). More recent studies of Tyagaraja and Raditladi basins, show that the composition of the volatile material may vary (Barraud et al. 2020; Lucchetti et al. 2021; Rodriguez et al. 2023).

Comparing the spectral properties of hollows and pyroclastic deposits within Tyagaraja crater, Lucchetti et al. (2021) showed that the hollows are better represented by chloride minerals and the pyroclastics are better represented by sulfides. The proposed scenario is that a localized VRL could be created by the differentiation of impact melt enriched in sulfides and chlorides (Vaughan et al. 2012; Lucchetti et al. 2021). The reduction of anhydrous chlorine-rich mafic melts would produce chlorides (Carroll and Webster 1994) which could unmix from the chlorine-saturated silicate melts to form a chloride-rich flotation crust as the VRL; which subsequently devolatilized during hollows formation (Vaughan et al. 2012; Lucchetti et al. 2021). Sodalite ($Na_8(Al_6Si_6O_{24})Cl_2$) and halite (NaCl), along with magnesium and calcium chlorides ($MgCl_2$, CaCl, respectively) are consistent with the spectral properties of the hollows in Tyagaraja crater. Halite and elemental sulfur were proposed by Rodriguez et al. (2023) for the VRL responsible for the glacier-like flows in Raditladi, as its rheology under Mercury's environmental conditions could produce these features. Phillips et al. (2021) demonstrated that stearic acid ($C18H36O2$), fullerenes (C_{60}, C_{70}), and elemental sulfur (S_8) have the appropriate thermophysical properties to explain hollow formation, where, considering planetary formation mechanism, make sulfur the most plausible candidate.

It should be noted that all these studies are of the color spectral properties of the regolith after volatile removal. The physical and optical characteristics of the regolith left behind (the lag or refractory deposit) provides some of the few constraints on the devolatilization process and the properties inherent to the VRL. In this manuscript we examine the regolith properties of a subset of the regions with hollows in Raditladi basin that have been associated with glacier-like flow (Rodriguez et al. 2023). The hollows in these regions are associated with the basin's peak ring and the flow-like features that emanate from them. The hypothesis is that these flows originated from a VRL that was excavated by the formation of the basin, exposed in the peak ring formation, and subsequently flowed to form the morphology evident today (Rodriguez et al. 2023). The hollows formed on these flows as a result of sublimation of the volatile materials. These are the remnants of the VRL excavated by the formation of Raditladi basin.

In the following sections this manuscript reviews the geologic history of Raditladi basin, as it pertains to hollows development, the data set used to examine the regolith properties associated with a subset of the hollows units within the flow-like features, the modeling techniques used to derive the regolith characteristics, and a discussion of the derived regolith properties and their

implications for the processes involved in forming the hollows and the properties of the VRL associated with their presence.

Raditladi Basin

Raditladi basin could be as young as 1Ga or less (Strom et al. 2008; Prockter et al. 2010), which places it in the Mansurian period (Marchi et al. 2009; Denevi et al. 2016b). The inner plains of the basin are estimated to be about the same age as the basin (Marchi et al. 2011). Finite element models of the graben at the center of the basin suggest that the smooth plains are volcanic in origin (Blair et al. 2013) and their emplacement may have been triggered by the impact (Marchi et al. 2011). Thus, heat sources within the basin include both impact melt and volcanic flows.

Rodriguez et al. (2023) examined hollows within the Raditladi basin (**Figure 1**), and provided detailed examination of distinct hollows clusters that occur within its peak ring and adjacent lobate depositional aprons. These aprons show a cross-sectional morphology that exhibits convex upward forms terminating abruptly into steep ends, running out to distances of tens of kilometers from the peak ring scarps and, in some instances, superimposing extensional features along the adjacent crater floor (Rodriguez et al. 2023; Areas II and III in **Figure 1**). The hollows within these aprons have depths that are a significant fraction of the apron's thickness – up to one third (Rodriguez et al. 2023). The morphology of the aprons, along with the depths of the hollows within them, suggest a glacier-like emplacement originating from the flow of exposed VRLs associated with the formation of the peak ring (Rodriguez et al. 2023).

Clusters of hollows are also visible on and along the peak ring, with some merging to form relatively flat areas within the peak ring (Area I in **Figure 1**). The flat ridge tops on the peak rings, or mesas, suggest a demarcation separating volatile-rich materials from nonvolatile rocks, where the volatile materials may have flowed from the peaks to form the aprons (Rodriguez et al. 2023). Key to the preservation of the aprons is the development of a refractory lag capable of arresting or significantly slowing the devolatilization (Rodriguez et al. 2023).

Variations in the regolith structure along these aprons and peak rings are linked to the processes that have produced them and their modification history. Regolith structure refers to both the relationships between regolith grains (inter-grain structures) and the structures within the grains (granular structures). Inter-grain structures include compaction/porosity and photometric surface roughness. Photometric surface roughness is defined as the average surface tilt over the size range of a few grain diameters to the footprint resolution of the detector. For the lunar surface this is dominated by the centimeter scale (Helfenstein and Shepard 1999), but the dominating scale on Mercury's surface, which is much more processed by impacts (Cintala 1992), could be smaller. Granular structures include grain size and scattering behavior. The scattering behavior is governed by grain shape, opacity, changes in crystallinity, and inclusions (other grains, bubbles, cracks) – essentially any property that can change refractive indices within the grain. Variations in compaction can provide indicators for ongoing devolatilization (such as more porous regolith continues to provide escape pathways). Correlations of photometric surface roughness with morphology provide markers for fine-grained deposits, mass-wasting, and collapse. Changes in grain structures (including size and scattering behavior) provide boundaries for processing, such as maturity due to exposure to space weathering. The areas mapped by Rodriguez et al. (2023), shown in **Figure 1**, are examined using Hapke's radiative transfer model equations (e.g., Hapke 2012a) to examine the regolith structure to provide insight into the production and modification history of not only the hollows, but the complex morphology of the peak ring and glacier-like flows, thereby providing additional constraints on the VRL exposed during the basin formation.

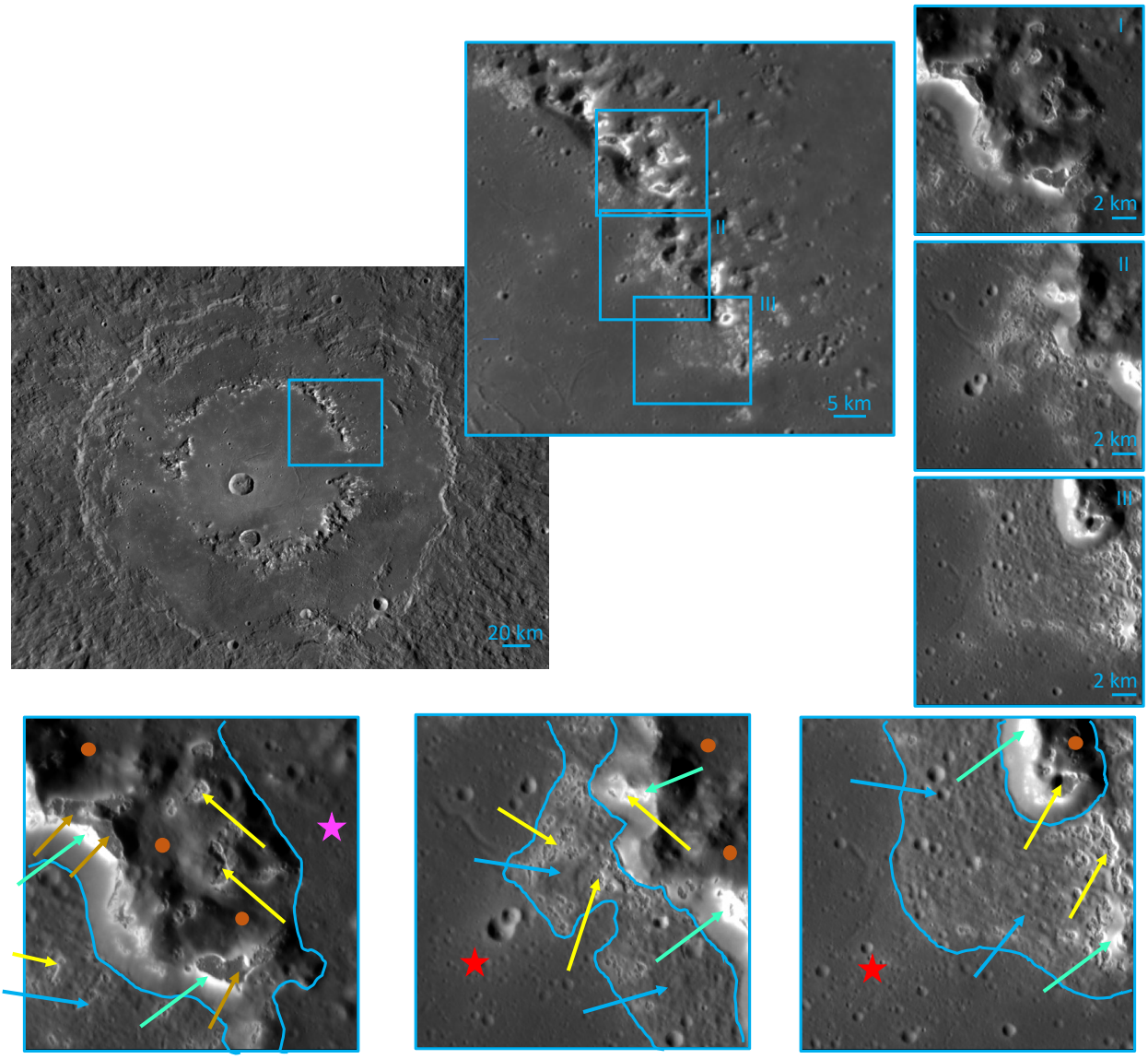

Figure 1. (top) Location of the hollows regions examined in Raditladi Basin. These are a subset of the regions examined by Rodriguez et al. (2023) that display hollows within glacier-like flows associated with the basin's peak-ring. (bottom) Identification of different morphological features within Areas I, II, and III (left to right). Blue lines identify the boundaries between the flow-like features, the basin floor, and the peak ring structures. The red stars identify the basin floor interior and the magenta star identifies the basin floor outside of the peak ring structure. Blue arrows identify the flow-like feature, yellow arrows identify hollows, and blue-green arrows identify halos. Brown arrows identify mesa tops (these are occupied by hollows features) and brown circles identify inter-peak terrains within the peak ring structure.

Photometric Data Set

Photometric data cubes for the three hollows areas (**Fig. 1**) were constructed using the methods described in Domingue et al. (2023, 2024), using the techniques of stereophotoclinometry (SPC).

All images were tied to the digital terrain models (DTMs) of these regions constructed for the study by Rodriguez et al. (2023). The result is a set of image cubes (photometric cubes) where the same sample and line in each image corresponds to the same physical location on the surface. The first plane in the image cube is the reflectance and the subsequent planes are the corresponding incidence, emission, and phase angle values that account for topography. A summary of the image data is provided in **Tables A1 – A3** in the Appendix, where a corresponding photometric cube was constructed for each image listed.

Each area was modeled individually. The photometric data cubes for each region were sampled into area bins measuring 10 x 10 pixels, where pixels are the discrete locations defined by line and sample in the photometric cubes. A pixel within a photometric cube that is located within a given 10 x 10 area bin contributes a 'data point' to that bin's data set. A 'data point' is the reflectance, incidence angle, emission angle, and phase angle values. For example, if two images cover the entire area of a given bin, then they each contribute 100 data points (one data point for each pixel in the 10 x 10 pixel bin) for modeling that specific area. Each bin was independently modeled. This follows the techniques described by Domingue et al. (2023, 2024). We do this to constrain computation time while keeping the highest spatial resolution that provides a broad range in angle values.

The range of photometric angles (incidence, emission, and phase angles) covered by the data set determines how well the model solutions can be constrained. To examine the quality of the data coverage, different regimes within the photometric angle values were defined. These include two opposition regimes, a near-opposition regime, a backward scattering regime, and a forward scattering regime. Each is defined by phase angle (α) values. The coherent-backscatter regime includes observations acquired at $\alpha \leq 2^{o}$ and the overlapping shadow-hiding regime includes observations acquired at $\alpha \leq 5^{o}$. The near-opposition, backward scattering, and forward scattering regimes are defined by $5^{o} < \alpha \leq 20^{o}$, $20^{o} < \alpha \leq 90^{o}$, and $90^{o} < \alpha \leq 180^{o}$, respectively. For each 10 x 10 pixel bin, the number of data points in each photometric regime was counted (See **Figure A1** in Appendix). The MDIS imaging data only contained observations in the backward and forward scattering regimes for all three sites. Following the methodology of Domingue et al. (2023, 2024), the quality of the data coverage in the incidence and emission angle values was examined (See **Figures A2 – A4**). Variations in parameter values associated with data coverage are apparent in Area II (see Photometric Modeling Results) associated with differences in coverage in the forward scattering direction.

Modeling Approach and Methodology

The Hapke model set of equations were used to model the photometric data for each of the hollows areas in Raditladi basin. The data sets contain no observations in either of the opposition regimes, thus the coherent backscatter opposition parameters are set to zero (as there are no published values for the global properties for these parameters), and the shadow hiding opposition parameters are set to the values from the analysis of a global dataset derived by Domingue et al. (2015), with B_s = 3.086 and h_s = 0.09. The resulting form of the Hapke model equation applied to these data sets is thus given by

$$\frac{I}{F} = \frac{w}{4\pi}\frac{\mu_{0e}}{\mu_{0e}+\mu_e}\left\{\left[p(\alpha)[1 + B_{S0}B_S(\alpha)]\right] + [H(\mu_{0e})H(\mu_e) - 1]\right\}S\left(i, e, \alpha, \overline{\theta}\right) \quad \text{Eq(1)},$$

where I/F is the ratio of reflected to incidence sunlight, w is the single scattering albedo, $\overline{\theta}$ is the surface roughness, α is the phase angle, $p(\alpha)$ is the single particle scattering function, B_{S0} is the shadow-hiding opposition effect amplitude and the term B_S is given by

$$B_S(\alpha) = \left[1 + \frac{1}{h_s} tan\left(\frac{\alpha}{2}\right)\right]^{-1} \quad \text{Eq(2),}$$

where h_s is the width of the shadow-hiding opposition peak. $S(i,e,\alpha,)$ is the surface roughness term, and μ_{0e} and μ_e are the modified cosines of the incidence (i) and emission (e) angles (see Hapke 1984), respectively, which account for changes in the surface tilt due to roughness. In this formalism, surface roughness is a 'photometric surface roughness', which is the average surface tilt from a few grain diameters to the pixel footprint as expressed within the upper few micrometers of the regolith. The $H(x)$ terms are the Chandrasehkar H-functions. The mathematical expression of these terms, and their derivation, can be found in Hapke (1981, 1984, 1986, 1993, 2002, 2008, 2012a).

A Henyey-Greenstein function is used for the single particle scattering function, $p(\alpha)$, given by:

$$p(\alpha) = \frac{(1-c)(1-b^2)}{(1-2bcos(\alpha)+b^2)^{\frac{3}{2}}} + \frac{c(1-b^2)}{(1+2bcos(\alpha)+b^2)^{\frac{3}{2}}} \quad \text{Eq(3)}$$

where b describes the amplitude of the scattering direction and c describes the partition between forward and backward scattering. For the case where c=0, positive b values are backward scattering, negative b values are forward scattering, and b = 0 is an isotropic scattering function.

The coverage in the forward scattering direction (**Fig. A2**), especially in phase angle, is significantly lower than in the backward scattering direction (50% or more of the phase angle bins contain observations in the backward scattering direction, whereas less than 15% of the phase angle bins contain observations in the forward scattering direction) for each of the hollows areas, therefore the partition parameter, $\boldsymbol{c}$, may not be well constrained by the data set. Hapke (2012b) demonstrated an empirical relationship between the scattering amplitude, b, and the scattering partition, c. However, Hapke (2012b) derives the mathematical relationship between b and c using a different formulization of the Henyey-Greenstein function, P_{Hapke}, is given by

$$P_{hapke}(\alpha) = \frac{1+c_H}{2}\left[\frac{1-b^2}{(1-2bcos\alpha+b^2)^{3/2}}\right] + \frac{1-c_H}{2}\left[\frac{1-b^2}{(1+2bcos\alpha+b^2)^{3/2}}\right] \quad \text{Eq (4)}$$

where the phase function amplitude, b, is equivalent to the phase function amplitude in Eq. 3, however the scattering partition parameters, c and c_H, are related by

$$c = \frac{1-c_H}{2} \quad \text{Eq. (5).}$$

Hapke (2012b) derived a relationship between b and c_H, where the value of c_H is given by

$$c_H = 3.29\exp(-17.4b^2) - 0.908 \quad \text{Eq. (6),}$$

from which we give the relationship between the scattering partition parameter c and b to be:

$$c = \frac{1-[3.29\exp(-17.4b^2)-0.908]}{2} \quad \text{Eq. (7).}$$

A summary of the model parameters is provided in Table 1.

As a test of this approach, the data was also modeled with the scattering partition parameter as a free parameter. The results in this case showed b vs c values commensurate with the hockey-stick relation, and similar relationships between morphological units and the other parameters, though the scatter in the data values was larger. The modeling results presented focus on the application with c determined with the hockey-stick relationship. Data from both the backward and forward scattering direction were used to model the photometric properties, however the quantity of data in the forward scattering direction is insufficient to constrain the value of 'c', thus the hockey-stick relationship is used.

In many images there are areas that fall into shadow. The algorithm that returns the incidence, emission, and phase angle values for the images returns unrealistic incidence and emission angles in the shadowed areas. Pixels with incidence and emission angles greater than 70º are removed from the data sets.

Table 1. Hapke Parameters

Parameter	Value or range used in modeling	Description
w	0.05 – 0.9	Single scattering albedo
B_{so}	2.01	SHOE amplitude
h_s	0.07	SHOE width
b	0.001 – 0.8	Scattering function amplitude
c	$c = \frac{1-[3.29\exp(-17.4b^2)-0.908]}{2}$	Scattering function partition
$\overline{\theta}$	0.01 – 40	Surface roughness

The mathematical complexity of the Hapke model equations introduces the plausibility of non-unique solutions. The "best fit" solution, defined as the set of parameters that produces the lowest root mean square error (RMSE) between modeled and observed data, may not be the only set of plausible photometric parameters. We adopt a probabilistic Bayesian inverse formulation, as described and used by Domingue et al. (2023, 2024), to determine the model parameter values. This approach uses Markov Chain Monte Carlo (MCMC) sampling to estimate the full parameter probability distribution space.

The MCMC employed is the python package "emcee" (Foreman-Mackey et al., 2013), which uses random "walkers" to evaluate models in the model space. A walker randomly selects a set of model parameter values, calculates the corresponding reflectance, and compares it with the measured reflectance. How well the calculated reflectance approximates the measured reflectance then determines how far the walker will move in the parameter space when selecting the next random model; a closer approximation means the walker will stay nearby in the model space and

a worse approximation means the walker will explore models further away. In the infinite limit, the frequency at which a walker samples each point in the model space is proportional to the probability density at that location (Foreman-Mackey et al., 2013), meaning that regions within the model space that poorly fit the data are sampled infrequently, which significantly reduces the number of models that need to be evaluated. Our approach uses 1000 walkers each taking 1000 samples and discarding the first 200 samples to ensure that the walker has found a region of high probability. We evaluate the best fitting model, and the median value of each model parameter distribution along with its corresponding upper and lower 1-sigma bounds. Tests run using larger number of walkers did not produce significantly different results.

A framework for interpreting the results is provided in the Appendix.

Photometric Modeling Results

The mapping of the individual Hapke model parameters for each area are shown in the Appendix (Figures A6 – A8). To examine the quality of the parameter solutions, the model parameters derived for each area were used to reconstruct the images used in the modeling. In essence, replica or synthetic images were created of each image in the data set and a ratio image between the actual image and the model-derived synthetic image provides a measure of the quality of the solution (examples shown in **Figs. 2 – 4**).

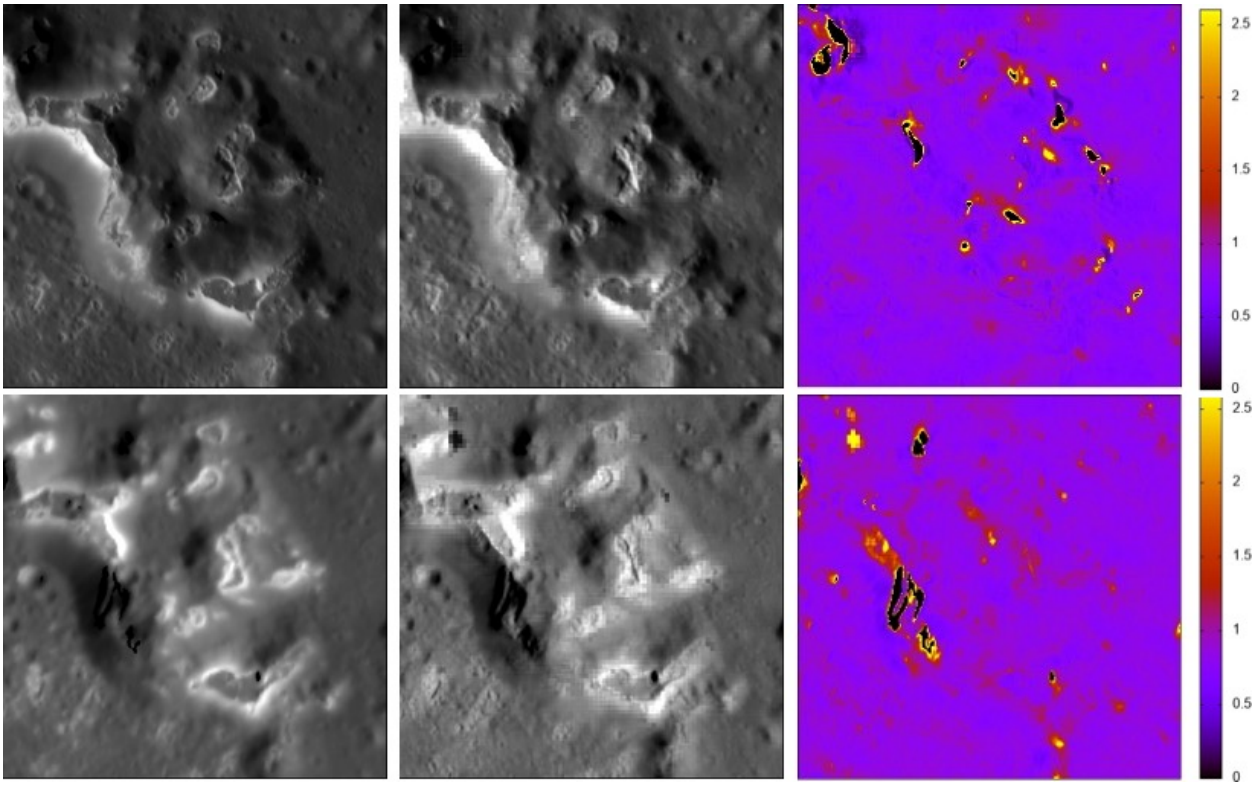

Figure 2. Example images from Area I. Top left is NAC image N1046021872M. The top center image is a synthetic image of the image on the left based on the Hapke model parameters shown in Figure 2. The top right is a ratio of the observed image (left) to the model image (center). Bottom left is WAC image W0231179208G. The bottom center image is a synthetic image of the image on the left based on the Hapke model parameters shown in Figure 2. The bottom right is a ratio of the observed image (left) to the model image (center). The observed and synthetic images in the

top row are displayed on a grey scale of 0 – 0.152 and those on the bottom row are displayed on a grey scale of 0 – 0.134. Both ratio images are displayed on a grey scale of 0 – 2.5. The black areas in the ratio image are regions in shadow in the observed image, based on the SPC shape model.

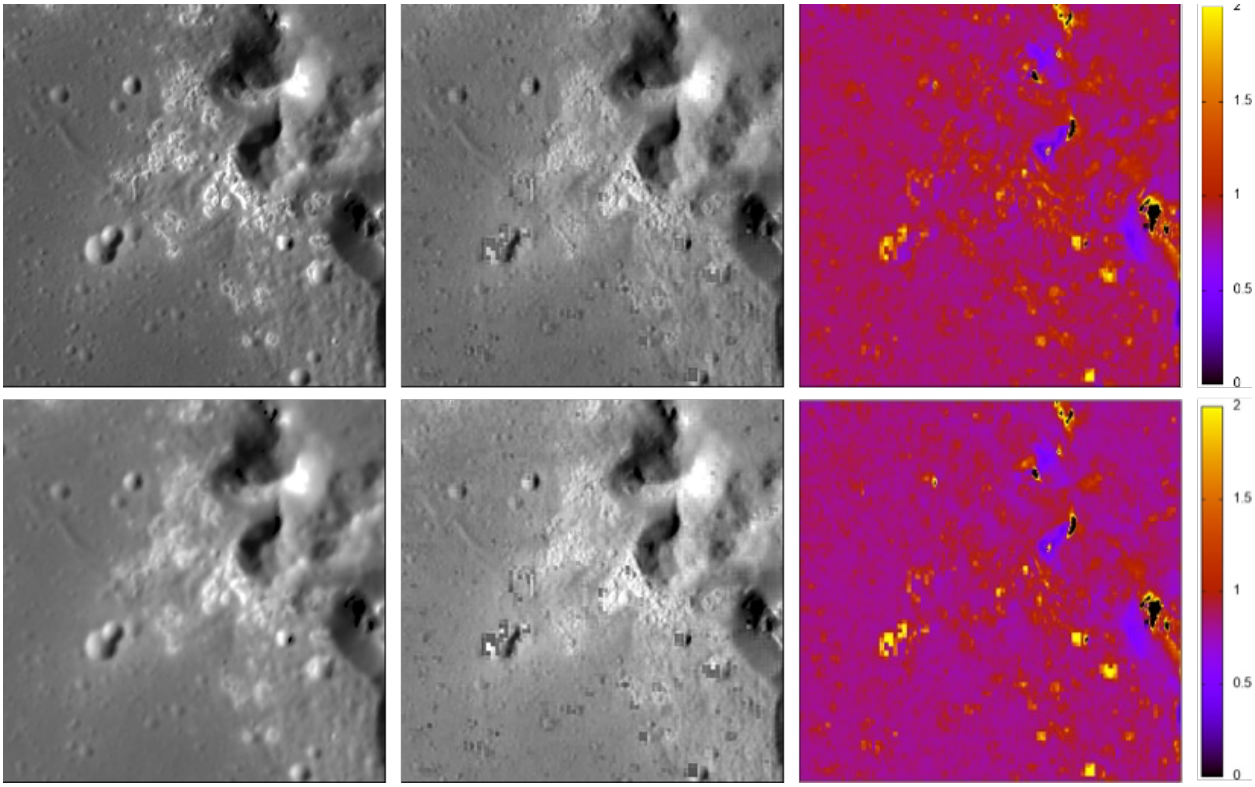

Figure 3. Example images from Area II. Top left is NAC image N1025853427M. The top center image is a synthetic image of the image on the left based on the Hapke model parameters shown in Figure 3. The top right is a ratio of the observed image (left) to the model image (center). Bottom left is WAC image W0231179208G. The bottom center image is a synthetic image of the image on the left based on the Hapke model parameters shown in Figure 3. The bottom right is a ratio of the observed image (left) to the model image (center). The observed and synthetic images in the top row are displayed on a grey scale of 0 – 0.08 and those on the bottom row are displayed on a grey scale of 0 – 0.09. Both ratio images are displayed on a grey scale of 0 – 2.5. The black areas in the ratio image are regions in shadow in the observed image, based on the SPC shape model.

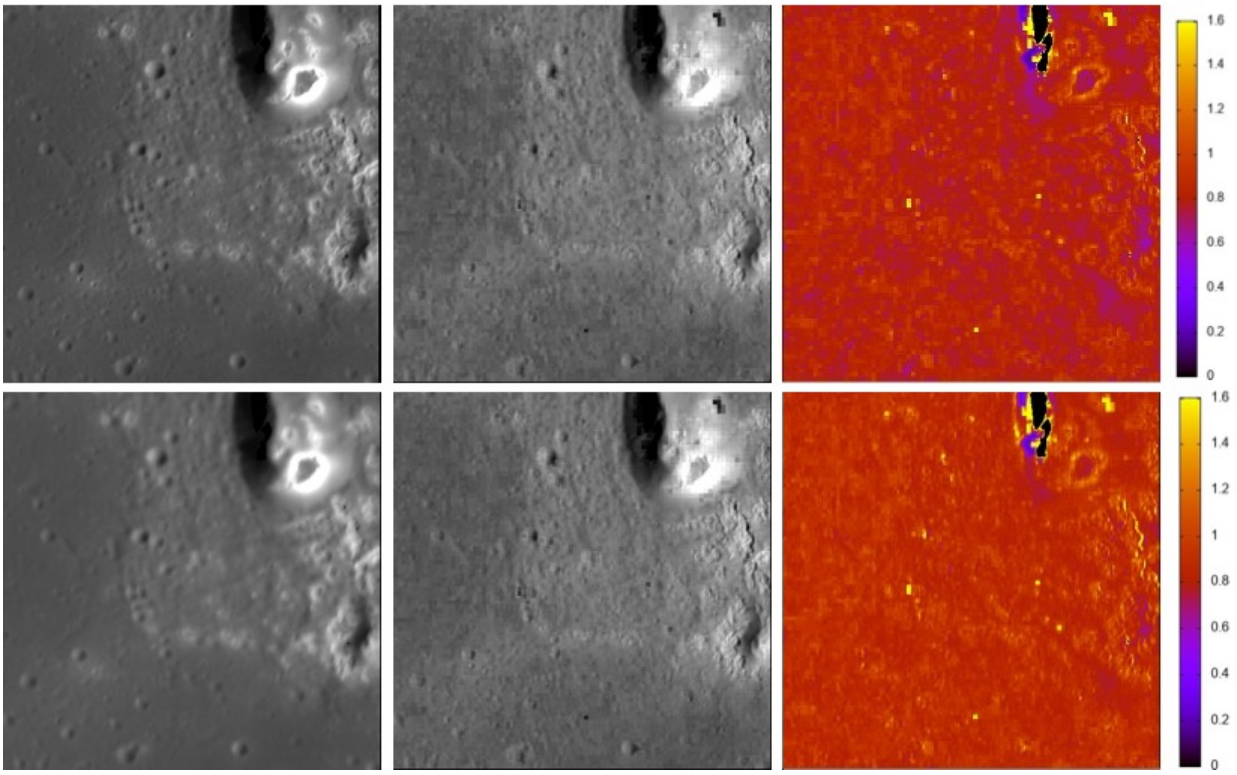

Figure 4. Example images from Area III. Top left is NAC image N1025680666M. The top center image is a synthetic image of the image on the left based on the Hapke model parameters shown in Figure 4. The top right is a ratio of the observed image (left) to the model image (center). Bottom left is WAC image W0231179208G. The bottom center image is a synthetic image of the image on the left based on the Hapke model parameters shown in Figure 4. The bottom right is a ratio of the observed image (left) to the model image (center). The observed and synthetic images in the top row are displayed on a grey scale of 0 – 0.13 and those on the bottom row are displayed on a grey scale of 0 – 0.12. Both ratio images are displayed on a grey scale of 0 – 2.5. The black areas in the ratio image are regions in shadow in the observed image, based on the SPC shape model. The pixilation in the synthetic images (center) is due to the 10 x 10 pixel binning of the original data set.

Ratios of the observed images with the synthetic images created from the Hapke model solutions provide a visual measure of the quality of fit obtained by the modeling effort. The examples shown in **Figures 2 – 4** are some of the better fits. Ratio values of unity represent an exact match between observation and model prediction of the absolute reflectance. The ratio values can be binned into groups based on how much they depart from unity. Bins representing 5, 10, 15, 20, 25, 30, and >35 departures were examined. Ratio values greater than unity represent areas where the model underestimates the absolute reflectance, whereas ratio values less than unity represent areas where the model overestimates the absolute reflectance. **Figure 5** displays a histogram for each of the areas, showing the percent departure, from a perfect solution over all images used in the modeling effort. For each area, the model predicts the absolute reflectance to within 20 – 25% for the majority of the imaged area, with the model predicting a brighter surface than measured. This overprediction in the reflectance is due to some of the assumptions made in the model parameters, such as using the global shadow hiding opposition parameters and the

hockey-stick relationship between the particle scattering function parameters, due to lack of data in the forward scattering direction to constrain these parameters.

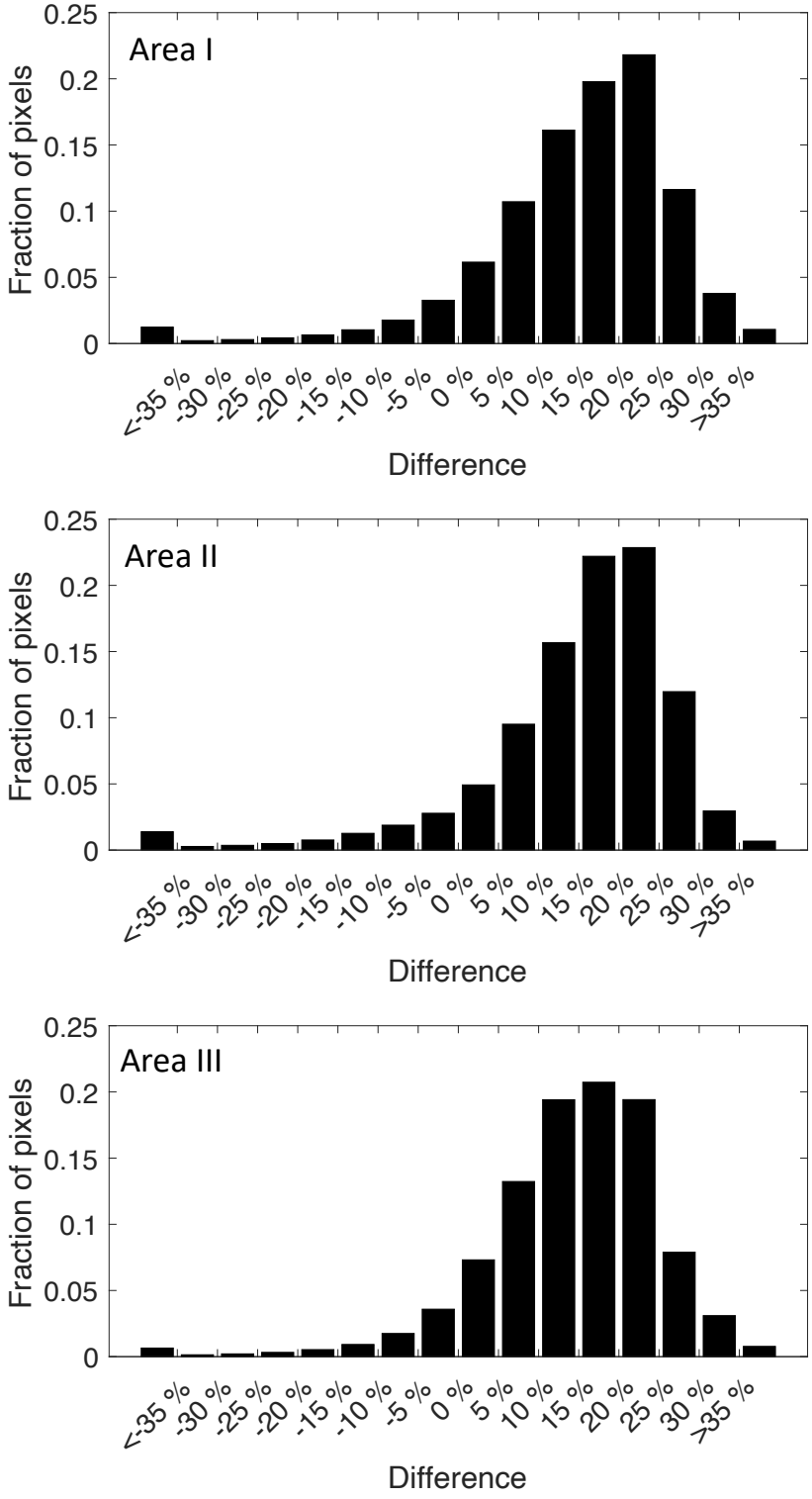

*Figure 5. Histograms of Area I (top), Area II (center), and Area III (bottom) showing the percent differences from summed over all images used to model the reflectance behavior in each area in terms of the fraction of pixels from the total in each percent difference category. Histograms for the individual images are shown in the supplementary materials (**Figs. A10 – A12**).*

Examination of the distributions within the Bayesian solutions show convergence on a single set of solutions, with no indications of a plausible set of solutions at another local minima (**Figure A9**). Further examination of the image data set also shows variation in the spatial resolution (see **Tables A1 – A3**) that can contribute to large uncertainties within the reflectance values for each location on the surface. Given the quality of the data set, including the angular coverage, the convergence of the solutions within the parameter space, we then chose to examine the relative reflectance values within the three areas. The relative

433 reflectance is defined as the reflectance ratioed to a standard area within each study region, in
434 contrast to the absolute reflectance which is the reflectance relative to the incident light (in this
435 case sunlight). This was done to provide some understanding of how well the model captures the
436 relative differences between units within each study area. In the interpretation of the results, it is
437 important to be able to identify places of similar and dissimilar structural properties. The
438 dissimilarities are captured by the relative differences between parameter values.
439 A representative, standard region was selected in each area (**Fig. 6**) and the median reflectance
440 value within that standard region was calculated for each image. The image displays the ratio of
441 the reflectance to the median reflectance of the standard region, providing a map of the relative
442 reflectance to the standard region for each image. This normalization was performed on both the
443 observed images and the synthetic, model-based images. A ratio between the observed normalized
444 image and its corresponding normalized synthetic image was calculated. The purpose of this
445 normalized reflectance comparison is to ascertain how well the model captures the relative
446 reflectance variations, and thus the relative variations in physical structure. The ratio values were
447 binned into groups based on how much they departed from unity, with bins representing 5, 10, 15,
448 20, 25, 30, >35 percent departures. Ratio values greater than unity represent areas where the model
449 underestimates the relative reflectance, whereas ratio values less than unity represent areas where
450 the model overestimates the relative reflectance. **Figure 6** displays a histogram for each of the
451 areas, showing the percent departure between the measured relative reflectance and the model
452 predicted relative reflectance. For each area, the model predicts the relative reflection to within 10
453 – 15% for the majority of the imaged area, with the distribution centered on unity. Predictions
454 below 10% are considered good (within the accuracies of most telescopic observations (Domingue
455 et al. 2002)). We interpret these values to indicate that the modeling results can confidently capture
456 relative differences/variations between the units within each area that are above the 15% level.
457

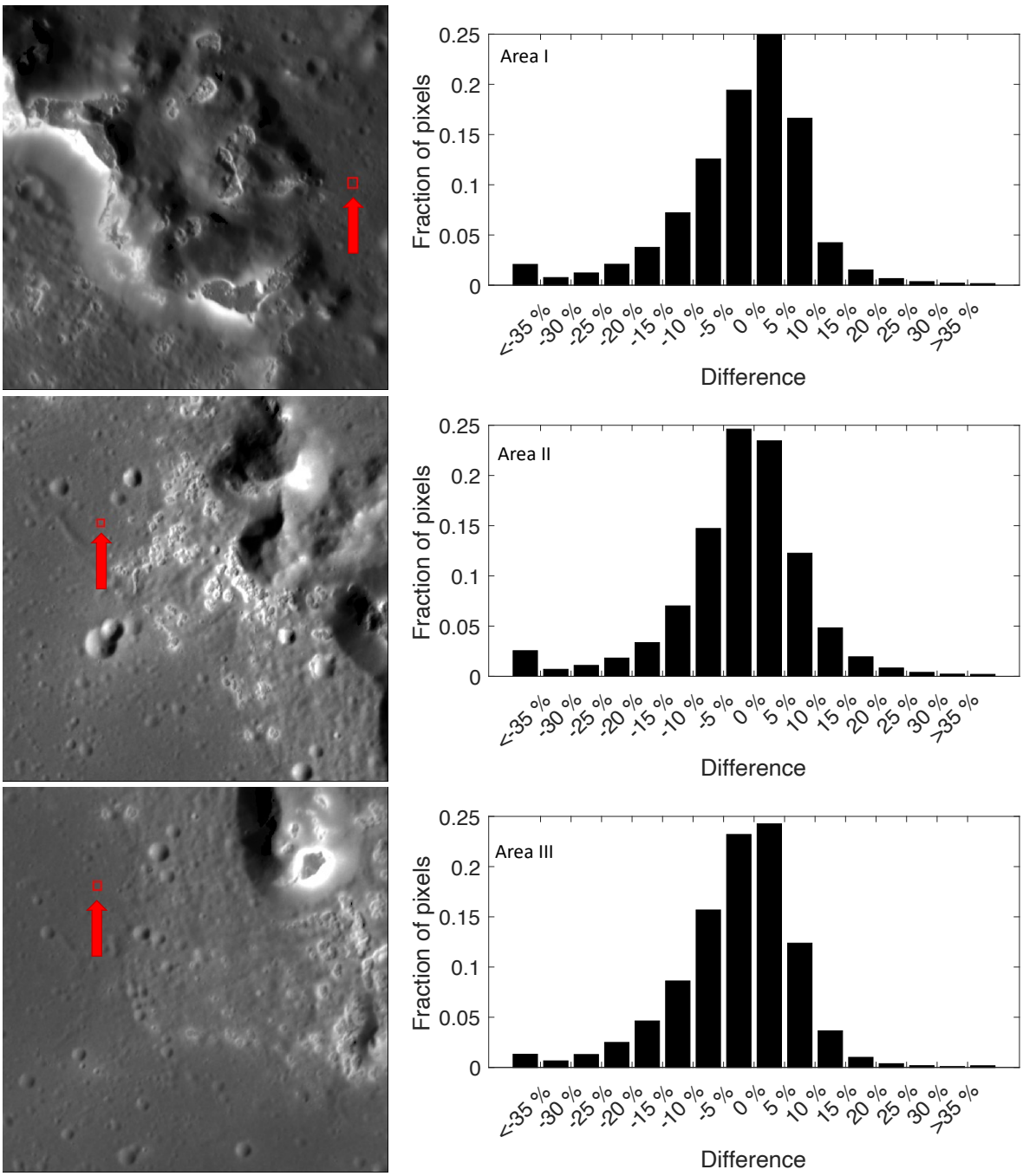

*Figure 6. (left) Images of each study area (top to bottom: Area I, Area II, and Area III) with a red square (highlighted by a red arrow) denoting the region used for calculating the standard reflectance. (right). Histograms of Area I (top), Area II (center), and Area III (bottom) showing the percent differences between the normalized reflectance between the actual image and the normalized reflectance from the model images, summed over from all images used to model the reflectance behavior in each area. The histograms show the fraction of pixels from the total in each percent difference category. Histograms for the individual images are shown in the supplementary materials (**Figs. A13 – A15**).*

Analysis of Photometric Properties

Examination of each of the parameter maps for the three areas displays some distinct trends with morphology. The single scattering albedo (**Fig. 7**) shows that hollows units, regardless of their presence on the glacial flows or the peak summits, are brighter (higher values of ***w*)** in all three areas. The yellow arrows in **Figure 7** highlight examples of the brighter hollows as compared to the surrounding terrains. The peak walls also show trends with single scattering albedo. The walls can be divided into two sections, one with a high reflectance and adjacent to hollows (red arrows in **Fig. 7**) and another with an intermediate albedo (blue arrows in **Fig. 7**) and forming a border with the glacial flow features. The high reflectance wall sections also display a high single scattering albedo, whereas the intermediate albedo wall units display single scattering albedos similar to the lower albedos on the glacial flows and basin floor. Areas II and III include boundaries between the glacial flow units and the basin floor (blue/black lines in **Fig. 7**). The glacial floors appear to have, on average, a slightly higher single scattering albedo value than the basin floor in both areas. Outlined in red in **Figure 7** are two regions within Area I on the peak ring walls that display high single scattering albedo values that are not correlated with high-reflectance areas in the images, suggesting potential grain-size variations. These regions, hereafter referred to as 'anomalous regions', are adjacent to flat-topped peaks that form mesas within the peak-ring system. They are not the only areas where the single scattering albedo is greater than expected based on the reflectance values, but are two of the largest regions.

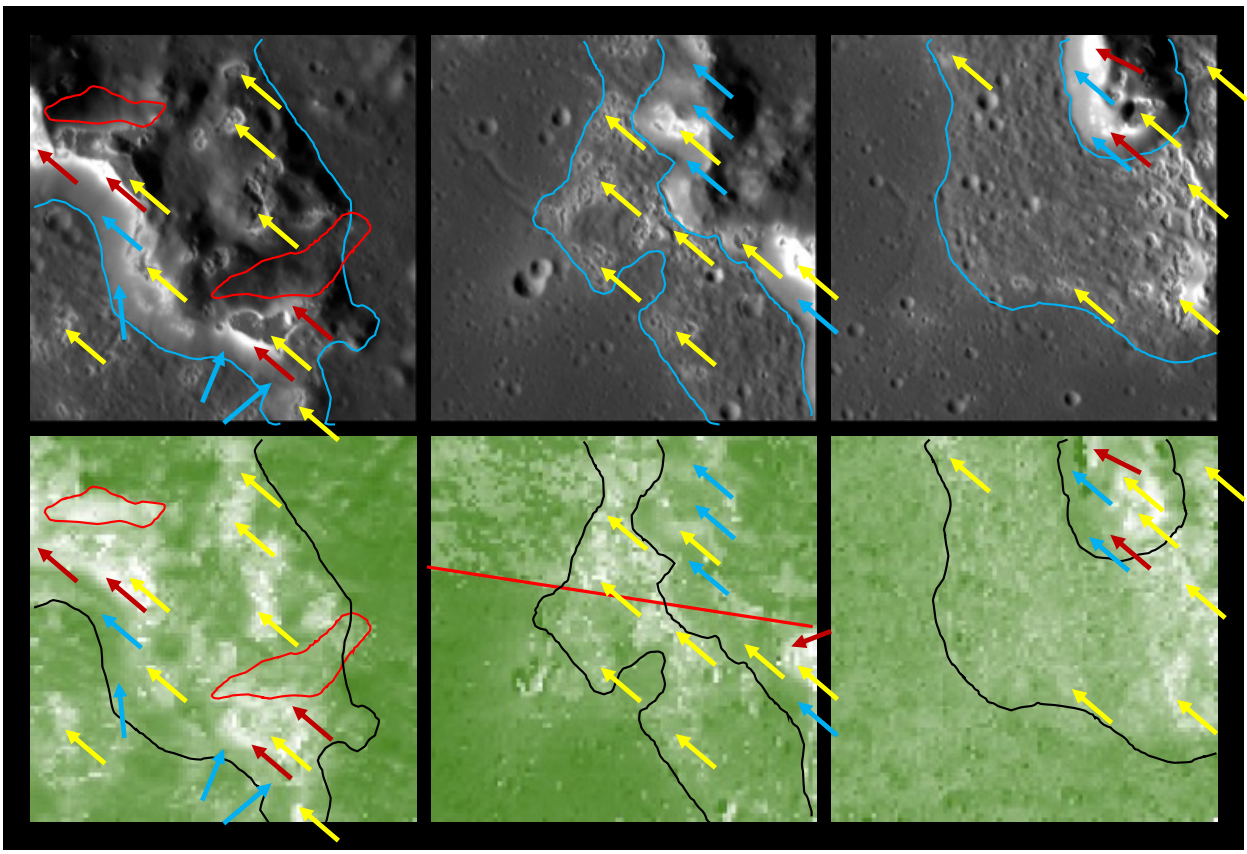

Figure 7. Areas I, II, and III (left to right columns) displaying the reflectance image (top row) single scattering albedo map from the 3-parameter solution (bottom row). The blue lines in the reflectance image (top row) display the boundary between the peak ring and either the glacial flow unit or the basin floor and the glacial flow and the basin floor. These lines are repeated in

black in the parameter maps. The yellow arrows point to examples of hollows within either the glacial flow or the summits of the peak ring. The red arrows point to examples of high-reflectance materials along the peak walls and the blue arrows point to examples of moderate-reflectance materials along the peak walls. The thick red line in the area II maps show the demarcation between data quality regions that are apparent in all the parameter maps for the 3-parameter solutions, with more extensive angular coverage available below the thick red line. The thinner red lines in the area I image and maps display regions on the peak walls with high single scattering albedo properties, but do not display high-reflectance values in the image of the area.

Examination of the surface roughness values (**Fig. 8**) do not display consistent, discernible patterns that distinguish hollows units from other units within the areas. Some appear rougher (higher values, brighter areas in the maps), while others appear smoother (lower values, darker areas in the maps). Hollow floors often appear rougher than the halos surrounding them. Many of the higher-reflectance wall sections display smoother roughness values, though there are counter examples also visible. Similarly, the moderate-reflectance wall sections display rougher surface roughness than the higher-reflectance wall sections, though there are a few counter examples in each area. The glacial flow units in Areas I and II display a marginally smoother surface roughness. The anomalous regions on the walls adjacent to the mesas in Area I (**Fig. 7**) also display some of the roughest surfaces in Area I.

The final free parameter in this modeling solution is the single particle scattering function's amplitude, b, parameter. The partition parameter, *c*, is derived from the *b* values as discussed above, and thus will have similar correlations with morphology. Examination of the *b* parameter values (**Fig. 9**) does not show any consistent correlation between *b* values and the location of the hollows units. Nor is there any consistent trend with either of the wall units and the values of the amplitude parameter. The glacial flow feature in Area III displays apparently higher *b* values than the basin floor, but lower than the adjacent peak walls. There is no clearly observable distinction between the glacial flow and the basin floor in Area III. The anomalously high regions in single scattering albedo in Area I, which also display as rough, show lower values of *b*, which correlate to more opaque and irregularly shaped (or rougher grain surface) grains (**Fig. 10**).

The correlation between opacity, shape, and grain surface properties is based on laboratory measurements and modeling of a broad range of planetary surfaces and laboratory samples. The correlation is described by the 'hockey stick relationship' derived by Hapke (2012b). This provides insight into average grain properties and an examination can be made of variations as a function of geomorphology. Each study region was mapped into different units (**Fig. 10**) and the median value of the scattering function amplitude (*b*) and partition (*c*) parameters were calculated for each unit and plotted on the hockey stick diagram (**Fig. 10**). The units were binned into different morphological categories, where the basin floor included unit 1 from all three areas, the glacial-like flow included unit 2 from Areas I and II and unit 3 from Area III, the peak ring walls included unit 3 from Area I, and unit 4 from Areas II and III, the top of the peak ring included unit 4 from Area I and unit 5 from Areas II and III, interior terrains within the peak ring (inner peak) included unit 5 from Area I and unit 6 from Area III. Area II unit 3 is an example of a hollows field and Area III unit 2 is a region surrounding a crater on the basin floor near the flow feature. Each morphological category shows that the grains within each terrain is best described by particles that are opaque and irregular in shape with rougher surfaces. There is some variation between the terrains, but overall, the grains are similar.

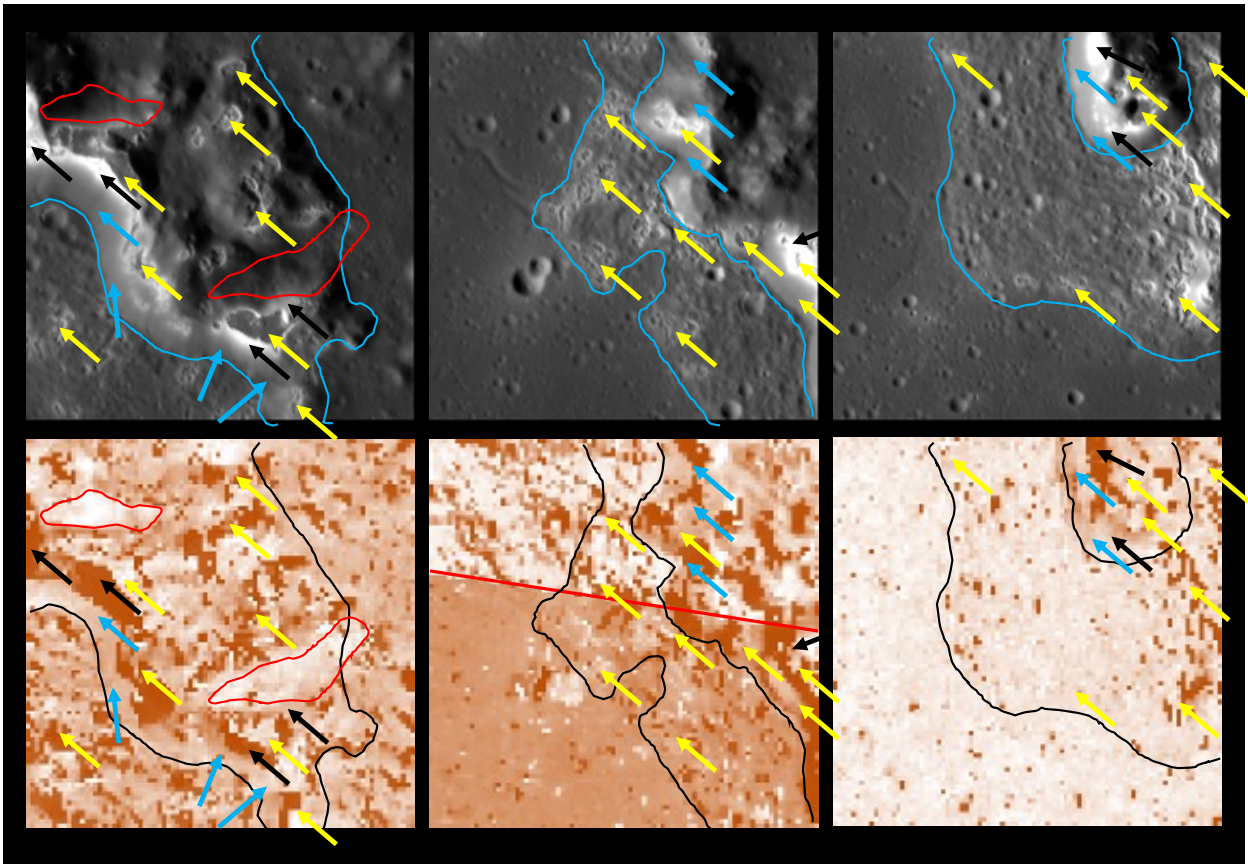

Figure 8. Areas I, II, and III (left to right columns) displaying the reflectance image (top row) and the surface roughness ($\overline{\theta}$) map from the 3-parameter solution (bottom row). The blue lines in the reflectance image (top row) display the boundary between the peak ring and either the glacial flow unit or the basin floor and the glacial flow and the basin floor. These lines are repeated in black in the parameter maps. The yellow arrows point to examples of hollows within either the glacial flow, peak walls, or the summits of the peak ring. The black arrows point to examples of high-reflectance materials along the peak walls and the blue arrows point to examples of moderate-reflectance materials along the peak walls The thick red line in the area II maps show the demarcation between data quality regions that are apparent in all the parameter maps for the 3-parameter solutions, with more extensive angular coverage available below the thick red line. The thinner red lines in the area I image and maps display regions on the peak walls with high single scattering albedo properties, but do not display high-reflectance values in the image of the area (top). These regions appear as some of the roughest regions in area I.

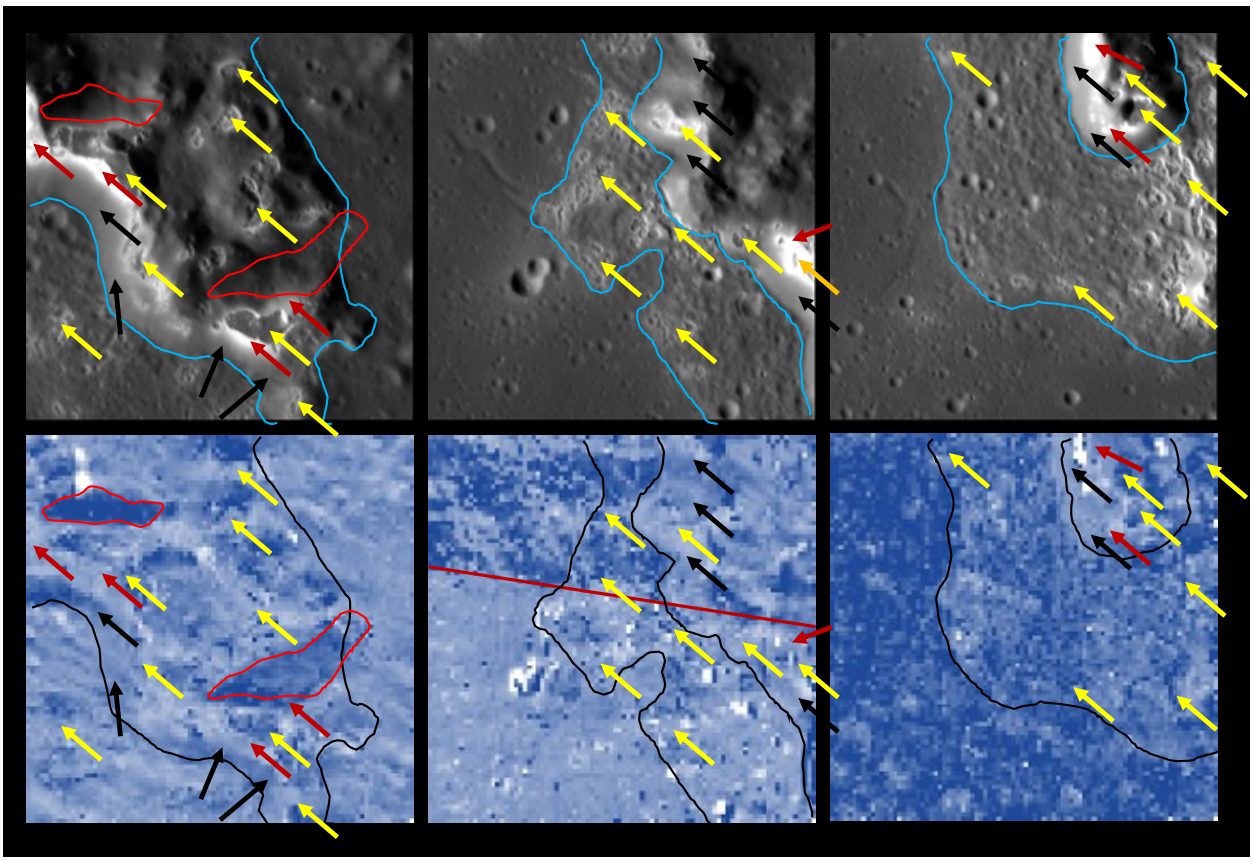

Figure 9. Areas I, II, and III (left to right columns) displaying the reflectance image (top row) single particle scattering function amplitude, b, map from the 3-parameter solution (bottom row). The blue lines in the reflectance image (top row) display the boundary between the peak ring and either the glacial flow unit or the basin floor and the glacial flow and the basin floor. These lines are repeated in black in the parameter maps. The yellow arrows point to examples of hollows within either the glacial flow or the summits of the peak ring. The red arrows point to examples of high-reflectance materials along the peak walls and the black arrows point to examples of moderate-reflectance materials along the peak walls. The thick red line in the area II maps show the demarcation between data quality regions that are apparent in all the parameter maps for the 3-parameter solutions, with more extensive angular coverage available below the thick red line. The thinner red lines in the area I image and maps display regions on the peak walls with high single scattering albedo properties, but do not display high-reflectance values in the image of the area (top). These regions also show anomalously low b values for this area.

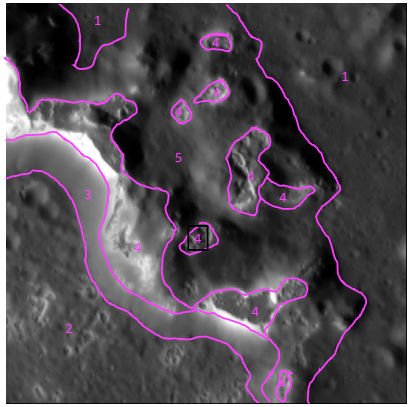

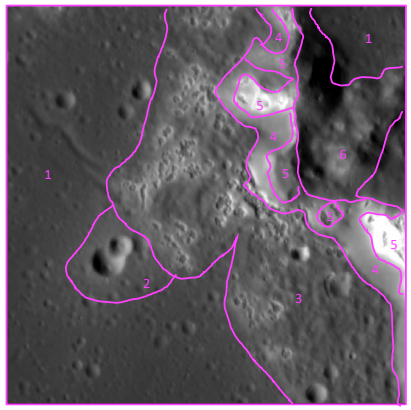

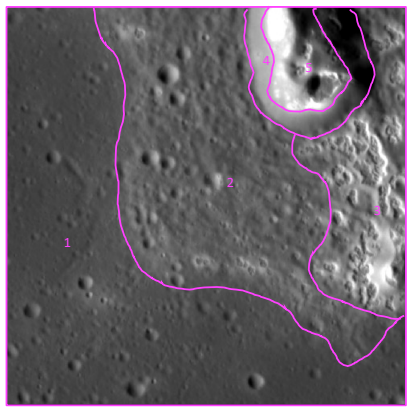

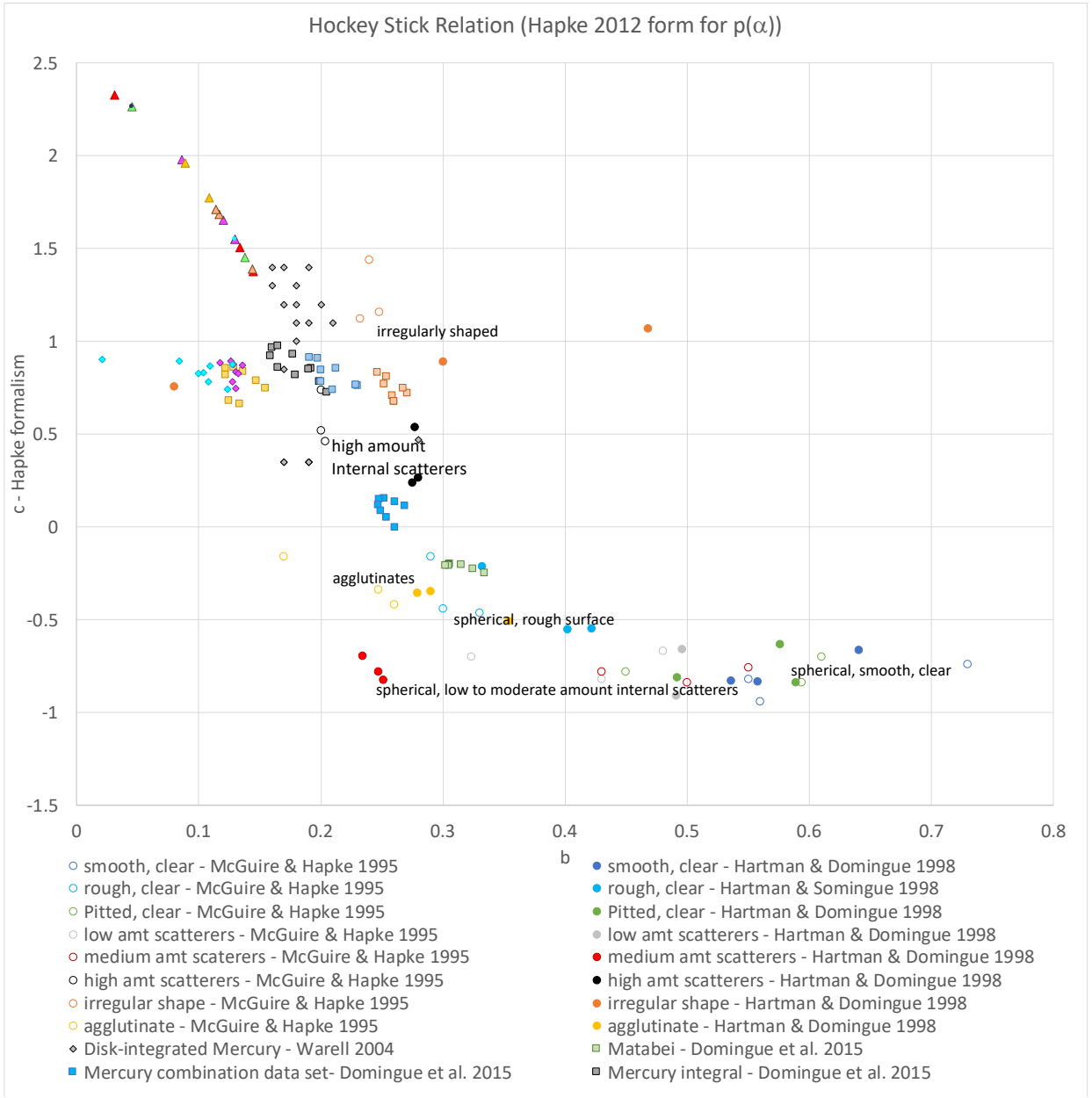
Hockey Stick Relation (Hapke 2012 form for p(α))
c - Hapke formalism
b
irregularly shaped
high amount
Internal scatterers
agglutinates
spherical, rough surface
spherical, smooth, clear
spherical, low to moderate amount internal scatterers
smooth, clear - McGuire & Hapke 1995
rough, clear - McGuire & Hapke 1995
Pitted, clear - McGuire & Hapke 1995
low amt scatterers - McGuire & Hapke 1995
medium amt scaterers - McGuire & Hapke 1995
high amt scatterers - McGuire & Hapke 1995
irregular shape - McGuire & Hapke 1995
agglutinate - McGuire & Hapke 1995
Disk-integrated Mercury - Warell 2004
Mercury combination data set- Domingue et al. 2015
smooth, clear - Hartman & Domingue 1998
rough, clear - Hartman & Somingue 1998
Pitted, clear - Hartman & Domingue 1998
low amt scatterers - Hartman & Domingue 1998
medium amt scatterers - Hartman & Domingue 1998
high amt scatterers - Hartman & Domingue 1998
irregular shape - Hartman & Domingue 1998
agglutinate - Hartman & Domingue 1998
Matabei - Domingue et al. 2015
Mercury integral - Domingue et al. 2015

569

570 *Figure 10. Hapke's 'hockey-stick' relationship (Hapke 2012b) between the scattering function amplitude (b) and the scattering function*
571 *partition (c) parameters used in the modeling of the Raditaldi regions compared to other Mercury studies and the laboratory*
572 *measurements of McGuire and Hapke (1995) and the remodeling of those measurements by Hartman and Domingue (1998). The results*
573 *for different morphological categories in the study regions are shown in magenta. The area maps along the side of the graph denote the*
574 *different morphological units examined. Unit 1 in all areas represents basin floor. Unit 2 represents the flow-like features in Area I and*
575 *III, in Area II it represents a double crater with possible ejecta. Unit 3 represents peak ring walls in Area I, flow-like features in Area II,*
576 *and hollows fields in Area III. Unit 4 represents hollows in Area I and peak ring walls in Areas II and III. Unit 5 represents inter-peak*
577 *terrains in Area I, hollows in Area II and III. Note that the 'c values' have been converted to match the formalism in Hapke 2012b due*
578 *to the different formulation of the single particle scattering function, as discussed in section describing the Modeling Approach and*
579 *Methodology. This diagram has been converted to match that in Hapke 2012b.*

Color-Coded Analyses

To determine if there are plausible correlations with morphology and combinations of parameters, the Hapke model parameter images were used to create color maps of the three study areas and then compared with the morphologic units. The surface roughness, single scattering albedo, and scattering amplitude are displayed in the red, green, and blue channels, respectively (**Figure 11**). It is important to note that the properties being examined are the relative differences in parameters from terrain to terrain, and not the absolute values. This provides a mechanism for examining relative changes in grain properties (size, shape, composition) and inter-grain properties (compaction/porosity and surface tilt/roughness).

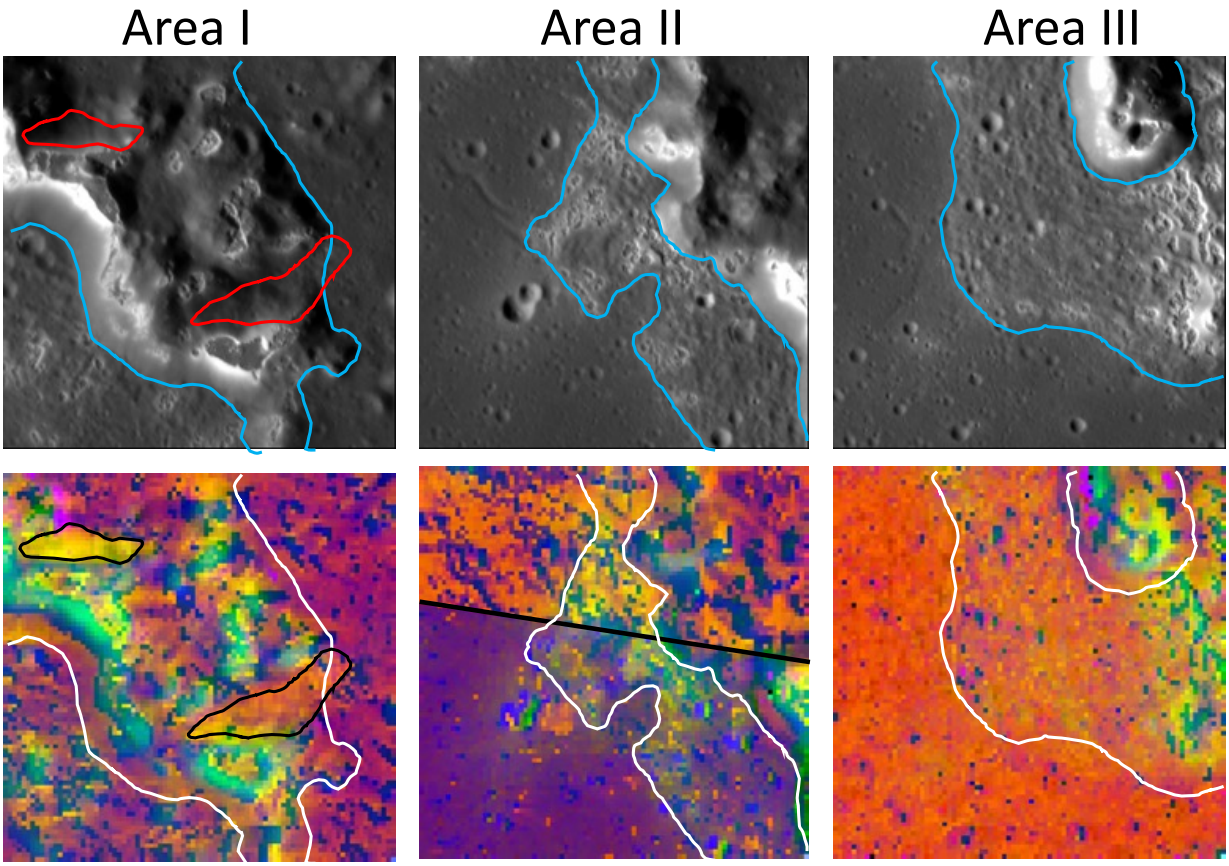

Figure 11. Color representation of the photometric model parameters compared to the regional morphology. The first column presents Area I, the center column presents Area II, and the right column presents Area III. The top row is an image of the corresponding area (Fig. 1) with morphologic boundaries shown in blue, and the area I high single scattering albedo regions outlined in red. The second row displays the surface roughness, the single scattering albedo, and the phase function amplitude in red, green, and blue, respectively. The morphologic boundaries are displayed in white, with the area I high single scattering albedo regions outlined in black. The black line across area II shows the demarcation between data quality regions.

The regions of basin floor in each area appear mottled in the color maps with the darker colors, such as purple, dark blue, and darker shades of orange (**Figure 11**). This corresponds to areas with comparatively low values of single scattering albedo (**Figure 12-left column**), moderate to high values of surface roughness (**Figure 12-center column**), and a range in scattering function

amplitude values (**Figure 12-right column**) corresponding to irregularly shaped and opaque grains. It should be noted that regardless of morphology, the regolith grains in the study areas are ubiquitously irregularly shaped and opaque. There are subtle differences between morphological units, but all values map in a region of the hockey-stick diagram correlating to irregularly shaped, opaque particles (**Figure 10**).

The flow-like features in each area also appear mottled in color, but with lighter shades of the colors seen on the basin floor, except for locations where hollows are present (**Figure 11**). For regions on the flow-like features that do not contain hollows or their associated halos, the photometric parameters are similar to that for the basin floor with the exception of higher values of the single scattering albedo on the flows. Areas I and II show roughness values on the flow regions without hollows and halos that overlap with the smoother portions of the basin floor. Area II shows differences associated with data quality, where the top portion of the area shows the properties of the flow are commensurate with the properties of the basin floor, but the bottom portion of the area shows comparable albedos. The flows include regions of higher roughness than the basin floor. The scattering amplitude for these portions of the flows show grains of comparable shape and opacity as the basin floor, with the exception of Area III where the grains are subtly more equant and less opaque than the basin floor. The hollows and halos within the flow units are distinguished by the presence of yellows and greens (**Figure 11**). This corresponds to higher values of single scattering albedo (**Figure 12-left column**). Surface roughness values generally overlap with the lower range of basin floor values (**Figure 12-center column**) in Areas I, III, and the bottom portion of Area II whereas the roughness values in the top portion of Area II are comparatively rougher. The scattering function amplitude values for the flow regions that contain hollows either overlap with the basin floor values or are higher (**Figure 12-right column**), corresponding to grains that are subtly more equant and transparent.

The colors within the peak ring structures are more complex. The hollows and halos display similar color schemes to those within the flow-like features, where the walls and inter-peak terrains are mottled with shades of orange, magenta, and dark blue, similar to the flows where there are no hollows or halos (**Figure 11**). In charts of the parameter values, the halos within the peak ring structure typically have the highest single scattering albedos whereas the hollows display a similar albedo to those within the flow-like features (**Figure 12-left column**). The walls and inter-peak terrains display albedos similar to those of the basin floor and flows (**Figure 12-left column**). The halos display the lowest (smoothest) values in surface roughness, whereas the hollows within the peak ring structure displays a broad range, from low to high (**Figure 12-center column**). The surface roughness of the walls and inter-peak terrains overlap with those of the basin floor and flows (**Figure 12-center column**). The scattering function amplitude is not well constrained in Area II for the halos, showing a broad range of values. For the other study areas, the scattering function amplitude of the hollows and halos overlaps with those found in the flows (**Figure 12-right column**). The scattering function amplitude for the walls and inter-peak terrains is similar to that of the basin floor (**Figure 12-right column**).

In Area I there are a unique set of features, the mesas which are topped with hollows structures and the representative anomalous regions adjacent to these mesas. The mesas are mottled shades of yellow and orange, indicative of the high albedo values, rougher surfaces indicative of walls and inter-peak terrains, and a broad range of scattering function amplitudes, including some of the lowest observed in the area (**Figure 12**). The anomalous regions are distinctive in color, predominantly yellow with shades of brighter orange seen in the southernmost region (**Figure 11**). The northernmost anomalous region (bright yellow in color) has single scattering albedos

comparable with the hollows and overlaps with the halos in the peak ring structure, whereas the southernmost region displays a broader range, though commensurate with hollow albedos (**Figure 12-left column**). Both anomalous regions display some of the highest surface roughness values and lowest scattering function amplitudes (**Figure 12-center & right columns**).

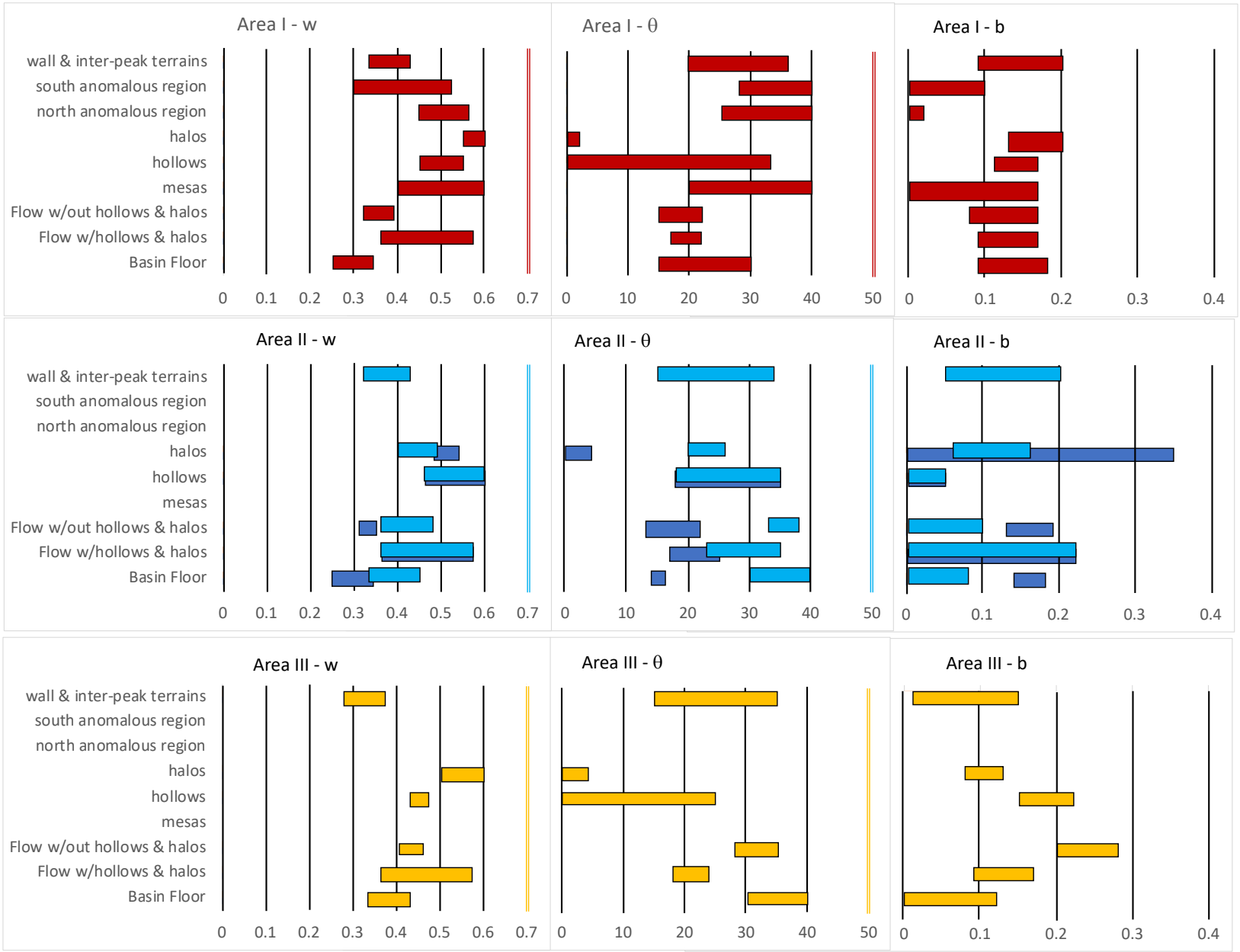
Area I - w
Area I - θ
Area I - b
Area II - w
Area II - θ
Area II - b
Area III - w
Area III - θ
Area III - b
wall & inter-peak terrains
south anomalous region
north anomalous region
halos
hollows
mesas
Flow w/out hollows & halos
Flow w/hollows & halos
Basin Floor
0 0.1 0.2 0.3 0.4 0.5 0.6 0.7
0 10 20 30 40 50
0 0.1 0.2 0.3 0.4

654

655 *Figure 12. Range of Hapke model parameter values for the different morphological units in the study areas. The top row presents the*
656 *results for Area I, the center row for Area II, and the bottom row for Area III. The left column displays single scattering albedo values,*
657 *the center column displays surface roughness values and the right column displays single particle scattering function amplitude values.*
658 *The Area II data is divided into ranges from the top, lower data quality, portion of the image (light blue) and bottom, higher data quality,*
659 *portion of the image (dark blue) offset to note the overlap.*
660

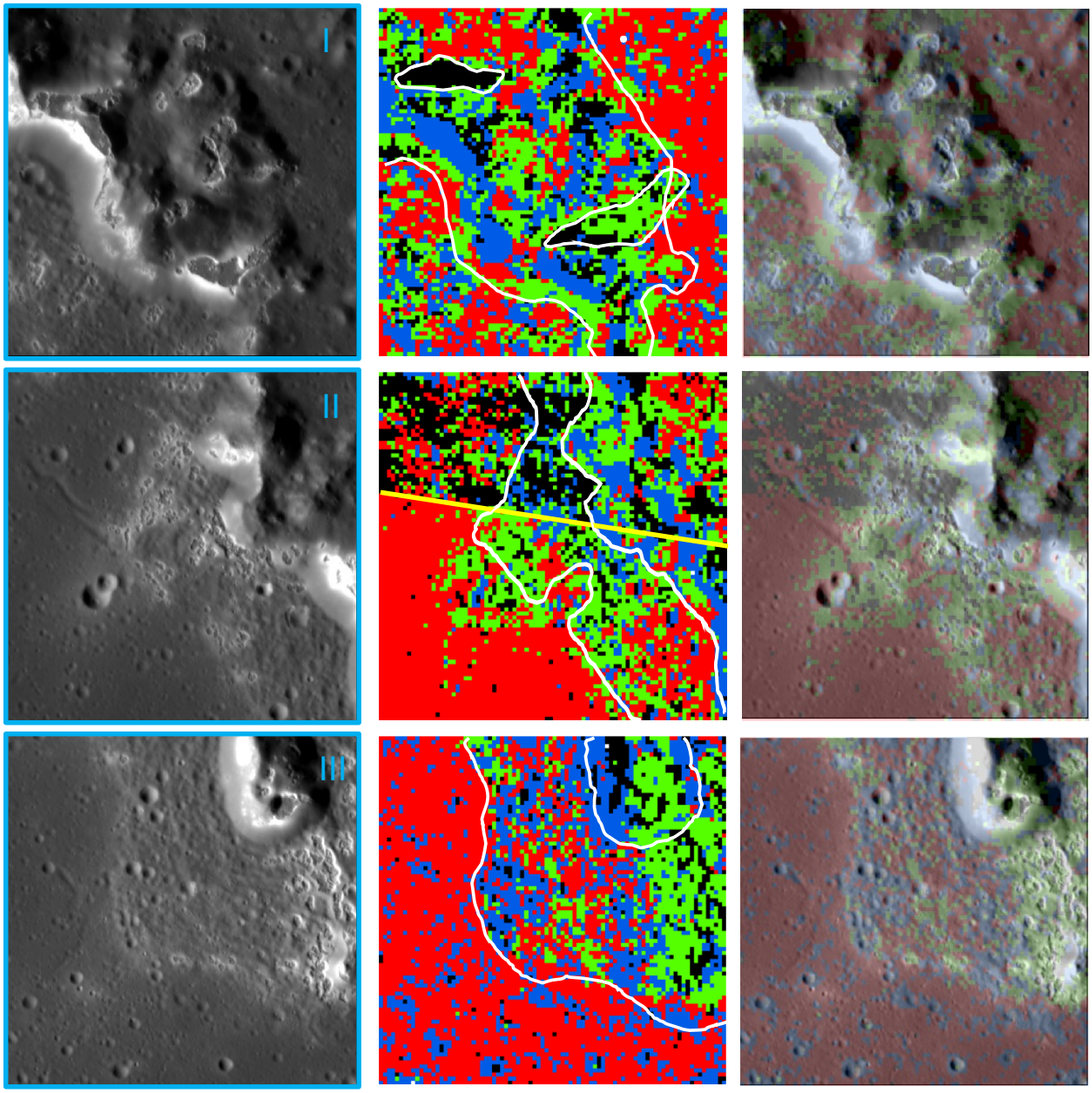

Figure 13. The K-means cluster unit maps for areas I (top), II (center), and III (bottom) using the 4-cluster solutions. The first column are grayscale reflectance images of each area, the central column are the K-means cluster unit maps with morphologic boundaries shown in white, and the right column is a transparent overlay of the K-means cluster unit maps on top of the reflectance images. For the central and right columns: Red = Cluster A, Black = Cluster B, Blue = Cluster C, Green = Cluster D. Refer to Table 2 for details on the parameter value ranges for each cluster unit.

Machine Learning-Based Analyses.

Following the methodology of Chuang et al. (2022, 202**5**) a two-step image classification approach was applied to the photometric parameters to interpret the photometric results based on the morphologic features. The first step was to apply an unsupervised K-means clustering

algorithm followed by a supervised clustering Maximum Likelihood Classification (MLC) algorithm. The K-means algorithm, available through open-source Python SciKit-Learn, is a straightforward cluster analysis tool requiring a defined number of clusters (*k*) to be assigned by the user (Pedregosa et al. 2011). Once *k* is user-defined, the algorithm then iteratively calculates all the non-overlapping clusters in N-dimensional space. The optimal number of *k* clusters can also be calculated using a common "elbow" method, an inflection point in the plot of the sum of the squared distances (SoSD) between each data point relative to its centroid and *k*. This point can be determined automatically using the Kneedle Method (Satopaa et al. 2011). Our K-means results range between three and four clusters with the latter correlating better with the morphology. The map results are shown in **Figure 13** and the mean and standard deviation for parameter values in each of the four classified units are summarized in **Table 2**. The standard deviation in the values for each cluster unit are overlapping predominately in *w* and *b* values, suggesting that the units are a function of the combination in these parameter values.

Table 2. Mean and standard deviation for parameter values of four classification units in Areas I-III based on the K-means algorithm

Unit	Parameter	Area I	Area II	Area III
A (Red)	θ	22.58 +/- 4.21	15.84 +/- 3.60	33.08 +/- 1.83
	w	0.31 +/- 0.03	0.30 +/- 0.02	0.38 +/- 0.02
	b	0.14 +/- 0.03	0.16 +/- 0.04	0.03 +/- 0.02
B (Black)	θ	33.62 +/- 5.32	34.22 +/- 4.55	$3.74^{-3.74}_{+4.55}$
	w	0.50 +/- 0.05	0.44 +/- 0.06	0.41 +/- 0.07
	b	0.03 +/- 0.03	0.04 +/- 0.03	0.13 +/- 0.05
C (Blue)	θ	$3.86^{-3.86}_{+4.30}$	$1.99^{-1.99}_{+2.34}$	28.42 +/- 3.82
	w	0.38 +/- 0.08	0.37 +/- 0.05	0.36 +/- 0.04
	b	0.16 +/- 0.03	0.15 +/- 0.05	0.11 +/- 0.05
D (Green)	θ	27.94 +/- 4.60	22.42 +/- 5.17	30.76 +/- 3.50
	w	0.40 +/- 0.05	0.37 +/- 0.04	0.47 +/- 0.04
	b	0.10 +/- 0.03	0.12 +/- 0.03	0.04 +/- 0.04

Hapke parameter values with their standard deviations.

The photometric properties of the **K-means** units grade into each other (**Figure 14**). Unit A trends darker and moderately rough. Unit A correlates mostly with the basin floor. In contrast, Unit B trends to brighter and rougher surfaces. Unit B correlates with areas adjacent to hollows or with anonymously high albedo compared to darker reflectance, typically along peak walls. Units C and D correlate with high reflectance areas indicative of hollows, halos, and bright slopes along peak walls. Unit C trends to more moderate albedo values and a wide range of roughness. Unit D is similar to Unit C, but with consistently the roughest surfaces. The particle scattering properties for all the units are indicative of irregularly shaped grains, and match what is measured from the median values for the different morphological units (Fig. 10). The overlap in grain scattering characteristics indicates similar levels of processing, though not necessarily by the same process. In terms of the cluster associations with morphology, the basin floor is dominated by unit A, where expressions of other units are associated with craters that excavate and expose underlying materials. The flow-like features, where hollows and associated halos are absent, mimic the basin floor. Areas of the flow-like features containing hollows and/or halos, however, are dominated by

units C and D, indicating that the presence of hollows is associated with relatively darker and smoother regolith. The lower character of the albedo is not expected and is counter to what is observed in the color analyses. However, the albedo values do overlap in range between the different units such that the hollows and halos have higher albedo values than adjacent terrains (**Figure 7**), but can (though not necessarily) differ in roughness and regolith grain properties (**Figures 8 & 9**).

The peak ring structures in the study areas are covered by a variety of clusters. The hollows within the peak ring are dominated by unit C, though units B and D are also present. The regolith within hollows are different from the regolith of the basin floor, but predominately in roughness (smoother). The properties of the halos vary between study areas, where in Area I they are dominated by unit C and in Area III they are dominated by unit B. Area II halos are a mix of units C and D. The walls and inter-peak terrains within the peak ring structure are a mottled mixture of all clusters, though the small portion of the peak ring present in Area III is dominated by unit C. This implies that the walls and inter-peak terrains may be influenced by halo-related materials.

The mesas topped with large hollows that are surrounded by halos in Area I display a mottled mixture of units D, B, and C (in the order of greatest to least abundant). The regolith at the top of these mesas is brighter and rougher than the basin floor (**Figures 7 & 8**), counter to the trends seen in **Figure 14**, but within the overlapping values with unit A. It is interesting to note that the K-means algorithm assigns the regolith of these mesas to properties more in align with the hollows than the basin floor regolith.

Area I also displays two anomalous regions (one to the north, top, and one to the south, center). The northern anomalous region displays some of the highest single scattering albedo values (**Figure 7**), but is assigned to unit B in the K-means analysis. This region is also associated with some of the roughest regolith (**Figure 8**) and more irregular and opaque grains (**Figure 9**). These properties are counter to the trends within the K-means clusters. The southern anomalous region does not display the high albedo of its northern counterpart, but it does display similarities in surface roughness and regolith grain characteristics. The K-means analysis shows this region is dominated by unit D with areas of unit B, indicating that the regolith properties fall in the extreme ranges of the parameter values of these clusters.

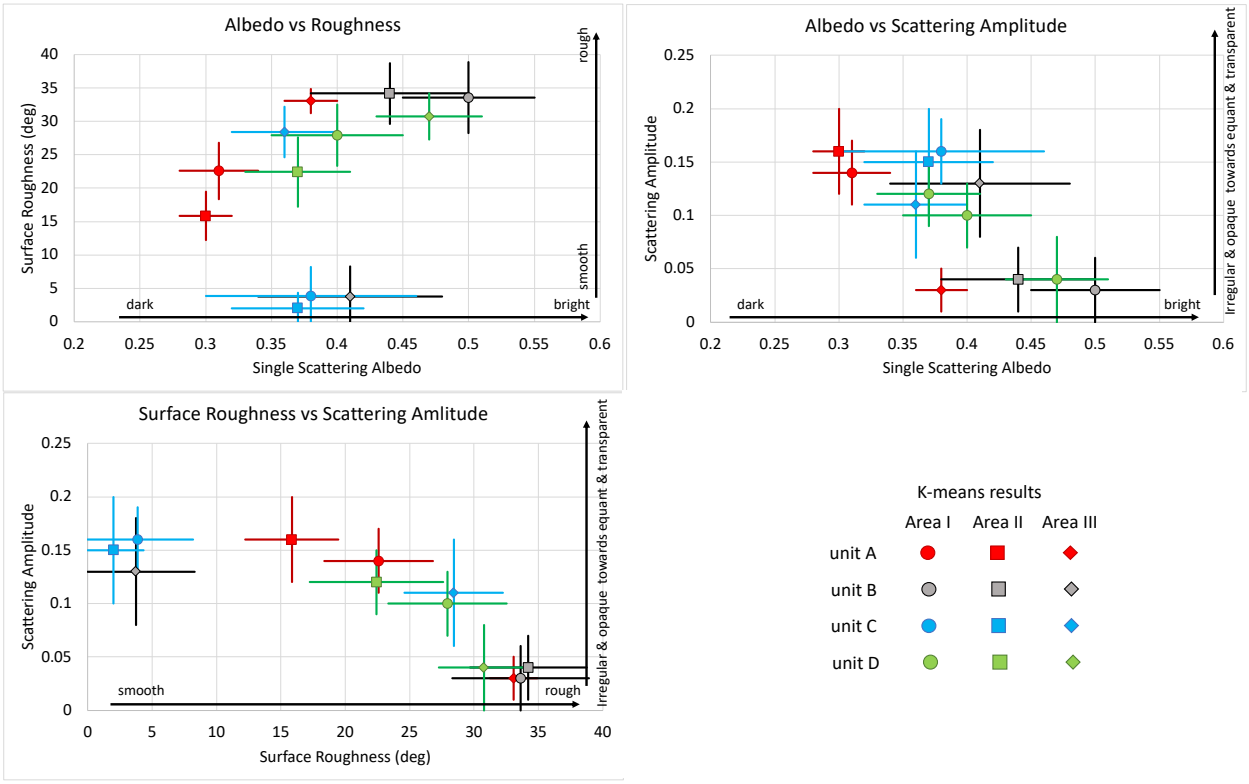

Figure 14. Comparisons of the parameter values defining each of the K-means clusters for each of the three study areas. There is significant overlap in parameter values, but the graphs display a grading of clusters into each other from unit A (red) to unit B (black/grey) to unit C (blue) to unit D (green).

To resolve ambiguities and inconsistencies in the association of photometric properties with geologic morphology from both the color and K-means analysis, we applied the MLC algorithm as described in Chuang et al. (2022, 2025) to the same data sets used in the K-means algorithm. The MLC algorithm is informed by both the color analysis and the K-means results. **This supervised** machine learning algorithms follows a task-driven approach that involves example data sets (referred to as training data) to define clusters. The training data are selected by the user in defined areas that best represent a given cluster unit based on the K-means results. Once training areas are selected, the data values within those areas are used to classify the remainder of the data set. In this study, training areas (**Figure 15**) were defined predominantly **from the** morphology and color (**Figures 11 and 14**). As the K-means results best defined four cluster units, we used the same four units for MLC which are: basin floor, flow, hollows, and halos. The MLC algorithm is one of several classification methods available in the Spatial Analyst extension package for ArcGIS Desktop. Area II was subdivided into two areas based on the differences in the color and subsequently the K-means analysis due to data quality difference, where a top portion (above the yellow line, **Figure 15**) and bottom portion (below the yellow line, **Figure 15**) were defined. Training areas in each portion were independently selected and analyzed with the MLC algorithm. The top and bottom portions of Area II were treated independently, as the relative variations are captured within each portion, but the data quality differences result in photometric parameters that do not correlate between the two portions, especially for the basin floor.

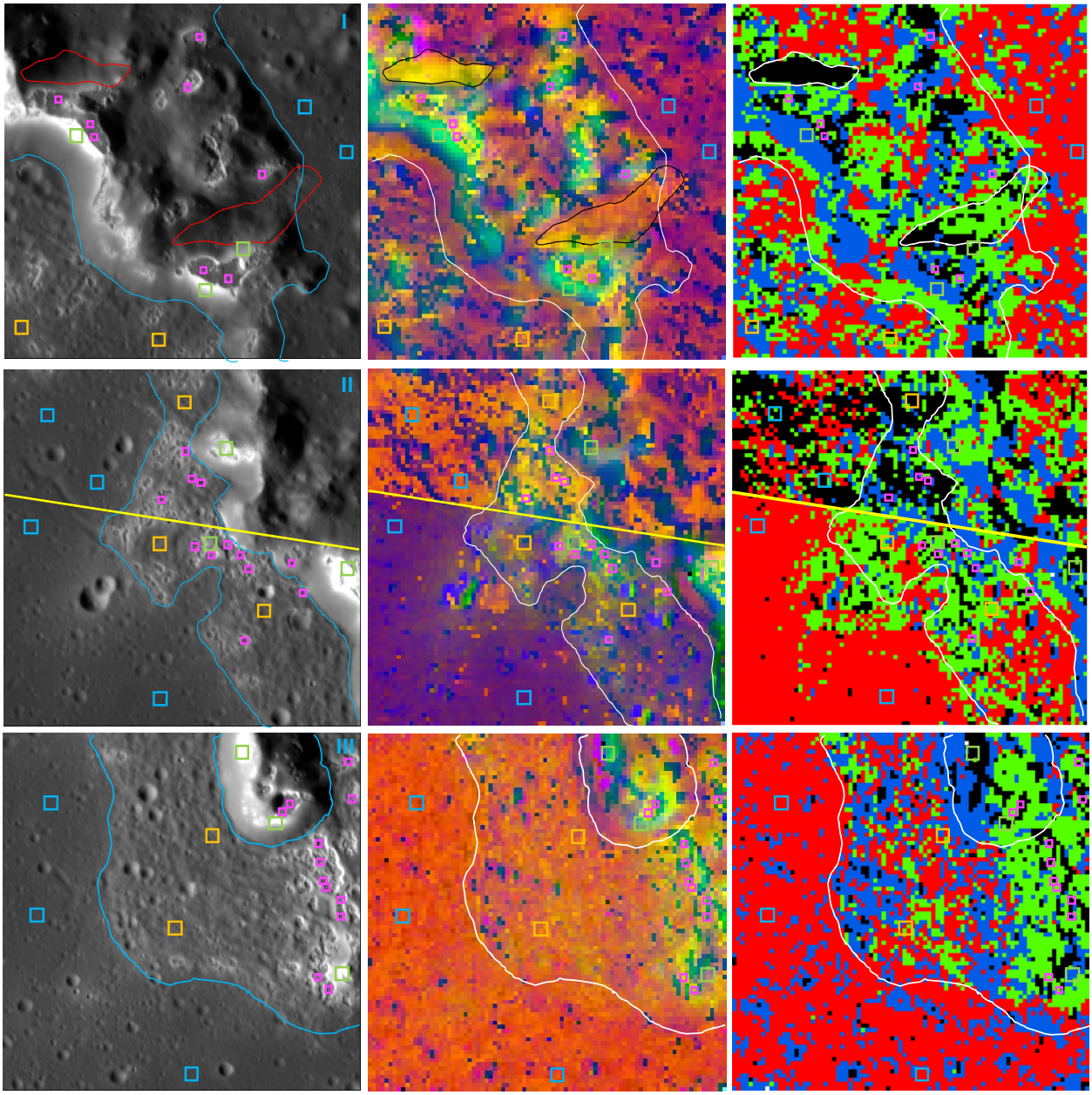

*Figure **15**. Training areas for the MLC analysis are outlined on the study areas (left column) and their corresponding locations within the photometric parameter color maps (center column) and K-means analysis (right column, see Fig. 16) are displayed for comparison. The training areas correspond to basin floor materials (blue boxes), glacier-like flow regions without the presence of hollows or halo materials (orange boxes), hollows (magenta boxes), and haloes (green boxes). The selected boxes are predominately based on morphology. Training areas for Area II (central row) were segregated into those from the top portion of the area (above the yellow line) and those from bottom portion of the area (below the yellow line) based on the differences in the color and subsequently the K-means analysis due to data quality differences.*

Examination of the resulting MLC cluster maps (**Figure 16**) provides some insight into the correlation of regolith properties with the **features in** these areas. Basin floor regions in each study area are dominated by the blue, basin floor cluster unit with small groupings of pixels from the other clusters. In Area I, there are groupings of pixels assigned to the hollows cluster that are associated with knobs and craters. Clusters of pixels extending from the peak ring structure onto the basin floor have been assigned to both flow and halo clusters in this study area. Similar trends are seen in the other study areas. The basin floor in the top portion of Area II is also dominated by the basin floor cluster, but craters and a rill are associated with groupings of halo cluster assigned pixels. The basin floor in the bottom portion of Area II is also, as expected, dominated by the basin floor cluster but pixel groups assigned to the hollows cluster are seen predominately associated with craters on the basin floor. There is a pair of superimposed craters on the basin floor in this portion of the study area that display pixels associated with the flow cluster interspersed with hollow cluster pixels and a small grouping of halo cluster pixels that merge into the flow-like feature. This may be indicative of the remnants of the ejecta blankets associated with these craters. The basin floor region in Area III, like in the other study areas, is dominated by the basin floor cluster with a large group of pixels assigned to the flow cluster that seem to extend from the flow unit and are associated with craters, including a pair of bright halo craters.

The flow-like features in all three study areas are dominated, as expected, by the MLC flow cluster. However, large portions within each flow-like feature show large groupings of pixels assigned to the hollows cluster in addition to smaller groupings assigned to both the halo and basin floor MLC clusters (**Figure 16**). Each of the flow-like features also contain hollows and associated halos, which are correlated with the location of the MLC hollow and halo clusters within the flow-like regions (see Area III). Study Areas I and II (top and bottom) flow-like regions are mottled with the MLC flow and hollow clusters, where the MLC hollows cluster is not only associated with hollows.

Table 3. Parameter values based on the MLC algorithm

Unit	Parameter	Area I	Area II (top)	Area II (bottom)	Area III
Basin Floor (Blue)	θ	22.17 ± 3.92	33.56 ± 7.03	38.38 ± 1.06	32.08 ± 4.26
	w	0.29 ± 0.02	0.53 ± 0.15	0.65 ± 0.06	0.56 ± 0.06
	b	0.10 ± 0.05	0.44 ± 0.24	0.66 ± 0.14	0.56 ± 0.17
Flow Materials (Orange)	θ	29.33 ± 7.55	29.62 ± 6.42	28.77 ± 13.53	33.72 ± 2.24
	w	0.48 ± 0.15	0.44 ± 0.09	0.56 ± 0.15	0.57 ± 0.07
	b	0.26 ± 0.25	0.16 ± 0.12	0.40 ± 0.23	0.47 ± 0.15
Halo Materials (Green)	θ	23.85 ± 16.5	$10.83^{+12.56}_{-10.83}$	$11.77^{+12.24}_{-11.77}$	18.46 ± 10.67
	w	0.57 ± 0.10	0.39 ± 0.13	0.43 ± 0.05	0.55 ± 0.16
	b	0.36 ± 0.23	0.21 ± 0.20	0.10 ± 0.05	0.49 ± 0.32
Hollow Floor (Magenta)	θ	17.30 ± 13.96	37.22 ± 3.47	24.42 ± 13.52	30.83 ± 7.44
	w	0.40 ± 0.10	0.68 ± 0.08	0.44 ± 0.12	0.62 ± 0.09
	b	0.13 ± 0.09	0.51 ± 0.15	0.28 ± 0.12	0.41 ± 0.19

Hapke parameter values and their standard deviations

The peak ring structure is a complex assortment of MLC flow, hollows, and halo clusters, with very few basin floor cluster pixels (**Figure 16**). The most extensive peak ring structure is seen in Area I. The mesas seen in this study area are associated with the MLC hollows cluster and the

bright regions surrounding hollows within the peak ring structure map as MLC halo clusters. The walls within the Area I peak ring structure are a combination of MLC flow and hollows clusters. In Areas II (top and bottom) and III, the peak ring structures map predominantly as MLC halo and hollow clusters. The anomalous regions in Area I do not stand out in the MLC maps. The northern anomalous region maps predominately as MLC hollows clusters and the southern anomalous region maps predominately as MLC flow clusters.

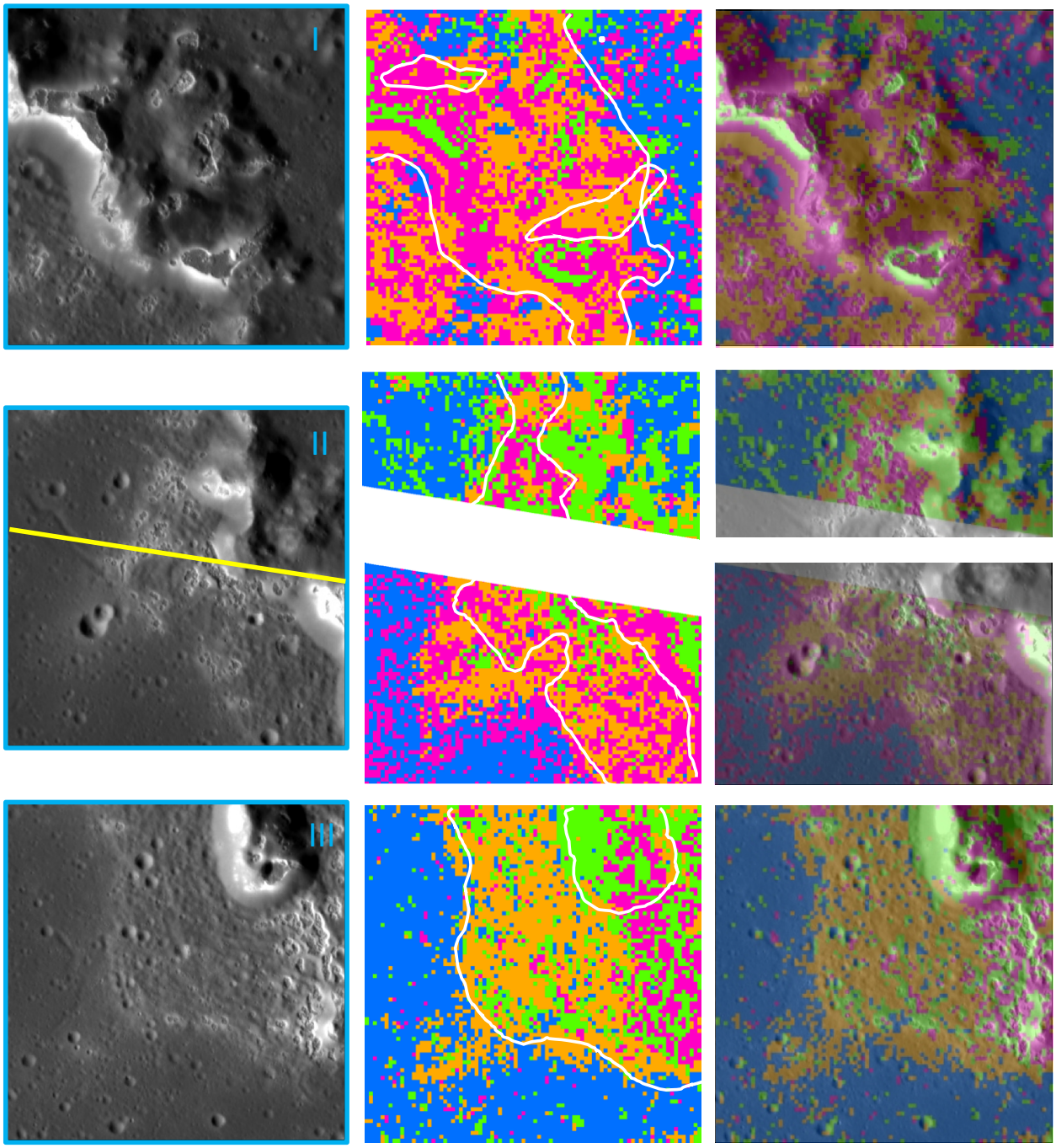

Figure 16. The MLC cluster unit maps for study Areas I (top), II (center), and III (bottom). The first column are grayscale reflectance images of each area, the central column are the MLC cluster unit maps with morphologic boundaries shown in white, and the right column is a transparent

overlay of the MLC cluster unit maps on top of the reflectance images. Area II has been divided into two portions (top with lower data quality, bottom with higher data quality). The center column shows no overlap in coverage, the right column has the overlap shown in greyscale. Each of these portions were examined independently. For the central and right columns: Blue = basin floor MLC cluster, orange = flow MLC cluster, magenta = hollows MLC cluster, green = halo MLC cluster. Refer to Table 3 for details on the parameter value ranges for each cluster unit.

The parameter values that correspond to each of the MLC clusters (**Table 3**) display many overlaps in values (**Figure 17**). Whereas the K-means clusters appear to grade into each other (**Figure 16**) the MLC clusters do not display as clear a gradation. The MLC basin floor cluster, with the exception of Area I, is representative of the brightest and roughest regolith with regolith grains more equant and transparent than the other MLC clusters. The MLC basin floor cluster in Area I, in contrast is darker, smoother, and represents grains with more irregular and opaque properties. It should be noted that the basin floor in Area I is exterior to the peak ring whereas this morphological unit is interior to the peak ring in the other study areas.

The MLC flow cluster displays a range of roughness values which overlap with those of the MLC basin floor cluster but also extends to smoother (lower) values. In contrast, the MLC hollows units span the entire range of roughness values. The MLC halo cluster represents some of the smoothest regions, which is consistent with the K-means analysis, even though the range of roughness values overlaps those of the MLC hollows units.

While the MLC basin floor unit is representative of high single scattering albedo values, the remaining clusters display the entire range of values in all the study areas. Albedo appears to distinguish basin floor regolith from the remaining morphological units, but is not a strong delimiter between these other morphological units. Similarly for the regolith grain characteristics, the MLC basin floor cluster is representative of some of the more comparatively equant and transparent grains whereas the other MLC clusters span the range of shape and opacity.

The plots comparing the photometric parameters for each MLC cluster (**Figure 17**) shows some linear correlations between parameters for some of the clusters. Since the basin floor in Area I is exterior to the peak ring, it is excluded from the examination of trends between parameters. The MLC basin floor cluster does not display a linear trend, it tends to group in regions of high albedo, rougher surfaces, and less opaque and more equant regolith grains (higher *b* values). The MLC flow unit, however, displays a linear relationship between single scattering albedo and scattering amplitude, where darker regolith is comprised of more opaque and irregularly shaped grains and brighter regolith is comprised of relatively more transparent and equant grains. There does not appear to be any correlations between surface roughness and either albedo or grain characteristics for the MLC flow cluster, thus grain size variations from the MLC basin floor cluster are not necessarily indicated. The MLC hollows and halo clusters, however, display correlations between all the photometric parameters. Both of these clusters show that darker endmembers are also smoother endmembers with more opaque and irregularly shaped grains and brighter endmembers are also rougher endmembers with less opaque and relatively more equant shaped grains.

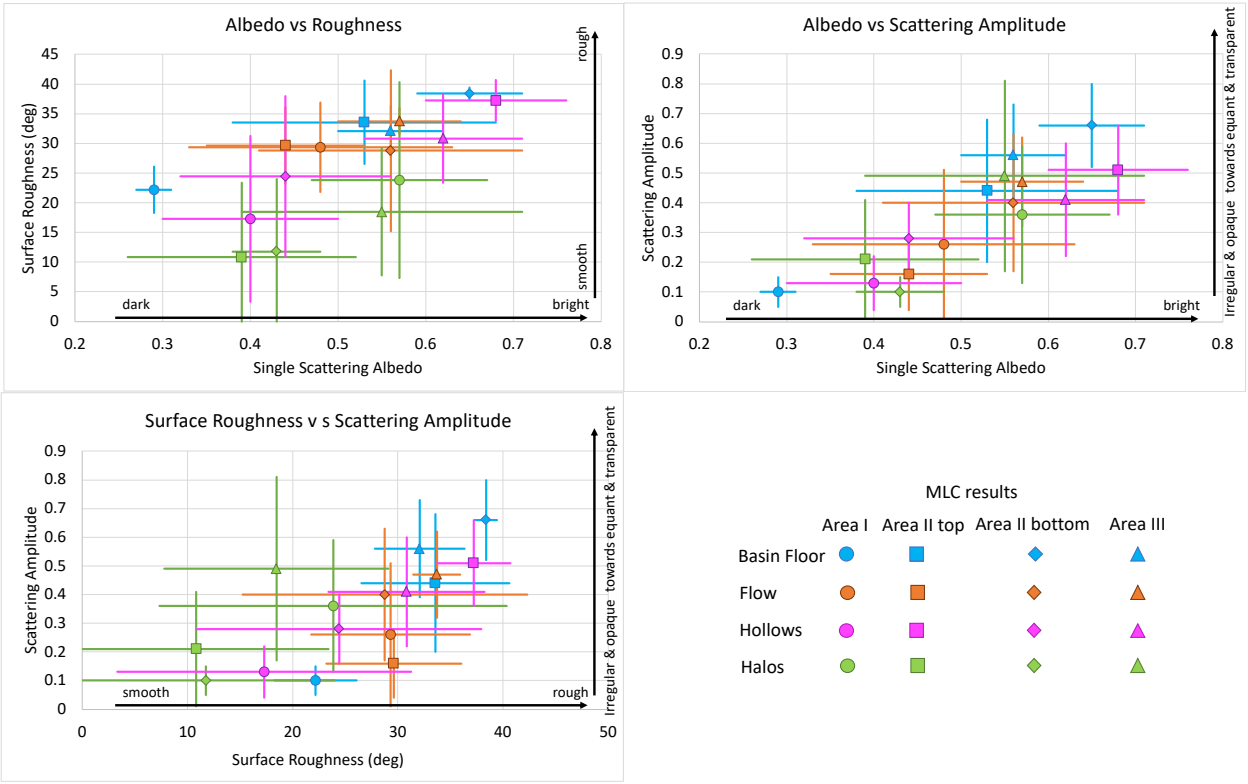

Figure 17. Comparisons of the parameter values defining each of the MLC clusters (Basin Floor, Flow, Hollows, Halos) for each of the three study areas (Area I shown in circles, Area II top shown in squares, Area II bottom shown in diamonds, and Area III shown in triangles). There is significant overlap in parameter values with some MLC clusters displaying linear trends between some parameters.

Implied Regolith Properties

Summary. The machine learning analyses each show that the basin floor regolith is distinct from the other morphological units (flow-like features, hollows, halos, peak ring structures), and that craters have exposed or excavated material that has similarities with the regolith associated with the flow-like features and hollows. Differences between the Area I exterior basin floor and Areas II and III interior basin floor indicated the regolith of the basin floor exterior to the peak ring structure is darker and smoother than the regolith of the basin floor interior to the peak ring structure. Both the K-means and MLC analyses show the interior basin floor is characterized by a comparatively brighter single scattering albedo and a rougher surface. The grain characteristics indicated by the two methods, however, are distinct. While the K-means parameter values and the median values from the morphological units plot similarly on the 'hockey stick' diagram, the MLC parameter values show a wider range (Fig. 18), reinforcing the results discussed above.

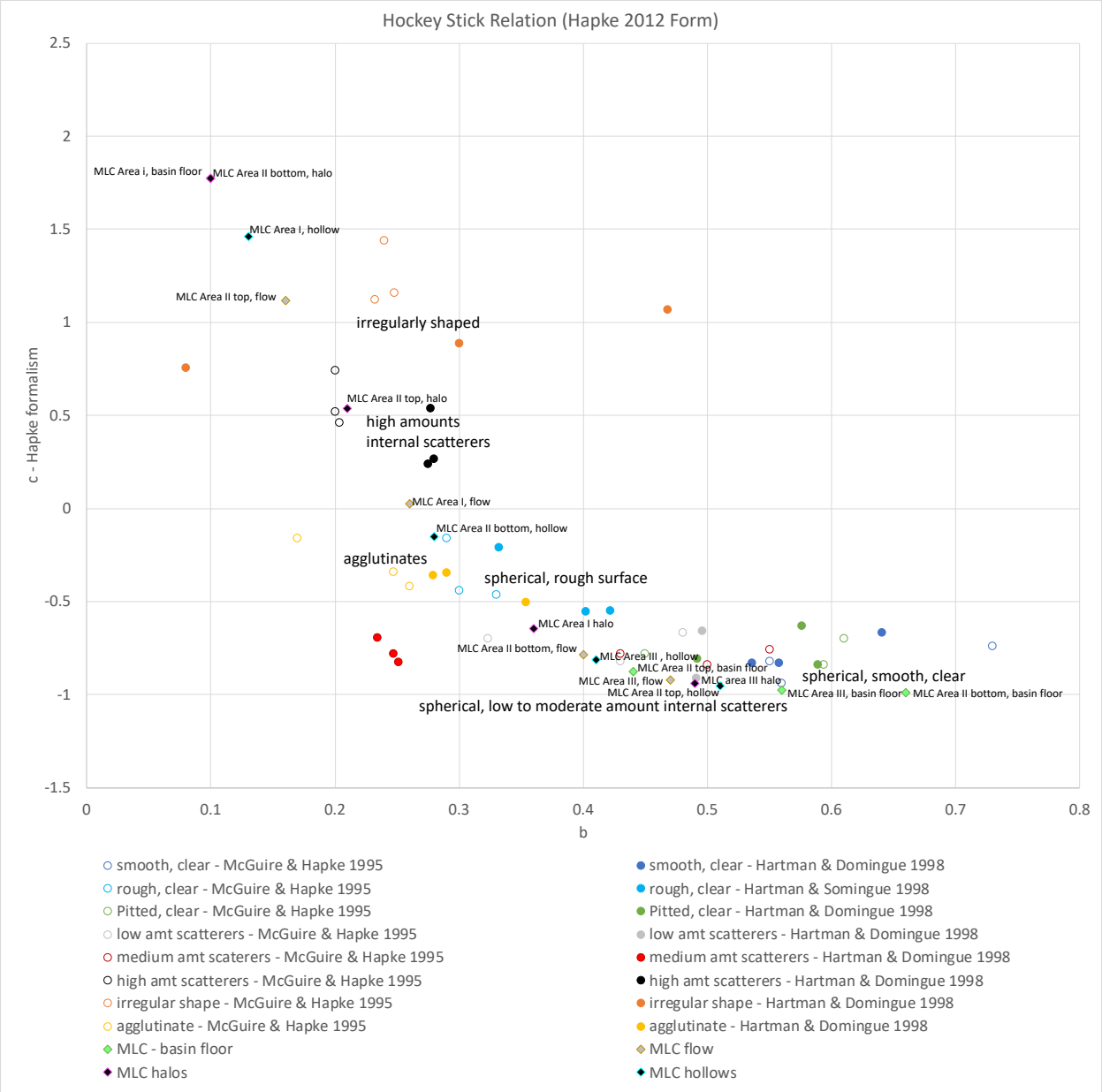

Figure 18. Hapke's 'hockey-stick' relationship (Hapke 2012b) between the scattering function amplitude (b) and the scattering function partition (c) parameters from the four MLC units from each study area compared to other Mercury studies and the laboratory measurements of McGuire and Hapke (1995) and the remodeling of those measurements by Hartman and Domingue (1998). Note that the 'c values' have been converted to match the formalism in Hapke 2012b due to the different formulation of the single particle scattering function, as discussed in section describing the Modeling Approach and Methodology. This diagram has been converted to match that in Hapke 2012b.

The flow-like features display more complex, less uniform regolith properties. While there are small clusters of basin floor-like regolith within this unit, the regolith is essentially divided into two types: 1) regolith inherent of the flow, and 2) regolith associated with hollows. The flow's

inherent regolith displays slightly lower single scattering albedo and slightly smoother roughness properties compared to the basin floor regolith. There appears to be a linear relationship between single scattering albedo and scattering amplitude, where lower albedo regolith grains are more irregularly shaped and opaque. In enhanced color images of the study areas, the flow-like features are a distinct color from the basin floor and hollows terrains (**Figure 19**). These color differences, derived from spectral properties, are diagnostic of compositional variations, though the exact compositions are not identifiable.

The single scattering albedo for the clusters associated with hollows cover the range of albedos from the modeling results. However, it is clear from the single scattering albedo maps (**Figure 7**) that the albedo of the hollows and associated halos is brighter (higher) than the surrounding terrains. The large extent of the clusters that correlate with these units across the surface indicate that the regolith characteristics of the hollows extend beyond their morphological boundaries. The photometric parameters for these clusters, in the MLC analysis, show linear correlations (**Figure 17**). The bright endmembers of this cluster are also rougher than the darker endmembers and share similarities in single scattering albedo and roughness with the basin floor regolith. They also share the same correlation between single scattering albedo and scattering amplitude as the flow-like features' regolith. The halos cluster displays the smoothest regolith, but shares the remaining characteristics as the hollows clusters.

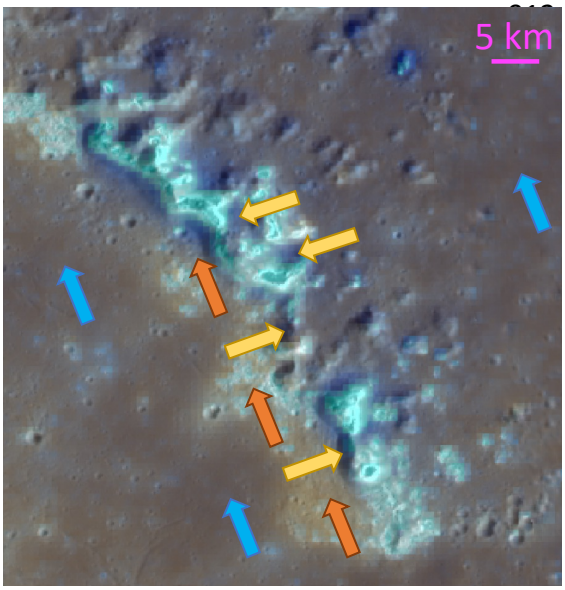

Figure 19. An excerpt from the enhanced color mosaic extracted from the MESSENGER Quickmap (https://mercury.quickmap.io). This color mosaic is based on principal component 2 (red channel), principal component 1 (green channel), and the 430/1000 nm reflectance ratio (blue channel). The hollows and surrounding halos appear light blue, the flow-like features appear light brown (orange arrows), the basin floor appears dark brown (blue arrows), and the peak walls appear to be a mixture of dark to light brown (yellow arrows), varying with location within the peak ring.

Grain Characteristics. The three comparative grain characteristics that can be examined here are composition, grain size, and grain structure (shape and internal inclusions). The color map (**Fig. 19**) suggests compositional differences between hollows and their halos that are distinct from all other morphological units in our study areas. The color differences between the basin floor, the flow-like features, and the peak walls are more subtle, suggesting the following: 1) morphological units with hollows have hollows material mixed in with a standard regolith component, and 2) there are potential grain size differences within the standard component of the different morphological units. The single scattering albedo, which is influenced by composition, grain size, and compaction, and the single particle scattering function amplitude (scattering amplitude), which

is influenced by the opacity and shape of the regolith grains, offer some insight into distinguishing between the options presented by the color properties.

Using the interior basin floor regolith as a benchmark, the exterior basin floor regolith is of similar color, therefore similar composition, but the single scattering albedo is lower and the surface is smoother than the interior basin floor regolith. The differences in albedo and roughness can be explained by differences in grain size and compaction (an inter-grain characteristic discussed below). A decrease in single scattering albedo can be produced by larger grain sizes in the exterior basin floor regolith compared to the interior basin floor regolith. The smaller grain sizes in the interior basin floor regolith may be produced by the preferential introduction of hollows-like materials. This interpretation is evidenced by the appearance of clusters associated with hollows on the basin floor, especially where there are craters evident. A layer beneath the interior basin floor, excavated by impacts, could introduce hollows-like material into the regolith.

Like the exterior basin floor regolith, the regolith of the flow-like features is comparatively smoother and darker in the areas not associated with hollows materials. The subtle difference in color suggests a difference in composition, but with common components to the basin floor regolith. Differences in grain size contributing to the albedo differences cannot be ruled out. Two mutually inclusive hypotheses are examined here in terms of the photometric properties: 1) the regolith of the flow-like features is a mixture of hollows and basin floor materials, or 2) the regolith of the flow-like features represents a younger, evolving surface where the basin floor regolith represents a desiccated, volatile-poor endmember.

The widespread presence of hollows-associated clusters in both the K-means and MLC maps of the study areas indicates that this geologic unit is an inherent part of the flow-like features and the processes forming them are affecting the regolith properties of the flows themselves. The origin of the flows from the peak ring, which includes a volatile rich layer (VRL) uplifted from depth (Rodriguez et al. 2023), suggests a mixing of the residual from the VRL after devolatilization with crustal components like those from which the basin floor, a volcanic unit derived from depth, originated. Smaller grain sizes of both components could contribute to the relative brightening of the flow-like features compared to the basin floor (**Figure 7**). However, the presence of both hollows-associated and flow-associated clusters on the basin floor correlated with impact craters suggest the presence of a layer beneath the basin floor with similar characteristics as the flow-like features. As this layer is exposed to the space environment on Mercury it evolves to a regolith like what is currently seen on the basin floor. The presence of hollows within the flow-like features suggests this morphological unit is still devolatilizing, but the presence of basin floor-associated clusters in regions of the flows with no hollows present indicates that the regolith of the flows is still maturing to an endmember state like that of the basin floor regolith.

Hollows and their associated halos are compositionally distinct from all other units, thus deconvolving grain size characteristics relative to the basin floor or flow-like features is not possible with the current data set. With the current data set, grain size differences can be inferred if similar compositions can be assumed. This is not the case when comparing the hollows and their associated halos with the other units in the study areas. However, comparisons can be made between these two units. In general hollows have slightly lower single scattering albedo than halos (**Figure 7**), but the MLC hollows cluster overlaps in albedo with the MLC halo cluster (mean values show the hollow cluster slightly brighter than the halo cluster). Halos display smoother surfaces than hollows (**Figure 8**). This implies that the grain sizes within the halo regolith is smaller than the near-by hollow regolith, commensurate with the deposition of a fine-grain material.

In Area I there are two 'anomalous regions' (one to the north and another to the south) that show unexpectedly high single scattering albedo values, high surface roughness, and low scattering amplitude compared to surrounding terrains. In reflectance images these areas do not appear anomalously bright nor distinct in morphology and are associated with inter-peak/peak walls. In the enhanced color images, they appear darker than the basin floor (interior and exterior), but are the same color as other areas bordering the peak walls (**Fig. 19**) that do not display anomalous photometric behavior. In the machine learning analyses these areas display regolith characteristics associated with hollows and the flow-like features, indicating regolith characteristics associated with volatile loss, suggestive of mass movement due to previous volatile content. The high single scattering albedo and surface roughness suggests relatively finer-grained, more compact but hummocky on micron-scale regolith. Finer-grains and lower porosity both contribute to increasing brightness (e.g., Clegg et al. 2014; Hess et al. 2023), but the higher surface roughness indicates the surface is more hummocky than the basin floor or flow-like features on scales of the observational wavelengths.

Inter-grain Characteristics. The relationship between regolith grains, referred to as inter-grain characteristics, is predominantly a combination of compaction/porosity and average tilt to the surface or surface roughness. This relationship is captured in comparative values of the surface roughness parameter and influences differences in the single scattering albedo. The compaction of a surface has been shown to brighten a surface (Clegg et al. 2014, Wu and Hapke 2018, Hess et al. 2023). Thus, smoother surfaces, which are also brighter, may represent regolith where the pores have been in-filled with smaller particles to produce a more compact yet more diverse grain size distributed regolith.

The difference between the interior and exterior basin floor suggests larger grain sizes in the exterior, but also supports a more porous regolith in the exterior. The albedo and roughness differences could be the result of the pore space of the interior basin regolith being filled-in with smaller grains, for example due to seismic shaking by the formation of the impact crater near the basin center or regolith movement during the extensional feature formation within the interior basin floor. The photometric properties of the flow-like features also indicate that this morphological unit may also be more compact, with small grains filling in pores. This infilling of pore space is supportive of the presence of interactions with volatiles and the residuals left from their removal.

The smoothest morphological units in the three study areas are the halos. They, along with the anomalous regions, are the brightest units and contain the relatively least opaque materials. The halos are suggestive of bright, fine-grained materials, that are relatively more compact than the other morphological units. The hollows are, as stated above, darker and rougher than the halos, implying that the regolith within the hollows consist of larger particles and are less compact than the halos.

In contrast, the anomalous regions, while having similar single scattering albedo values to the halos are some of the roughest morphological units, supporting a more hummocky terrain. The lack of a color signature correlated to these units suggest that these properties are related to grain size and compaction differences and not compositional differences. The smaller values of the single particle scattering function amplitude, however, indicates a difference in opacity and grain shape from the regolith in the other morphological units. The difference in opacity could be created by more scattering centers in the grain structure, such as bubbles, cracks, or inclusions rather than a difference in composition.

Surface Process Implications

The processes occurring in the three study areas examined include impact cratering which formed the Raditladi basin, volcanism which formed the current-day basin floor, sublimation which is responsible for the hollows and their associated halos, and glaciation/mass wasting that formed the flow-like features, mesas, and terrains within the peak ring structure. There are regolith characteristics within each morphological unit (basin floor, flow-like features, hollows and halos, peaks and inter-peak terrains) that are tied to the presence of volatiles; thus we begin by following the evolution of the proposed VRL (Rodriguez et al. 2023) within the regolith.

Rodriguez et al. (2023) proposed that the impact that formed the Raditladi basin uplifted a pre-existing VRL and exposed this layer within the peak ring system but removed it from the basin floor regions, demonstrated via impact modeling. The flow-like features are a result of the movement of this exposed VRL. The current presence of hollows within these flow features, attest to a continued presence of volatiles in recent geologic history. In addition, the formation of the glacier-like flows explains the presence of mesas within the peak-ring structure (Rodriguez et al. 2023). The flows occurred after the volcanic emplacement of the basin floor (Blair et al. 2013), however the presence of regolith exposed by subsequent impacts into the basin floor that share photometric properties with the regolith associated with hollows and the flows (i.e. cluster in the machine learning applications with hollows and flow units) implies the existence of a buried layer containing volatiles. Two scenarios could explain the presence of these buried volatiles. The first postulates that volatiles sublimated from the peak ring onto the ancient basin floor and were subsequently buried by the volcanic events that formed the current day basin floor. The buried volatiles were later exposed by impacts. The second follows a concept proposed by Vaughan et al. (2012), where the impact melt may have differentiated, forming a sulfide or chloride rich layer, which was not exposed at the surface, but was exposed by subsequent cratering events.

The color and photometric properties suggest that the basin floor regolith is larger-grained and less compact than the flow-like features. The regolith covering the flow-like features, however, is non-uniform, showing small areas commensurate with the basin floor, areas unique to the flow, and areas with regolith common to hollows and halos. This mixture of regolith characteristics implies an evolution from young, hollows-like regolith to mature basin floor regolith. The regolith inherent or unique to the flow-like features represents a regolith of potentially intermediate maturity, showing finer, more compact properties compared to the basin floor. The flow-like features are characterized by the presence of hollows (some with halos) whereas the basin floor is devoid of hollows (Rodriguez et al. 2023). The color suggests that the two morphological units have some compositional components in common. The photometry is highly suggestive of the presence of hollows and halo materials intermixed with the common compositional component. The scattering amplitude also suggests that the basin floor may be more space weathered, implying a longer exposure time or older age compared to the flow-like features. This age is commensurate with the paucity of craters on the flows (Rodriguez et al. 2023).

If the hollows are formed via the sublimation of a VRL, the regolith structure could provide insight into the sublimation process. Sublimation is the phase change from solid to gas without passing through the liquid phase, and depending on the material composition, is dependent on temperature and pressure. On Mercury we have the solar heating of the surface, where daytime maximum surface temperatures range between ~700 K at the hot poles, ~675 at the warm poles, and ~400 K at the polar latitudes (Bauch et al. 2021; Deutsch et al. 2025) and nighttime temperatures drop to ~100 K. Without an atmosphere, the surface is also exposed to the vacuum

of space. A rapid, energetic sublimation process will be disruptive of the interparticle relationships, causing motion of the finer-grained components, collapsing structures and in-filling vacancies thereby compacting the surface. This can be envisioned where there are large, continuous segments of volatile material with unshielded heating pathways exposed to the surface, with little non-volatile material entrained with the volatile component. The energetic, potentially explosive devolatilization (Xiao et al. 2013) will either eject the finer-grained particles, or shake the regolith such that these finer-grained constituents fill in pore spaces. A gradual, slow, less energetic sublimation process will be less disruptive of interparticle relationships. This can be envisioned where the VRL is an intimate mixture of both volatile and non-volatile components, even with volatile and non-volatile components comprising the same grain, where heating pathways exposed to the vacuum of space for the volatile component are limited. The less energetic sublimation will limit motion/removal of finer grains and preserve the smaller pore spaces or vacancies created by the removal of the volatile. The finer-grained, more porous regolith indicated by the photometry thus supports a gradual, slower, sublimation process. The sublimation process is halted by either the depletion of the VRL, which leaves a non-volatile remnant or lag, or the formation of a residual lag, which forms a barrier between the VRL and the environment. Because any lag material would be the top surface, which is what is sensed and described by the photometric results, it would govern the hollow scattering properties; thus, the albedo, opacity, particle shape, and surface roughness are descriptive of the lag material. This compares well with the hollow development stages that have been proposed (Blewett et al. 2018; Deutsch et al. 2025).

The photometric modeling indicates the hollows floors are rougher than the halos based on the surface roughness parameter, but are comparable to or slightly smoother than other geomorphic units, with the exception of the anomalous regions. A slow sublimation rate is less disruptive of the regolith grains, retaining inter-grain relationships and finer-grained components while removing material, and is photometrically associated with more compact, finer-grained regolith. A rapid sublimation rate is more disruptive, where large volumes of volatiles are removed, potentially entraining and thus removing the finer-grained components, and inter-grain relationships are altered by motion of the lag materials though the volatile removal processes resulting in a relatively coarser grained and more porous regolith. The photometric properties of the bright endmembers in the hollows clusters are indicative of finer-grained more porous regolith, commensurate with a slower, less disruptive sublimation rate; correlating in location to the morphology associated with hollows.

The regolith structural differences between halos and hollows provide some constraints on their relative formation. It has been proposed that halos are potential deposits of material removed from the hollows floors and redeposited adjacent to the source, and with time, these materials are space weathered and become indistinguishable from the surrounding terrain and regolith (Blewett et al. 2016, 2018). Compared to the hollows floors, halos display similar or higher (brighter) single scattering albedo, smoother interparticle/surface roughness, and are less opaque and irregularly shaped then the hollow floor regolith. The brighter single scattering albedo and similar color properties suggests the halos have a similar composition to the hollows but are comprised of smaller grains. The smoother surface roughness suggests a more compact regolith, where tilts between grains are shallower. This may follow if halos represent the initial stages of hollow formation. In the first stage of formation exposure and heating of the VRL results in a slow, gradual removal of material, where the intimate mixture of volatiles and refractory elements are gently removed from the surface. The volatile component escapes to the exosphere, and the heavier, fine-grained refractory component is deposited near the initial exposure site. As material is removed,

depressions form to create the hollow feature. As the hollow deepens, the mixture of gently escaping volatile and fine-grained refractory material fall back to the floor of the hollow (there is insufficient energy to scale the walls of the pit). The fine-grains mix with the larger grains that are not lofted by the initial sublimation process, but create a rougher surface than observed for the halos. This is commensurate with the 'Stage 1' development described by Blewett et al. (2016, 2018) and examined by Deutsch et al. (2025).

The most unexpected result was the discovery of the anomalous regions in Area I. These are regions within the peak ring system, along the walls of peaks within the ring. They have single scattering albedos comparable to the hollows and their halos and surface roughness values and single particle scattering function amplitude values are among the highest in the three study areas. The color mosaics do not show any distinctive color for these regions, suggesting they are not compositionally distinct from other inter-peak terrains. This compositional homogeneity suggests that these regions have a fine-grained regolith, in comparison to the other morphological units, a rougher/more tilted surface (comparatively more hummocky) that is indicative of a more porous regolith, and grains that are more opaque and less equant than elsewhere in the study areas. They are potentially areas of glacier-like flow or mass movement of material from the peaks. They are associated with peaks with flat tops (mesas) and could represent the remnants of the VRL that flowed from the peaks into the peak ring construct rather than over the basin floor. The color and photometric properties of these areas suggest that the lag from the VRL contains a compositional component in common with the general regolith.

Hollow and halo formation: Given the particle properties and size variations implied by the photometric results, we compare some possible mechanisms for the formation of and relationship between hollows and halos. This begins with the assumption that the formation of halos is the initial hollow formation step, where the sublimation process begins with the removal of the volatile component and the subsequent movement of the associated, non-volatile materials (hereafter referred to as lag material) to form the bright halo. The scenario assumes that halos consist of fine-particles of lag material that were ejected from the sublimating hollow region in many 'popcorn' events. We assume a particle in a hollow consists of a mixture of volatile and lag material, and energy is deposited into the particle sufficiently rapid to cause the volatile to sublimate, giving a 'kick' to the remaining lag component, and ejecting the lag component along a ballistic trajectory to form the halo. As the sublimation process proceeds, material is loss from the hollow region, by both the sublimation of the volatile and the ballistic removal of the smaller size fraction of the lag material, eventually forming a depression (hollow) surrounded by a fine-grained deposit of lag material (halo). This scenario is depicted in **Figure 20**.

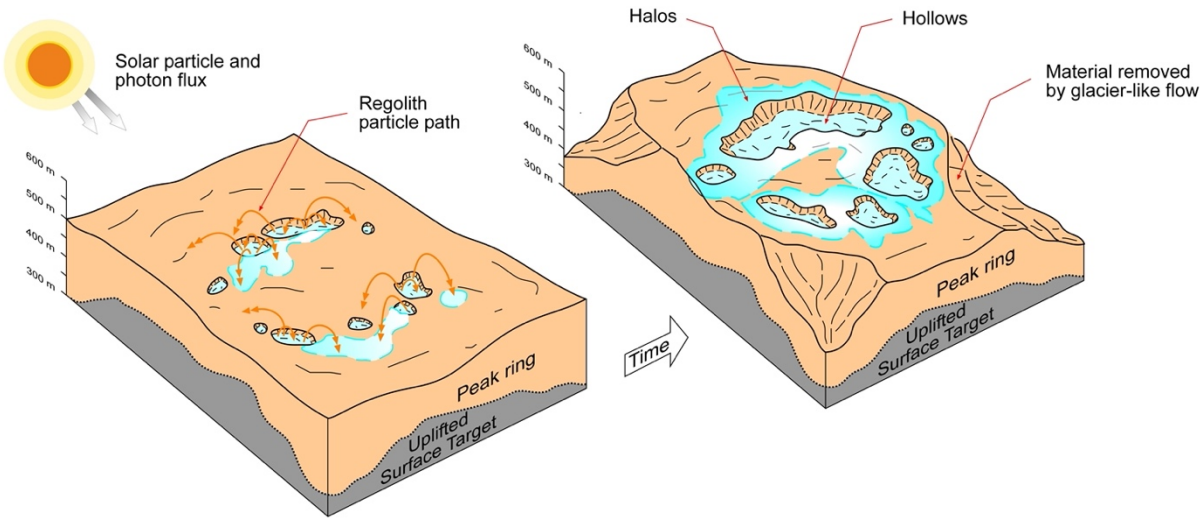

Figure 20. Schematic of the initial formation of halos through the popcorning of grains and the subsequent evolution and development of hollows. The sublimation of the volatile portion of intermixed grains removes regolith particles along ballistic trajectories (orange lines) to form deposits categorized as halos. As material is removed depressions are formed and with time grow to become hollows features, making halo formation the initial stage of hollows development, a precursor to the 'Stage 1' hollow development (e.g., Deutsch et al. 2025). This scenario depicts halo and hollow formation within the peak ring, which also experiences mass wasting due to glacier-like flows described by Rodriguez et al. (2023). The peak ring is uplifted material that forms a distinct surface feature.

Two mechanisms for inducing the sublimation event are examined, solar wind particle radiation and solar UV photon bombardment, to explore if the energies associated with these processes could impart sufficient energy to move material to form the halos. We also assume that the energy of dissociation is equivalent to the energy needed for moving material. The energy of dissociation for some candidate materials are listed in **Table 4**. The energies range from ~3.6 to 5 eV/molecule, which is not a large spread of energies, *i.e.* they are sufficiently similar. For the example described below, the dissociation energy for NaCl is used, as it is in the middle of the energy range and has been suggested as a plausible material for the glacier-like flows (Rodriguez et al. 2023).

Table 4. Dissociation Energies for Materials Associated with Hollows

Material	Energy (kJ/mole)	Energy eV/molecule
Halite (NaCl)	411	4.26
Sodium Sulfide (NaS)	360	3.73
Potassium Cloride (KCl)	436	4.52
Magnesium Sulfide (MgS)	346	3.59
Calcium Sulfide (CaS)	482	5.00

For a first order calculation we begin by assuming the ejected lag particles are of approximately the same small size. If the ejection velocity can be determined, then the kinetic energy can be

calculated and compared with the energy deposited in the volatile portion of the original volatile plus lag material grain. The ballistic trajectory, given no atmosphere, is defined by

$$X = V * t * \cos(\beta)$$

$$Y = V * t * \sin(\beta) - \frac{gt^2}{2}$$

Where X and Y are the range and altitude, respectively, V is the magnitude of the ejection velocity, t is the time, g is the gravity coefficient (3.7 m/s^2 for Mercury), and β is the angle of ejection with respect to the plane of the surface. The angle β is assumed to be random between 0º and 180º and the altitude Y equals zero at t = 0 and. From this we can correlate the distance X and associated velocity, V, from

$$X = \frac{2V^2}{g}\sin(\beta)\cos(\beta) = \frac{V^2}{g}\sin(2\beta)$$

$$V = \sqrt{\frac{gX}{\sin(2\beta)}}, \text{ where } \beta \text{ is } >0.$$

Hollow depths are estimated at 24 m ± 16 m (Blewett et al. 2018) and their lateral extent varies from 10s of meters to kilometers. For our regions in Raditaldi, the radius of hollows is ~137 m (Rodriguez et al. 2023). As a first order calculation, we can use X = 137m and β = 45º as an average angle to give a velocity of V = 22.5 m/s. The ejection energy, E_j, is then calculated from

$$E_j = \frac{1}{2}mV^2 \sim 3.44 * 10^{-4} J = 2.15 * 10^{15} eV\ ,$$

assuming a 1-mm diameter particle with a density of 2.59 g/cm^3 (density assuming CaS as the lag material).

There can be considerable variation in this result, as larger particles and/or shallower angles would yield larger ejection speeds. The fine-grained portion of the lunar regolith is considered to be < 100 μm (e.g., Taylor et a. 2010). **Table 5** lists estimates for E_j for a range of sizes, including those typical of lunar fine-grains. Cintala et al (1992) shows that Mercury's regolith can be expected to consist of grains sizes typical or smaller than the lunar surface. Alternatively, as hollows begin as smaller radii depressions, and most ejections would most probably occur at mid-range average angle values, the average ejection speed could be less than assumed above. Once grains are ejected, further movement could occur within the halos from impact of UV or solar wind particles. E_j is a typical energy range our model suggests for removal of a single grain by the 'popcorn' effect.

Table 5. Ejection Energy Estimates for Different Grain Sizes

Grain diameter	E_j (eV/d^2)*	ρ_{uv+} (eV/d^2/s)*	Thermal diffusion timescale (sec)
1 mm	2.15 x 10^{15}	4.5 x 10^{15}	1
0.5 mm	2.68 x 10^{14}	1.13 x 10^{15}	0.25
100 μm	2.15 x 10^{12}	4.5 x 10^{19}	0.01

50 μm	2.68 x 10^{11}	1.13 x 10^{19}	2.5 x 10^{-3}
25 μm	3.35 x 10^{10}	2.82 x 10^{18}	6.25 x 10^{-4}
10 μm	2.15 x 10^{9}	4.5 x 10^{17}	10^{-4}

**d is the diameter corresponding to the grain size listed in the first column*

Mapping of hollows has shown they preferentially occur on Sun-facing slopes (Blewett et al. 2013, 2011; Thomas et al. 2014), indicating that solar irradiance is a possible driver for devolatilization, especially by UV and shorter wavelength components (hereafter denoted as UV+ photons, wavelengths < 400 nm) of the solar photon output. The input energy density at Mercury from the Sun, ρ_{uv+}, from UV+ photons can be estimated by

$$\rho_{uv+} = R_{ME2} * f_{UV+X} * E_{solar\_spectrum}$$

where f_{UV+X} is the fraction of UV+ energy in the solar spectrum and $E_{solar\_spectrum}$ is the solar spectrum energy at Earth orbit (~1372 W/m^2), and R_{ME2} is the square of the ratio of Mercury AU to Earth AU. Solar UV photons comprise ~7% of the solar output (Stamnes 2003); X-rays and shorter wavelengths comprise ~1% of the solar output (Stamnes 2003). The ρ_{uv+} for Mercury is estimated then as ~1372 W/m^2 * (1AU/0.39AU)^2 ~ 9020 W/m^2, with 8% of these from UV+ photons (Meftah et al 2018), giving ρ_{uv+} ~ 721 W/m^2 = 7.21 x 10^{-4} W/mm^2 = 4.5 x 10^{15} eV/mm^2/s, which is more than twice as large as E_j for 1 mm size particles.

Another way to estimate ρ_{uv+} is through estimating number of photons. Energy in the solar spectrum for wavelengths > UV have energies < 3 eV. Using 3 eV means $N_{photons}$ = 1372 W/m^2 / 3 eV/photon = 1.372 x 10^{-3} J/s/mm^2 * 6.24 * 10^{18} eV/J / 3 eV/photon = 2.85 x 10^{15} photons/mm^2/s. Scaled to Mercury's orbit, $N_{photons}$ becomes 2.85 x10^{15} photons/mm^2/s * (1AU/0.39AU)^2 = 1.87x10^{16} photons/mm^2/s. UV+ photons at 8% of total = 1.87 x10^{16} * 0.08 = 1.5 x 10^{15} photons/mm^2/s. UV photon energy ranges from 3.1 to 12 eV (Stamnes 2003) and X-rays have energies > 12 eV. Using 8 eV for an average energy for UV photons and a low estimate of 12 eV for X-ray and shorter wavelength photons, $E_{aveUV+X}$ can be estimated by (8.eV *7%+12 eV*1%)/0.08 = 8.5 eV. This gives a value for ρ_{uv+} of ~12.7 x10^{15} eV/mm^2/s, which is ~3 times larger than the previous estimate of 4.5 x 10^{15} eV/mm^2/s. To be on the conservative side, we take the smaller of the two estimates. **Table 5** lists the ρ_{uv+} for areas corresponding to the particle sizes listed in the table, showing that the ρ_{uv+} values are greater than the E_j energies for particles as large as 1 mm.

Additional energy could be added to the system from the longer wavelengths of the visible range, though these photons would carry less energy (~1.6 – 3 eV; Meftah et al 2018) but would be much more plentiful. Solar photon radiation would then work to deepen and widen the hollows, but would be the most active during the part of Mercury's orbit having the greatest exposure to the Sun's radiation. However, a 'popcorn' event would need to occur on a sufficiently rapid timescale to prevent thermal energy loss. Thermal diffusion would remove energy quickly for small grains. The thermal diffusivity, κ, for many rock minerals is ~ 1 mm^2/s. The thermal diffusion time scale for a diameter, d, grain would then be $t \sim d^2/\kappa$, which is 1 second for a 1mm grain and 0.01 seconds for a 100μm grain (**Table 5**).

Another source of energy is the solar wind, which is comprised of ~95% protons, ~4% alpha particles, and the remaining ~1% are electrons and other ions (Ogilvie & Coplan 1995). The speed of the solar wind particles, v, is on the order of ~ 500 km/s and the particle density, ρ_{swp} is about

20 – 65 particles/cm^3 at Mercury's average orbital distance. The number density (protons/mm^2/s), N_{swp} is then given by

$$N_{swp} = v * \rho_{swp}$$

which is equal to 3.25 x 10^7 particles/mm^2/s assuming a value for ρ_{swp} of 65 particles/cm^3. The kinetic energy of a solar wind particle, E_{swp}, is derived from

$$E_{swp} = \frac{1}{2}mv^2$$

For simplicity, we assume all the particles are protons, the mass of a proton in 1.67x10^{-27} kg, giving a E_{swp} = 2.088 x 10^{-16} J = 1.3 x 10^3 eV. The speed of protons in the solar wind occurs over a range, so the energies will also spread over a range, but this provides an order of magnitude estimate.

The energy flux, ζ, for these protons is given by

$$\zeta = N_{swp} * E_{swp}$$

Giving, for this example, ζ = 4.225 x 10^{10} eV/mm^2/s. The time needed to accumulate the ejection energies, E_j, listed in **Table 5** are given in **Table 6** and are calculated by the deposition time, τ = E_j/ ζ. These calculations, however, do not include accounting for the shielding of the surface from the solar wind by Mercury's magnetic field. In all cases, the deposition timescales indicate that the effects of solar wind proton bombardment will affect only the micron or smaller grains, if any.

Table 6. Deposition time for meeting ejection energies by protons

Grain diameter	E_j (eV)	Deposition time
1 mm	2.15 x 10^{15}	14.1 hrs
0.5 mm	2.68 x 10^{14}	7.05 hrs
100 μm	2.15 x 10^{12}	1.41 hrs
50 μm	2.68 x 10^{11}	42.3 min
25 μm	3.35 x 10^{10}	21.1 min
10 μm	2.15 x 10^9	8.48 min

Another energy source for energetic protons is solar flares. The frequency of solar flares follows the Sun's 11-year cycle. These are categorized (A, B, C, M, and X) according to energy flux, where X flares are the most intense, emitting >10^4 W/m^2 (Tandberg-Hanssen & Emslie 1988). Within each category there are 10 energy levels, wherein an X3 flare is three times the intensity of an X1 flare. During solar maxima, flares can occur several times a day, where the most intense flares occur at ~8/cycle and the least intense can occur over 1000 times in a solar cycle (Veronig et al. 2002). Flares typically last several minutes, sometimes up to an hour or more (Reep and Knizhnik 2019). An extremely intense solar flare (X class) could eject protons of sufficient energy (many MeV to GeV; Crosby et al. 1993; McGuire and von Rosenvinge 1984) that would reach or exceed E_j. The most intense recorded flare had an estimated X-ray flux of ~45X1, that is, 4.5 x 10^{-3} W/m^2 at Earth's orbit (Curto et al. 2016), which would be equivalent to 1.755 x 10^{11} eV/mm^2/s

at Mercury's orbit. This is much lower than the 2.15 x 10^{15} eV/mm^2/s needed to eject a 1-mm lag grain or any of the grain sizes listed in **Tables 5 and 6**.

Popcorning the smaller grains from the hollow area is a mechanism to form the halos, a hallmark of the initiation of hollow formation. This segregates the finer-grains to the halos and larger grains to the hollows, as indicated in the photometric properties. However, as the hollow widens and deepens, not all 'popcorned' grains will be ejected from the hollow, some will follow trajectories that will land inside the hollow, even from grains that originate from the hollow walls. This will slow and eventually halt the halo formation.

On average hollows are ~24 m ± 16 m deep (Blewett et al. 2018), which may be limited due to lag build-up. Rodriguez et al. (2023) demonstrated that the thermal surface wave penetrates no more than ~ 3 – 5 m. If this thermal penetration depth is used as the lag deposit thickness, then the amount of volatile lost from a hollow could be estimated as a function of halo thickness and porosity using the following relations:

$$f_v + f_{nv} + \phi = 1$$

$$f_{nv} * (D + L) * A = (1 - \phi)L * A + a_h * z_h$$

$$f_v * (D + L) * A = (1 - \phi)D * A - a_h * z_h$$

where f_v is the volatile fraction, f_{nv} is the non-volatile (lag) fraction, is the porosity, D is the depth of the hollow, L is the lag thickness at the bottom of the hollow, A is the area of the hollow floor, a_h is the area of the halo, and z_h is the thickness of the halo. **Table 7** shows some estimates for volatile vs lag material abundance, as a function of porosity and halo thickness, assuming an average hollow depth of 24 m, a lag thickness of 4 m (average thermal penetration depth), a hollow radius of 137 m, and a halo area half the hollow area. The volatile content varies ~8% over the halo thickness between 0.5 – 5 m, regardless of porosity. Volatile content decreases as halo thickness increases or as porosity increases. As porosity increases the difference between volatile and lag content decreases. Constraining the porosity and halo thickness will provide needed constraints for determining the volatile content associated with hollows formation, and will perhaps be provided by the upcoming BepiColombo observations.

Table 7. Volatile content estimates

Porosity (%)	z_h (m)	f_v (%)	f_{nv} (%)
10	0.5	76.3	13.8
	1	75.4	14.6
	2	73.6	16.4
	3	71.8	18.2
	4	70	20
	5	68.2	21.8
20	0.5	67.7	12.3
	1	66.8	13.2
	2	65	15
	3	63.2	16.8
	4	61.4	18.6
	5	59.6	20.4

30	0.5	59.1	10.9
	1	58.2	11.8
	2	56.4	13.6
	3	54.6	15.6
	4	52.9	17.1
	5	51.1	18.9
40	0.5	50.5	9.5
	1	49.6	10.4
	2	47.9	12.1
	3	46.1	13.9
	4	44.3	15.7
	5	42.5	17.5
50	0.5	42	8
	1	41.1	8.9
	2	39.3	10.7
	3	37.5	12.5
	4	35.7	14.3
	5	33.9	16.1

Conclusions.

The regolith properties derived from this photometric study provide a few insights into the processes involved in hollows formation and the VRL associated with their presence within the Raditladi basin. The hollows are associated with finer-grained more porous regolith, indicative of a slower, less disruptive sublimation rate. The implication is that the volatiles are removed from the surface slowly, over a long period of time. The residual, or lag, that remains after sublimation is fine-grained and porous and it represents one component of the mixture of materials in the regolith of the flow-like features, the other component sharing a commonality with the basin floor. Hollows are an inherent part of these flows, and their presence indicates the recent, and possible current, existence of volatiles within them.

The flow-like features originate from the peak ring, which includes a VRL uplifted from depth during the impact forming event (Rodriguez et al. 2023). Sublimation of volatiles from the peak ring may have deposited on the floor prior to the volcanic events that formed the current day basin floor. This is evidenced by the hollow-like regolith materials on the basin floor associated with impact craters and their ejecta blankets. This may indicate the excavation of this potential sublimation deposit.

The regolith of the flow-like features includes smaller grain sizes than both basin floor regolith and hollows associated regolith. The smaller regolith grain sizes on the flows compared to the basin floor could explain the relative brightening of the flow-like features compared to the basin floor (**Figure 11**). However, flows from the peak ring were not isolated to the basin floor. The anomalous regions within the peak ring structure, associated with mesas within the peak ring, show regolith characteristics in common with the hollows material, indicative of volatile loss. These regions display similar single scattering albedos to the halos and are also some of the roughest units examined. The similar color properties of the inter-peak terrains to the basin floor suggests the photometric properties are related to grain size and compaction, and not composition. The color and photometric properties of these areas suggest that the lag from the VRL contains multiple compositional components, one of which is also common with the general regolith. This

suggests that the features in Raditladi Basin may capture an evolutionary sequence in regolith development and the mixing of volatiles within the upper crust. These findings are summarized in **Figure 21**.

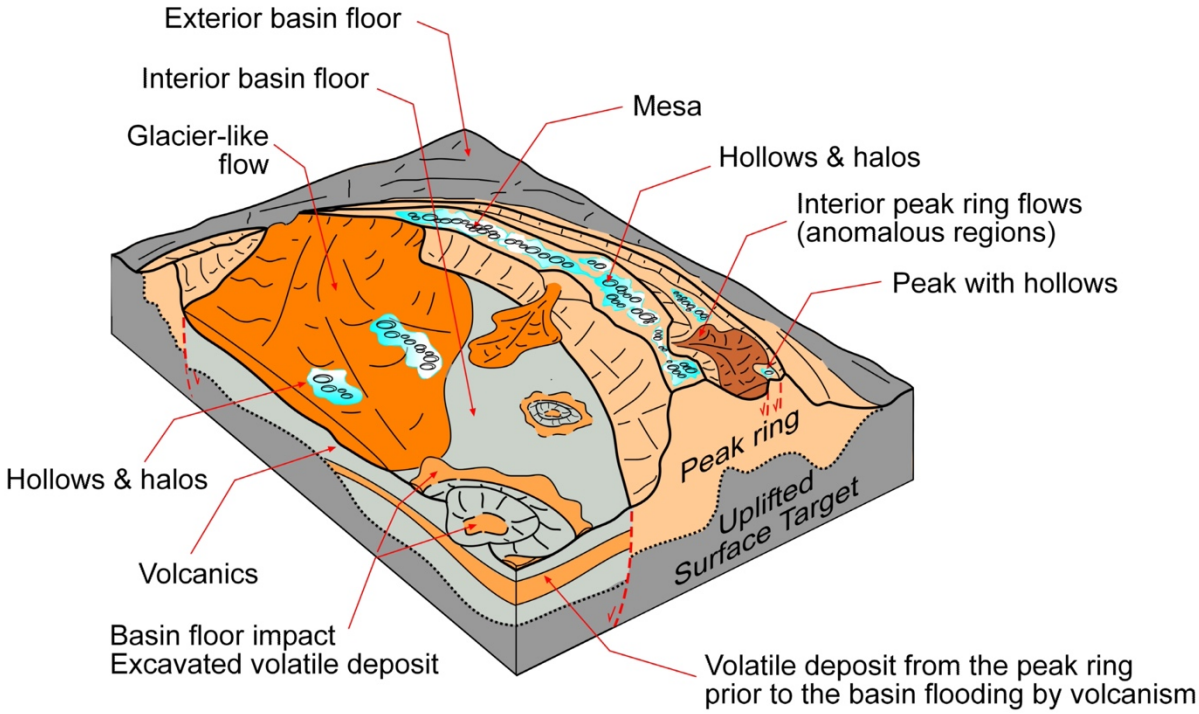

Figure 21. Schematic of the peak ring system (tan), flow-like features (dark orange), and basin floor (grey). The relationship between the interior basin floor (light grey), which displays the most distinctive photometric properties in the machine learning analyses, is used as the comparative regolith. The exterior basin floor (dark grey) is of similar composition but is comparatively more porous and contains larger regolith grains than the interior floor's regolith. Excavated materials from beneath the interior basin floor (light orange) show finer-grained, more compact characteristics than the interior floor commensurate with hollows regolith, suggesting the deposition of devolatilized material from the peak ring prior to basin floor flooding by volcanism and the subsequent emplacement of the glacier-like flows (Rodriguez et al. 2023). Hollows and their associated halos (bluish) are compositionally distinct, and their presence dominates the color properties of the mesas and hollow areas within the peak ring. The halos are finer-grained and more compact than all other units and the hollows have comparatively larger grains and more porous than the halos. The flow-like features (dark orange) show regolith properties intermixed between the interior basin floor and hollow, where the regolith is generally more compact and finer-grained than the interior basin floor. The interior peak ring flows, or anomalous regions, (brown) are also more fine-grained and porous than the interior basin floor, commensurate in regolith properties to the hollows and halos. The peak ring is uplifted material that forms a distinct surface feature.

References

Barraud, O., et al. 2023. Low sulfide concentration in Mercury's smooth plains inhibits hollows.

Sci. Adv. 9, eadd6452, doi:10.1126/sciadv.add6452
Barraud, O., et al. 2020. Near-Ultraviolet to Near-Infrared Spectral Properties of Hollows on Mercury: Implications for Origin and Formation Process. J. Geophys. Res. Planets 125 (12), doi:10.1029/2020JE006497
Barraud, O., et al., 2021. Spectral investigation of Mercury's pits' surroundings: Constraints on the planet's explosive activity. Icarus 370, doi:10.1016/j.icarus.2021.114652
Beck, P., et al. 2012. Photometry of meteorites. Icarus 218 (2012) 364–377
Besse, S., et al., 2020. Spectral Properties and Physical Extent of Pyroclastic Deposits on Mercury: Variability Within Selected Deposits and Implications for Explosive Volcanism JGR: Planets 125, doi:10.1029/e2018JE005879
Besse, S., et al. 2015. Spectroscopic properties of explosive volcanism within the Caloris basin with MESSENGER observations. JGR: Planets, 120, Issue 12, doi:10.1002/2015JE004819
Bickel, V.T., Deutsch, A.N., Blewett, D.T., Hollows on Mercury: Creation and analysis of a global reference catalog with deep learning. J. of Geophys. Res.: Machine Learning and Computation, 2, e2024JH000431.
Blair, D.M., et al. 2013. The origin of graben and ridges in Rachmaninoff, Raditladi, and Mozart basins, Mercury. J. Geophys. Res. – Planets, 118, 47–58.
Blewett, D.T. et al., 2011. Hollows on Mercury: MESSENGER evidence for geologically recent volatile-related activity. Science 333 (6051), 1856–1859.
Blewett, D.T. et al., 2013. Mercury's hollows: Constraints on formation and composition from analysis of geological setting and spectral reflectance. J. Geophys. Res. – Planets 118 (5), 1013–1032.
Blewett, D.T., et al., 2016. Analysis of MESSENGER high-resolution images of Mercury's hollows and implications for hollow formation. J. Geophys. Res. Planets, 121, 1798–1813, doi:10.1002/2016JE005070.
Blewett, DT., et al., 2018. Mercury's hollows In: Solomon, SC, Nittler LR, Anderson BJ (eds) Mercury: The View after MESSENGER. Cambridge University Press, Cambridge. Pp. 324 – 345.
Byrne, P.K., et al 2018. The Volcanic Character of Mercury In: Solomon, SC, Nittler LR, Anderson BJ (eds) Mercury: The View after MESSENGER. Cambridge University Press, Cambridge. Pp 287 – 323.
Chuang, F., et al., 2022. Mapping Lunar Swirls with Machine Learning: The Application of Unsupervised and Supervised Image Classification Algorithms in Reiner Gamma and Mare Ingenii Planetary Science Journal 3, number 10. Doi:10.3847/PSJ/ac8f43
Chuang, F. et al. Application of Machine Learning Techniques to Distinguish between Mare, Cryptomare, and Light Plains in Central Lunar South Pole−Aitken Basin 2025. Planetary Science Journal, Volume 6, Issue 2, id.35, 12 pp.
Cintala, M.J. 1992. Impact-Induced Thermal Effects in the Lunar and Mercurian Regoliths. JGR 97, No. E1, 947 – 973.
Clegg, R.N. et al., 2014. Effects of rocket exhaust on lunar soil reflectance properties. Icarus 227, 176 – 194.
Cord, A., Pinet, P., Daydou, Y., Chevrel, S., 2003. Planetary regolith surface analogs: optimized determination of Hapke parameters using multi-angular spectro-imaging laboratory data Icarus 165, 414–427.
Crosby, N. B., Aschwanden, M. J., and Dennis, B. R. 1993. Frequency distributions and correlations for solar X-ray flare parameters. Solar Physics 143 (2): 275-299. Doi:

10.1007/BF00646488
Curto, J. J., Castell, J., and Del Moral, F. 2016. Sfe: waiting for the big one. J. Space Weather Space Clim. 6, A23 https://doi.org/10.1051/swsc/2016018
Denevi, B.W. et al., 2016a. Final Calibration and Multispectral Map Products from the Mercury Dual Imaging System Wide-Angle Camera. Lunar Planet. Sci 47, abstract #1264. NASA/PDS.
Denevi, B.W., 2016b. The Geologic History of Mercury In: Solomon, SC, Nittler LR, Anderson BJ (eds) Mercury: The View after MESSENGER. Cambridge University Press, Cambridge. Pp 144 – 175.
Deutsch, A.N., Bickel, V.T., Blewett, D.T., 2025. Hollows on Mercury: Global Classification of Degradation States and Insight Into Hollow Evolution. JGR Planets 130, e2024JE008747.
Domingue, D.L., et al. 2002. Disk-Integrated Photometry of 433 Eros. Icarus 155, 205–219.
Domingue, D.L., et al., 2015. Mercury's global color mosaic: An update from MESSENGER's orbital observations. Icarus 257, 477 – 488, doi: 10.1016/j.icarus.2014.11.027
Domingue, D.L., et al., 2023. Spectrophotometric and Topographic Correlations within the Mare Ingenii Swirl Region: Evidence for a Highly Mobile Lunar Regolith. Planetary Science Journal 4:240, doi:10.3847/PSJ/ace433
Domingue, D.L., et al., 2024. Photometric Properties within the Reiner Gamma Swirl: Constraining Formation Mechanism. Planetary Science Journal 5:161, doi:103847/PSJ/ad2179
De Toffoli, B., et al. 2024. Hollows on Mercury: A Comprehensive Analysis of Spatial Patterns and Their Relationship to Craters and Structures. Earth and Space Sciences 11, doi:10.1029/2024EA003854
Evans, L.G. et al. 2015. Chlorine on the surface of Mercury: MESSENGER gamma-ray measurements and implications for the planet's formation and evolution. Icarus **257**, 417-427.
Evans, L.G., et al. 2012. Major-element abundances on the surface of Mercury: Results from the MESSENGER Gamma-Ray Spectrometer.. J. Geophys. Res., 117, E00L07, doi:10.1029/2012JE004178.
Foreman-Mackey, et al., 2013. emcee: The MCMC Hammer. arXiv:1202.3665, doi:10.48550/arXiv.1201.3665
Galiano, A. et al. 2022. Spectral identification of pyroclastic deposits on Mercury with MASCS/MESSENGER data. Icarus, Volume 388, article id. 115233, doi: 10.1016/j.icarus.2022.115233
Galiano, A., et al. 2024. Detection of a novel spectral feature at 830 nm in MDIS/MESSENGER color image of Praxiteles basin, Europlanet Science Congress 2024, Berlin, Germany, 8–13 Sep 2024, EPSC2024-220, https://doi.org/10.5194/epsc2024-220, 2024.
Goudge, T. A., et al., 2014. Global inventory and characterization of pyroclastic deposits on Mercury: New insights into pyroclastic activity from MESSENGER orbital data. J. Geophys. Res. Planets, 119, 635–658.
Hapke, B., 1981. Bidirectional Reflectance Spectroscopy 1. Theory. J. Geophys. Res. 68, 4571–4586.
Hapke, B., 1984. Bidirectional Reflectance Spectroscopy 3. Correction for Macroscopic Roughness. Icarus 59, 41–59.
Hapke, B., 1986. Bidirectional Reflectance Spectroscopy 4. The Extinction Coefficient and the Opposition Effect. Icarus 67, 264–280.
Hapke, B., 2002. Bidirectional Reflectance Spectroscopy 5. The Coherent Backscatter Opposition Effect and Anisotropic Scattering. Icarus 157, 523–534.

Hapke, B., 2008. Bidirectional reflectance spectroscopy 6. Effects of porosity Icarus 195, 918–926.
Hapke, B., 2012a. Theory of Reflectance and Emittance Spectroscopy. Cambridge University Press, NY, 2nd Edition, 513 pp.
Hapke, B., 2012b. Bidirectional reflectance spectroscopy 7 The single particle phase function hockey stick relation. Icarus 221, 1079 – 1083.
Head. J.W., et al. 2008. Volcanism on Mercury: Evidence from the First MESSENGER Flyby. Science, 321, 69 – 72, doi:10.1126/science.1159256
Helfenstein, P., and Shepard, M.K., 1999. Submillimeter-Scale Topography of the Lunar Regolith. Icarus 141, 107–131.
Hess, M., et al., 2023. Comparative photometric analysis of the Reiner Gamma swirl and Chang'e 5 landing site. A&A 674, A226.
Jozwiak, L.M., Head, J.W., Wilson, L., 2018. Explosive volcanism on Mercury: Analysis of vent and deposit morphology and modes of eruption. Icarus 302, doi:10.1016/j.icarus.2017.11.011
Klima, R.L., et al. 2018. Global Distribution and Spectral Properties of Low-Reflectance Material on Mercury. Geophys. Res. Lett. 45,2945–2953 (2018).
Leon-Dasi, M., et al., 2025. Timing of explosive volcanism on Mercury: A morphological and spectral analysis. Icarus 429, 116421.
Lucchetti, A., et al., 2018. Mercury Hollows as Remnants of Original Bedrock Materials and Devolatilization Processes: A Spectral Clustering and Geomorphological Analysis. J. Geophys. Res. (Planets) 123, 2365–2379 (2018).
Lucchetti, A., et al., 2021. Volatiles on Mercury: The case of hollows and the pyroclastic vent of Tyagaraja crater. Icarus 370, 114694.
Marchi, S. et al. 2009. A new chronology for the Moon and Mercury. Astron. J. 137, 4936–4948.
Marchi, S. et al. 2011. The effects of the target material properties and layering on the crater chronology: the case of Raditladi and Rachmaninoff basins on Mercury Planet. Space Sci. 59, 1968–1980.
McGuire, A., Hapke, B., 1995. An Experimental Study of Light Scattering by Large, Irregular Paeticles. Icarus 113, 134–155.
McGuire, R. E., and von Rosenvinge, T. T. 1984. The energy spectra of solar energetic particles. Advances in Space Research 4 (2-3): 117-125. https://doi.org/10.1016/0273-1177(84)90301-6
Meftah, M., et al., 2018. SOLAR-ISS: A new reference spectrum based on SOLAR/SOLSPEC observations. Astronomy & Astrophysics 611, A1. 10.1051/0004-6361/201731316
Nittler, L. R., et al., 2011. The Major-Element Composition of Mercury's Surface from MESSENGER X-ray Spectrometry. Science 333, 1847–1850, doi:10.1126/science.1211567.
Nittler, L.R., et al. 2018. The Chemical Composition of Mercury. In: Solomon, SC, Nittler LR, Anderson BJ (eds) Mercury: The View after MESSENGER. Cambridge University Press, Cambridge, pp 30-51
Nittler, L.R., and Weider, S.Z., 2019. The Surface Composition of Mercury. Elements: An International Magazine of Mineralogy, Geochemistry, and Petrology, 15(1), pp.33-38, DOI: 10.2138/gselements.15.1.33
Ogilvie, K. W., and Coplan, M. A. 1995. Solar wind composition. Reviews of Geophysics 33 (S1) 615-622. https://doi.org/10.1029/95RG00122
Pedregosa F., et al. 2011. Scikit-learn: Machine Learning in Python. J. Machine Learning Res. doi:10.48550/arXiv.1201.0490

1522 Pegg, D.L., et al. 2021. Explosive vent sites on Mercury: Commonplace multiple eruptions and
1523 their implications. Icarus 365, 114510.
1524 Peplowski, P. N., et al. 2012. Aluminum abundance on the surface of Mercury: Application of a
1525 new background-reduction technique for the analysis of gamma-ray spectroscopy data. J.
1526 Geophys. Res., 117, E00L04, doi: 10.1029/2012JE004181.
1527 Phillips et al. 2021. The Lifecycle of Hollows on Mercury: An Evaluation of Candidate Volatile
1528 Phases and a Novel Model of Formation. Icarus 114306
1529 Prockter, L. M., et al. (2010), Evidence for Young Volcanism on Mercury from the Third
1530 MESSENGER Flyby. Science, 329, 668–671, doi:10.1126/science.1188186.
1531 Reep, J. W., and Knizhnik, K. J., 2019. What Determines the X-Ray Intensity and Duration of a
1532 Solar Flare? The Astrophysical Journal, 874, 157. doi: 10.3847/1538-4357/ab0ae7
1533 Rodriguez, J.A.P., et al., 2020. The chaotic terrains of Mercury reveal a history of planetary
1534 volatile retention and loss in the innermost solar system. Nature Scientific Reports, 10, 4737,
1535 2020,
1536 Rodriguez, J.A.P., et al., 2023. Mercury's Hidden Past: Revealing a Volatile-dominated Layer
1537 through Glacier-like Features and Chaotic Terrains. Planetary Science Journal, 4:219
1538 doi:10.3847/PSJ/acf219
1539 Rothery, D.A., et al. 2021. On the asymmetry of Nathair Facula, Mercury. Icarus 355, 114180.
1540 Rothery, D.A, Thomas, R.J., Kerber, L., 2014. Prolonged eruptive history of a compound volcano
1541 on Mercury: Volcanic and tectonic implications. EPSL 358, doi:10.1016/j.epsl.2013.10.023
1542 Satopaa, V., et al. 2011. Finding a "Kneedle" in a Haystack: Detecting Knee Points in System
1543 Behavior. International Conference on Distributed Computing Systems Workshops 31, 166-
1544 171. doi:10.1109/ICDCSW.2011.20.
1545 Shepard, M., Helfenstein, P., 2007. A test of the Hapke photometric model. J. Geophys. Res. 112,
1546 E03001. http://dx.doi.org/10.1029/2005JE002625.
1547 Shkuratov, Y., Bondarenko, S., Kaydash, V., Videen, G., Munoz, O., Volten, H., 2007. J. Quant.
1548 Spectrosc. Radiat. Transf. 106, 487–508.
1549 Speyerer, E.J., Robinson, M.S., Sonke, A.J. 2022. Present Day Endogenic and Exogenic Activity
1550 on Mercury. GRL 49, e2022GL100783
1551 Stamnes, K. 2003. Ultraviolet Radiation. Pages 2467-2473 in Encyclopedia of Atmospheric
1552 Sciences, Academic Press. https://doi.org/10.1016/B0-12-227090-8/00444-9
1553 Strom, R.G., et al. 1975. Tectonism and volcanism on Mercury. J. Geophys. Res, 80, 2478 – 2507,
1554 doi:10.1029/JB080i017p02478.
1555 Strom, R. G. et al. 2008. Mercury Cratering Record Viewed from MESSENGER's First Flyby.
1556 Science 321, 79–81.
1557 Tandberg-Hanssen, E., and Emslie, A. G. 1988. The Physics of Solar Flares. Cambridge University
1558 Press.
1559 Taylor, L.A., et al. 2010. Mineralogical and chemical characterization of lunar highland soils:
1560 Insights into the space weathering of soils on airless bodies. JGR 115, E02002,
1561 doi:10.1029/2009JE003427.
1562 Thomas, R.J., et al., 2014a. Hollows on Mercury: Materials and mechanisms involved in their
1563 formation. Icarus 229, doi:10.1016/j.icarus.2013.11.018
1564 Thomas, R.J., et al., 2014b. Long-lived explosive volcanism on Mercury. Geophys. Res. Lett., 41,
1565 6084-6092, doi:10.1002/2014GL061224
1566 Thomas, R.J., et al. 2016. Mercury's low-reflectance material: Constraints from hollows. Icarus
1567 277, doi:10.1016/j.icarus.2016.05.036.

Vaughan et al. 2012. Hollow-forming layers in impact craters on Mercury: Massive sulfide or chloride deposits formed by impact melt differentiation. LPSC 43, id. 1187.

Vilas, F., et al. 2016. Mineralogical indicators of Mercury's hollows composition in MESSENGER color observations. Geophys. Res. Lett. 43,1450–1456 (2016).

Weider, S. Z. et al. 2015. Evidence for geochemical terranes on Mercury: Global mapping ofmajor elements with MESSENGER's X-Ray Spectrometer. Earth Planet. Sci. Lett. 416, 109-120 (2015).

Weider, S.Z., et al., 2016. Evidence from MESSENGER for sulfur- and carbon-driven explosive volcanism on Mercury. Geophys. Res. Lett., 43, 3653 – 3661, doi:10.1002/2016GL068325

Veronig, A., et al., 2002. Temporal aspects and frequency distributions of solar soft X-ray flares. Astronomy & Astrophysics 382, 1070-1080. Doi: 10.1051/0004-6361:20011694

Wu, Y., and Hapke, B., 2018. Spectroscopic observations of the Moon at the lunar surface. Earth Planet. Sci. Lett, 484, 145 – 153. doi:10.1016/j.epsl.2017.12.003

Xiao, Z. et al. (2013). Dark spots on Mercury: A distinctive low-reflectance material and its relation to hollows Journal of Geophysical Research: Planets, Volume 118, Issue 9, pp. 1752-1765

Acknowledgements. The work for this study was supported by Solar System Workings grant 80NSSC22K0099 and Discovery Data Analysis grant 80NSSC24K0066.

Appendix.

Data set. Tables of image data used in this study for each region. Photometric cubes were constructed for each of the images listed and are available in the Zenodo.

Table A1. Area I photometric imagery

Image name	Incidence	Emission	Phase	Resolution (m/pxl)
N0221023170M	27.28 – 90.00	0.12 – 65.44	89.48 – 90.60	15.51
N0233729090M	6.17 – 72.66	5.52 – 80.53	28.18 – 28.48	108.29
N0233814610M	3.76 – 70.74	0.06 – 68.24	27.70 – 28.05	75.50
N0251314913M	23.18 – 90.00	5.53 – 74.54	95.05 – 96.08	22.68
N0251314922M	26.96 – 89.99	5.17 – 69.00	94.60 – 95.30	22.98
N1013292097M	2.77 – 69.92	0.06 – 57.24	50.92 – 52.14	27.29
N1015454462M	19.46 0 89.99	2.41 – 73.47	91.77 – 92.48	37.09
N1015454698M	19.47 – 90.00	4.13 – 73.25	87.87 – 88.44	47.19
N1015483258M	20.54 – 90.00	0.22 – 69.44	88.51 – 89.27	35.79
N1015483484M	20.55 – 90.00	3.25 – 69.08	84.99 – 85.60	45.21
N1025680646M	23.35 – 90.00	0.03 – 52.87	47.38 – 48.13	37.90
N1025853410M	23.20 – 90.00	0.06 – 56.46	79.17 – 79.88	34.75
N1025853427M	33.10 – 90.00	0.08 – 50.31	78.63 – 79.21	35.38
N1045964008M	25.53 – 90.00	0.00 – 47.98	69.29 – 70.08	38.38
N1045992923M	24.56 – 90.00	0.02 – 44.92	65.95 – 66.53	37.97
N1045992946M	26.55 – 90.00	0.00 – 40.15	65.45 – 66.13	38.85
N1046021872M	25.63 – 90.00	0.00 – 41.42	61.78 – 62.55	39.01
W0215981346G	23.20 – 90.00	0.05 – 54.61	46.25 – 47.72	275.21
W0216024763G	23.20 – 90.00	0.02 – 47.41	61.06 – 62.75	259.04
W0218798458G	0.07 – 66.75	0.15 – 59.65	55.43 – 56.10	338.76
W0231179170G	23.20 – 90.00	0.01 – 54.80	57.36 – 59.05	132.87
W0231179208G	23.20 – 90.00	0.06 – 51.04	53.34 – 54.88	142.18
W0231222365G	23.20 – 90.00	0.04 – 51.37	68.28 – 69.92	132.62
W0249008821G	3.96 – 70.89	0.03 – 48.41	40.46 – 41.47	241.96
W0249037562G	3.18 – 70.26	0.01 – 44.77	39.42 – 40.37	256.76
W0249037617G	3.18 – 70.26	0.01 – 46.38	42.81 – 43.81	243.63
W0249037671G	3.18 – 70.26	0.03 – 52.74	46.95 – 47.98	235.89
W0249181883G	0.04 – 67.15	11.94 – 82.95	78.09 – 78.82	230.98
W0264217471G	3.75 – 70.72	0.00 – 55.27	49.28 – 50.42	207.78
W0264246178G	2.98 – 70.10	0.01 – 50.22	44.66 – 45.71	228.81
W0264246275G	2.98 – 70.10	0.03 – 55.26	52.35 – 53.45	207.60
W1013234498G	4.33 – 71.18	0.00 – 45.54	43.79 – 45.11	184.57

Table A2. Area II photometric imagery

Image name	Incidence	Emission	Phase	Resolution (m/pxl)
N0108826727M	33.48 – 90.0	7.77 – 67.70	60.64 – 60.75	254.47
N0108826792M	33.48 – 90.0	7.46 – 67.56	60.09 – 60.19	260.61
N0221023175M	36.37 – 89.37	2.75 – 54.14	89.85 – 90.72	15.64
N0233729090M	7.49 – 69.52	14.93 – 75.16	28.08 – 28.37	108.29
N0233814610M	5.98 – 67.66	0.25 – 59.86	27.67 – 28.02	75.50
N0251314922M	26.29 – 90.0	5.82 – 69.38	94.85 – 95.98	22.98
N0251314931M	38.65 – 85.80	9.37 – 56.15	94.50 – 95.01	23.27
N0251458976M	31.09 – 90.0	0.01 – 35.38	65.39 – 66.50	21.55
N1013292093M	5.42 – 66.74	0.03 – 51.03	51.55 – 52.13	27.59
N1013292097M	5.42 – 67.03	0.13 – 51.14	51.41 – 52.14	27.29
N1015454698M	26.17 – 90.0	6.40 – 69.25	88.28 – 88.59	47.19
N1015483484M	27.08 – 89.99	2.22 – 65.10	85.34 – 85.74	45.21
N1025651792M	34.95 – 90.0	0.39 – 54.40	45.32 – 45.84	36.61
N1025651796M	29.06 – 90.0	0.05 – 54.26	44.84 – 45.60	37.02
N1025680646M	35.04 – 89.99	0.10 – 46.09	47.56 – 48.80	37.90
N1025680666M	35.11 – 90.0	0.07 – 47.97	46.95 – 47.67	38.55
N1025853427M	28.82 – 90.0	0.06 – 50.00	78.56 – 79.38	35.38
N1045964008M	26.56 – 90.0	0.03 – 43.61	69.49 – 70.26	38.38
N1045992946M	27.53 – 90.0	0.00 – 38.83	65.61 – 66.40	38.85
N1046021872M	28.51 – 90.0	0.00 – 35.27	61.98 – 62.72	39.01
N1046021896M	28.51 – 889.99	0.01 – 33.86	61.72 – 62.22	39.92
W0215981346G	30.27 – 90.00	0.06- 59.48	47.23 – 48.73	275.21
W0216024763G	30.27 – 90.00	0.03 – 47.23	62.26 – 63.49	259.04
W0216024811G	30.27 – 90.00	0.03 – 48.77	57.47 – 58.98	273.82
W0216068263G	41.98 – 89.86	0.02 – 32.58	69.10 – 70.47	132.87
W0231179170G	30.27 – 90.00	0.03 – 54.36	58.68 – 60.37	142.18
W0231179208G	30.27 – 90.00	0.02 – 53.15	54.42 – 55.99	132.62
W0231222365G	41.95 – 90.00	0.08 – 35.55	69.46 – 70.84	202.50
W0249008821G	3.91 – 77.02	0.00 – 46.11	41.59 – 42.60	241.96
W0249037562G	3.04 – 76.18	0.00 – 39.56	40.37 – 41.33	256.76
W0249037617G	3.04 – 76.18	0.02 – 44.98	43.88 – 44.88	243.63
W0249037671G	3.04 – 76.17	0.07 – 51.30	48.11 – 49.14	235.89
W0249066345G	2.21 – 75.33	0.02 – 42.56	42.52 – 43.44	261.58
W0249181883G	0.68 – 71.86	21.17 – 80.92	78.94 – 79.68	230.98
W0264188574G	4.57 – 77.64	0.00 – 44.56	39.64 – 40.29	207.78
W0264217471G	3.68 – 76.80	0.19 – 54.06	50.77 – 51.56	228.81
W0264246178G	2.82 – 75.96	0.01 – 43.55	45.69 – 46.75	207.60
W1013234498G	4.32 – 77.40	0.02 – 44.85	45.16 – 46.48	184.57
W1056138397G	30.34 – 90.00	2.66 – 63.41	77.36 – 78.28	240.04
W1056167536G	30.31 – 90.00	1.30 – 61.98	80.69 – 81.57	238.27

Table A3. Area III photometric imagery

Image name	Incidence	Emission	Phase	Resolution (m/pxl)
N0108826727M	30.43 – 89.99	0.06 – 48.61	47.26 – 48.03	254.47
N0108826792M	30.43 – 89.99	0.06 – 48.61	47.26 – 48.03	260.61
N0220979975M	34.97 – 87.31	13.80 – 64.75	98.96 – 100.07	16.86
N0233687955M	7.26 – 80.45	0.26 – 65.53	27.47 – 28.08	47.17
N0233729090M	6.14 – 79.29	7.74 – 68.63	28.07 – 28.36	108.29
N0233814610M	3.70 – 76.82	0.21 – 55.83	27.77 – 28.12	75.50
N0251314931M	38.03 – 85.91	10.13 – 57.00	94.39 – 95.38	23.27
N0251458976M	25.43 – 90.00	0.00 – 42.15	65.39 – 66.45	21.55
N0251458985M	37.34 – 89.96	0.00 – 28.60	64.96 – 65.73	21.81
N1025651792M	30.49 – 90.00	0.10 – 55.48	45.48 – 46.27	36.61
N1025651796M	45.14 – 79.39	2.64 – 38.77	45.24 – 45.83	37.02
N1025680666M	30.43 – 89.99	0.06 – 48.61	47.26 – 48.03	38.55
N1025853427M	30.27 – 89.99	0.10 – 49.44	78.93 – 79.71	35.38
N1025853445M	37.82 – 89.96	0.05 – 42.22	78.35 – 78.96	36.05
N1045964008M	20.97 – 89.97	0.01 – 49.80	69.54 – 70.16	38.38
N1045964032M	33.17 – 85.20	0.01 – 37.43	69.05 – 69.67	39.30
N1045992946M	21.90 – 9000	0.00 – 45.33	65.57 – 66.30	38.85
N1045992971M	34.0 – 86.235	0.00 – 31.89	65.25 – 65.69	39.80
N1046021896M	22.85 – 90.00	0.00 – 41.18	61.62 – 62.37	39.92
W0215981346G	28.82 – 90.00	0.05 – 51.18	46.56 – 48.02	275.21
W0216024763G	28.82 – 90.00	0.02 – 43.02	61.47 – 63.14	259.04
W0216024811G	28.82 – 90.00	0.01 – 39.91	56.85 – 58.29	273.82
W0231179170G	28.82 – 90.00	0.14 – 50.31	57.85 – 59.52	273.18
W0231179208G	28.82 – 90.00	0.08 – 46.56	53.70 – 55.23	132.87
W0231222365G	28.81 – 90.00	0.05 – 45.31	68.68 – 70.30	142.18
W0231567980G	36.71 – 90.00	31.65 – 92.41	128.79 – 129.13	132.62
W0249008821G	6.10 – 67.78	0.00 – 42.86	40.98 – 41.99	241.96
W0249037562G	5.63 – 67.29	0.00 – 38.32	39.84 – 40.79	256.76
W0249037617G	5.63 – 67.29	0.02 – 39.72	43.29 – 44.30	243.63
W0249037671G	5.63 – 67.29	0.04 – 45.85	47.49 – 48.52	235.89
W0249066345G	8.28 – 64.80	0.10 – 36.71	42.02 – 42.93	261.58
W0249181883G	3.38 – 65.02	13.81 – 75.94	78.47 – 79.23	230.98
W0264217471G	5.97 – 67.65	0.05 – 48.34	49.88 – 51.02	228.28
W0264246178G	5.53 – 67.16	0.00 – 44.00	45.10 – 46.16	207.78
W0264246275G	5.53 – 67.16	0.05 – 48.09	52.90 – 53.89	228.81
W1013234498G	6.32- 68.04	0.01 – 40.18	44.40 – 45.72	184.57
W1056138397G	28.89 – 90.00	0.03 – 56.24	76.92 – 77.84	240.04
W1056167536G	28.86 – 90.00	0.10 – 55.52	80.27 – 81.15	238.27

Data Quality.

The MDIS imaging data only contained observations in the backward and forward scattering regimes for all three sites. Following the methodology of Domingue et al. (2023, 2024), the quality

of the data coverage in the incidence and emission angle values was examined (See Figures A2 – A4), for both the backward and forward scattering regimes were examined by grouping the observations into 5-degree bins for all three photometric angles. The number of data points in each bin was counted and the percentage of bins with data points was mapped (**Figs. A2 – A4**).

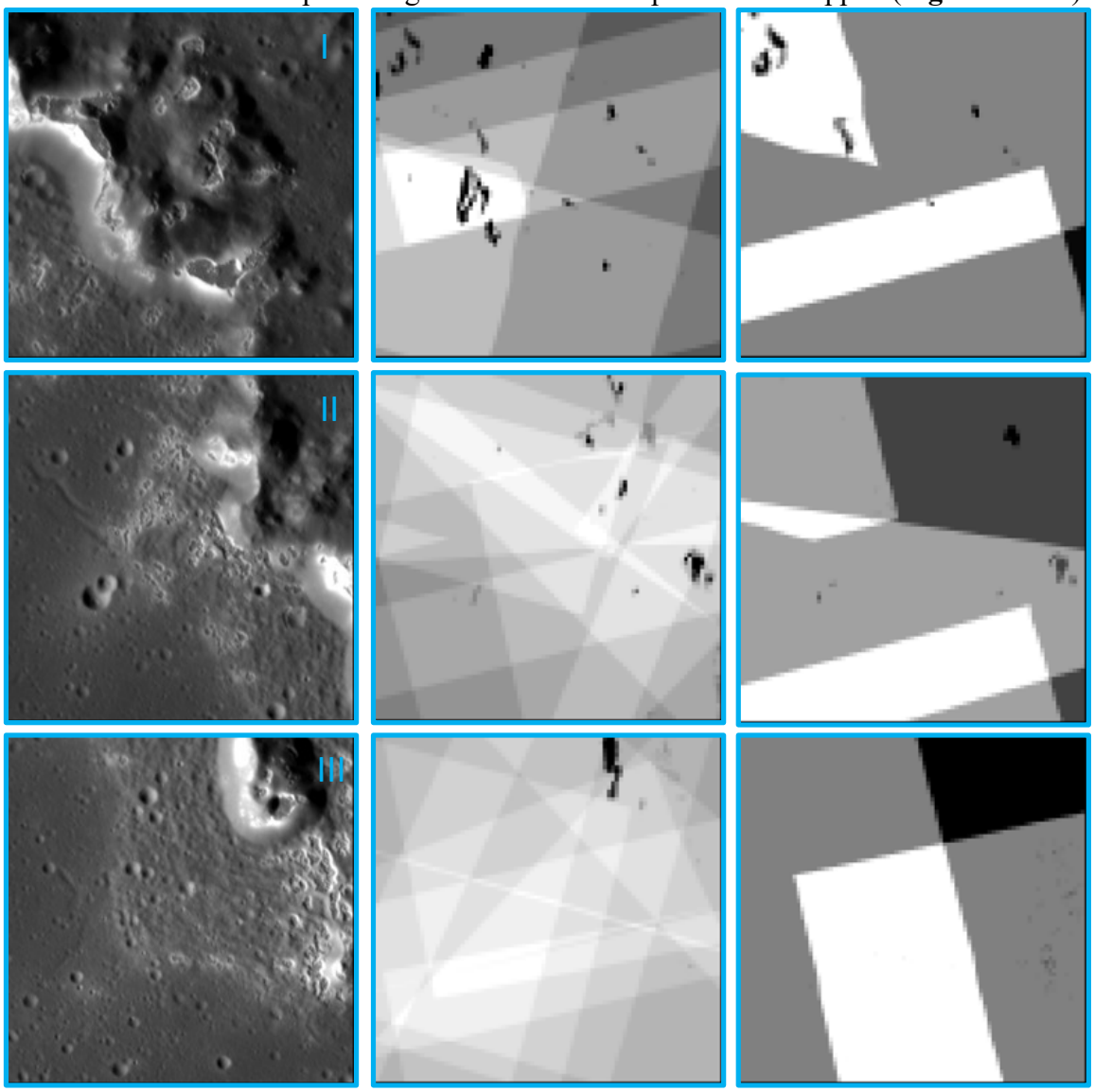

Figure A1. Data point coverage for Areas I (top row), II (center row), and II (bottom row), shown in grey scale with lower numbers darker and higher numbers brighter. An image of the area is shown in the left column, north upwards. Backward scattering regime data counts are displayed in the center column, forward scattering data counts are displayed in the right column. Data counts in Area I range from 1800 – 2900 and 14 – 300 in the backward and forward scattering regimes, respectively. Data counts in Area II range from 1700 – 3300 and 0 – 300 in the backward and forward scattering regimes, respectively. Data counts in Area III range from 1500 – 3207 and 0 – 200 in the backward and forward scattering regimes, respectively.

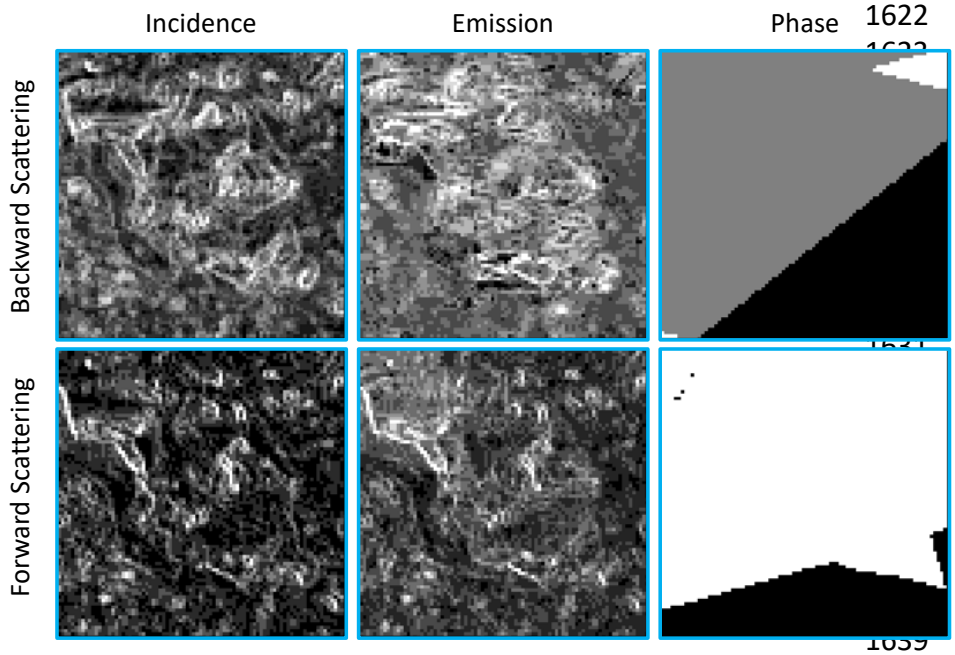

Figure A2. Data coverage maps displaying the percentage of angular bins with data points across Area I. Lower to higher values are represented by darker to lighter shades of grey, respectively. The top row displays the backward scattering regime and the bottom row displays the forward scattering regime. The columns, from left to right, display the percent coverage in incidence, emission, and phase angle. The range of percentage values in the backward scattering regime are 16.7 – 100, 33.3 – 94.4, and 64.3 – 78.6, respectively. The range of percentage values in the forward scattering regime are 5.6 – 55.6, 5.6 – 61.1, and 5.6 – 11.1, respectively.

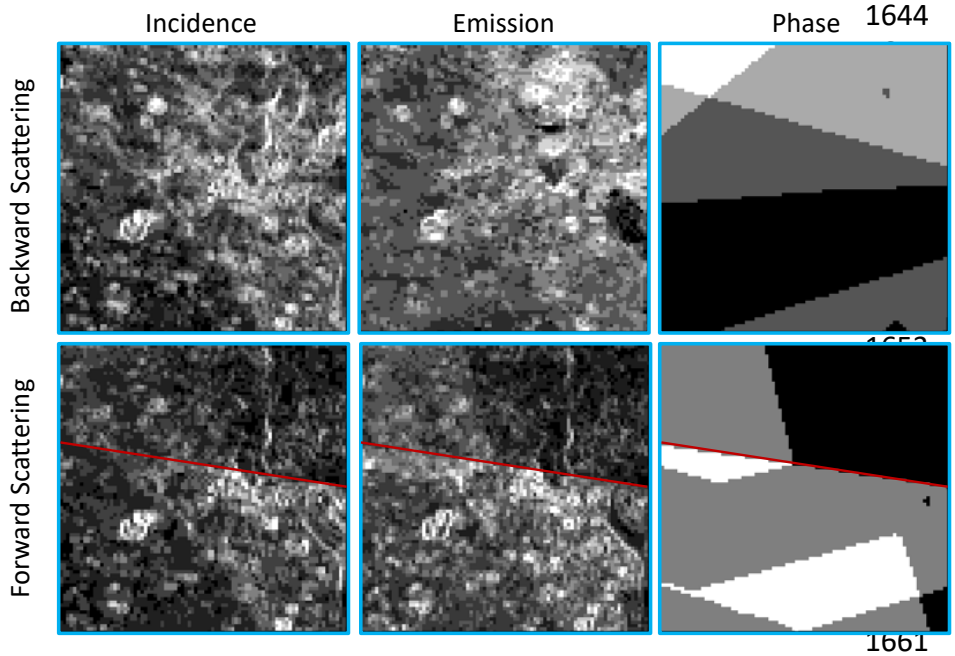

Figure A3. Data coverage maps displaying the percentage of angular bins with data points across Area II. Lower to higher values are represented by darker to lighter shades of grey, respectively. The top row displays the backward scattering regime and the bottom row displays the forward scattering regime. The columns, from left to right, display the percent coverage in incidence, emission, and phase angle. The range of percentage values in the backward scattering regime are 22.2 – 94.4, 33.3 – 83.3, and 50.0 – 85.7, respectively. The range of percentage values in the

forward scattering regime are 0 – 66.7, 0 – 77.8, and 0 – 16.7, respectively. The red line marks a boundary in angle coverage that affects the modeling results, as discussed in the 'Photometric Modeling Results' section. A larger angle range, representing better coverage, is present below the red line.

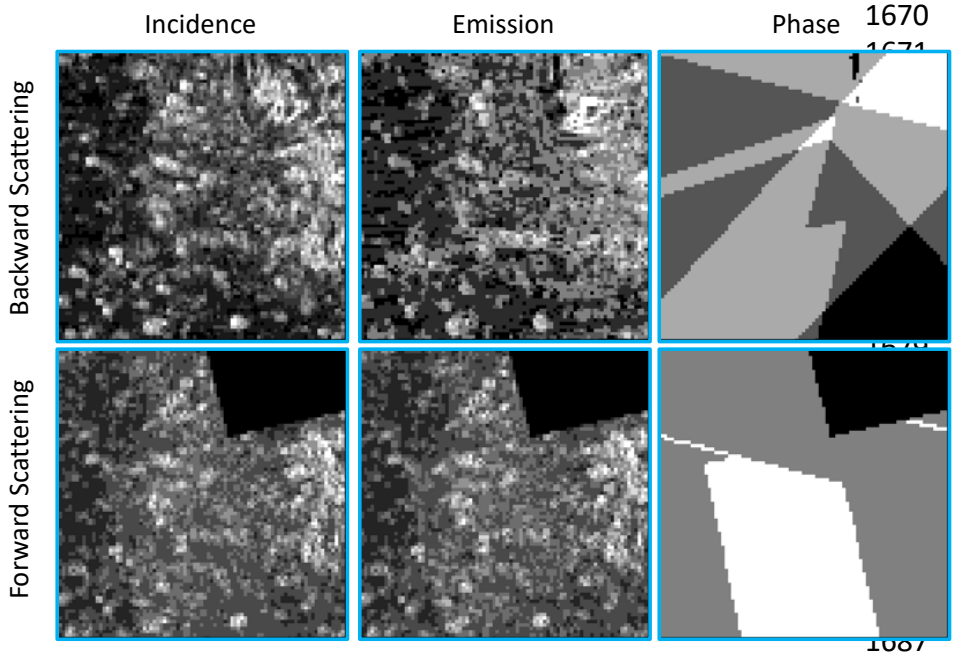

Figure A4. Data coverage maps displaying the percentage of angular bins with data points across Area III. Lower to higher values are represented by darker to lighter shades of grey, respectively. The top row displays the backward scattering regime and the bottom row displays the forward scattering regime. The columns, from left to right, display the percent coverage in incidence, emission, and phase angle. The range of percentage values in the backward scattering regime are 22.2 – 100, 38.9 – 94.4, and 57.1 – 78.6, respectively. The range of percentage values in the forward scattering regime are 0 – 55.6, 0 – 50, and 0 – 11.1, respectively.

Framework for Interpreting Results

Photometry is the study of reflected light that has been scattered by a medium, in this case a planetary regolith. Models assist in deriving physical properties of the scattering medium (regolith), but these properties are limited to the depth to which the light interacts (the optically active portion of the regolith). Different wavelengths probe to different depths, and the visible range probes to depths of a few micrometers to millimeters, depending on the opacity of the regolith material. In the case of Hapke's model, the physical properties of the optically active portion of the regolith can be interpreted from the single scattering albedo, surface roughness, and single particle scattering amplitude parameters. These interpretations allow for comparative examination of granular structures in addition to inter-grain structures. The interpretation of these properties is constrained by the color or spectral properties of the surface.

The single scattering albedo, w, is controlled by the composition, grain size, and compaction/porosity of the surface (e.g., Hapke 2012a). Smaller grain sizes, within compositionally similar regolith, can produce a higher w value. Alternatively, the removal of fine-grains and the destruction of the porous, fairy-castle structure (i.e., compaction, c_m, of the surface, where $c_m = 1 - \rho$, with ρ = porosity) of the lunar regolith has been shown to increase the surface reflectance, and thus the single scattering, albedo (Clegg et al. 2014, Wu and Hapke 2018, Hess et al. 2023). While it has not been firmly established how similar the structures within Mercury's

regolith are to the lunar regolith, differences in both inter-grain and granular structures will produce the same relative effects on both bodies. To determine if grain size or compaction are contributing to albedo differences between units will require examination of the other photometric parameters in addition to examination of the color or spectral properties.

Grain size and compaction also control the surface roughness parameter, $\overline{\theta}$, values. The surface roughness parameter is defined as a measure of the average surface tilt over scales from a few grain diameters to the footprint size or resolution of the detector (e.g., Hapke 2012a). The surface tilt, on the scale of grain diameters, is dependent on the pore space between particles (porosity), which in turn is influenced by grain size (are smaller grains infilling the pores, or are larger grains more closely packed). An illustration of this is provided in the Appendix (**Fig. A5**). Comparisons of trends with w and $\overline{\theta}$ can place boundaries on the grain size and compaction differences between surfaces.

The single particle scattering amplitude, b, is governed by how the individual grains scatter light, which in turn is controlled by the shape and internal structure of the grain. The mathematical correlation between b and the single particle scattering partition parameter, c, is based on laboratory measurements and applications of this function and model to other solar system objects (e.g. Hapke 2012b). The relationship shows that lower values of b correlate with more opaque, irregularly shaped, and rougher surfaced grains. This allows for the comparison of grains in terms of internal structures, which are often correlated to either processing or formation of the surface.

Roughness and surface tilt.

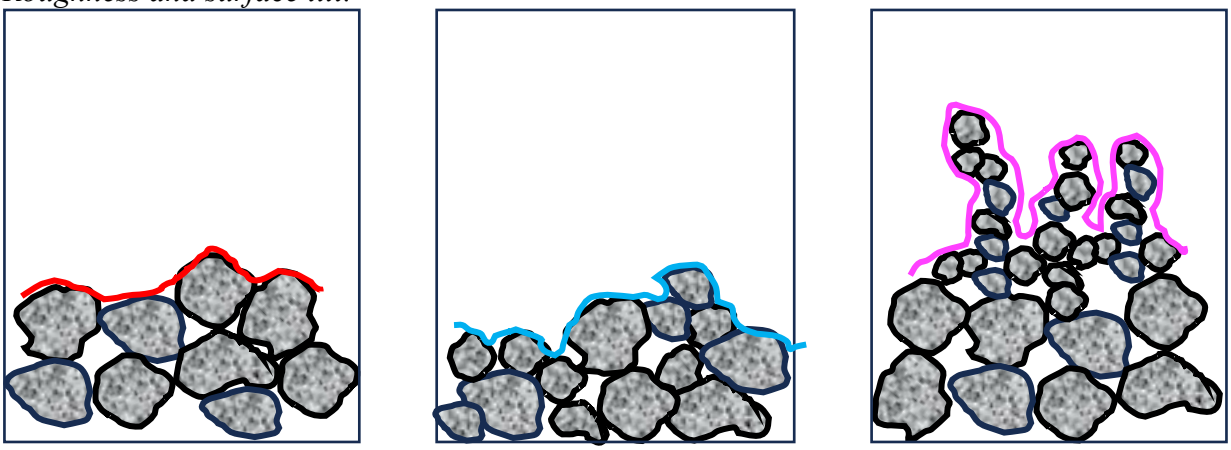

Figure A5. An illustration of how surface tilts vary on the scale of grain sizes with variation in grain size and porosity in a regolith. The scenario on the left represents larger, compact grains, whereas the scenario on the right represents the fairy-castle structure of the lunar regolith. The central diagram shows an intermediate, multiple grain size, compact scenario. The colored lines represent the shape of the topography that influences the photometric behavior of the surface.

Photometric Parameter Maps

The mapping of the individual Hapke model parameters for each area are shown in **Figures A6 – A8**, with each figure using the same grey-scale for each parameter (different grey-scales per parameter, but same scale from figure to figure for each parameter) to facilitate comparisons between regions.

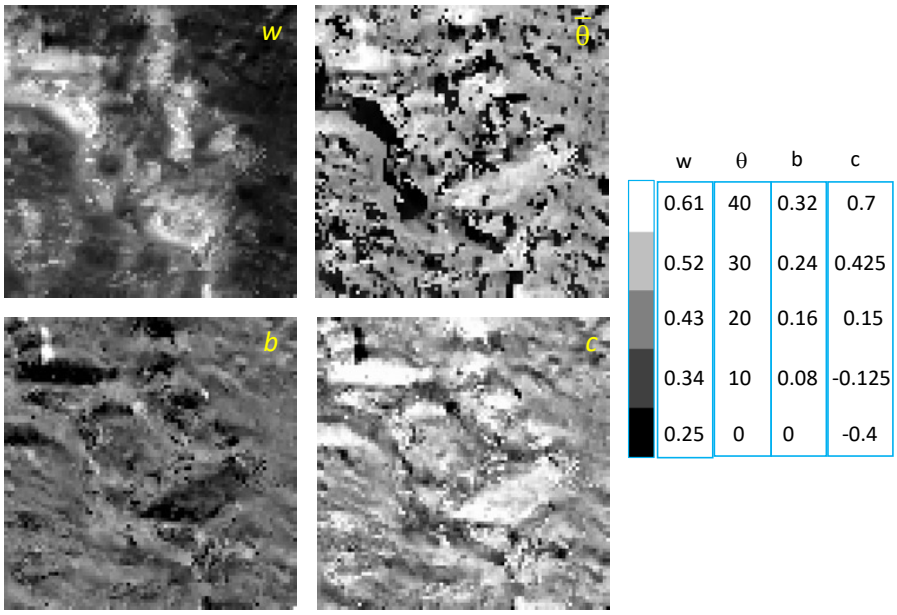

Figure A6. Mapping of the single scattering albedo (top left), surface roughness (top right), scattering function amplitude (bottom left), and scattering function partition parameters (bottom right) for area I. The grey scale represents values from low (dark) to high (bright). The table displays the grey-scale for each of the parameter maps.

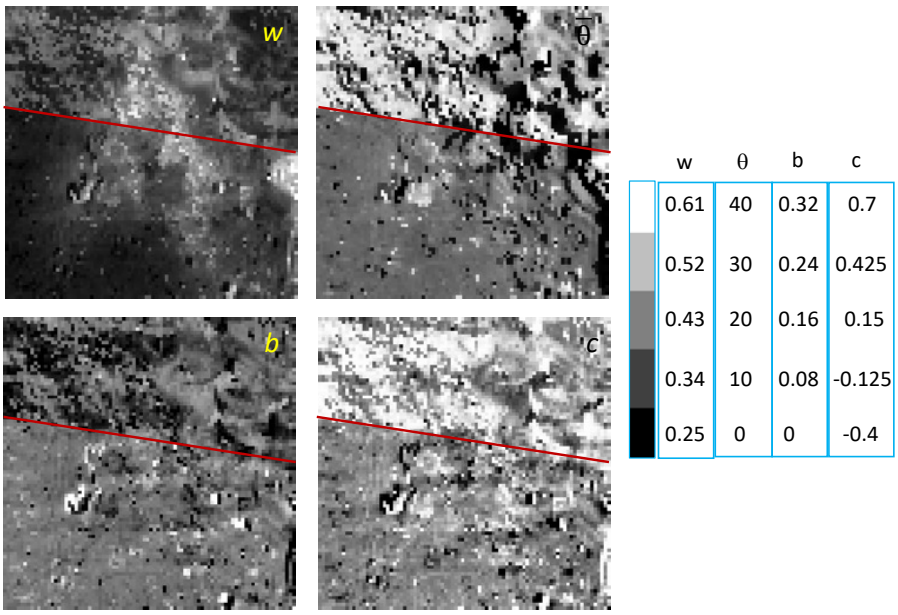

Figure A7. Mapping of the single scattering albedo (top left), surface roughness (top right), scattering function amplitude (bottom left), and scattering function partition parameters (bottom right) for area II. The grey scale represents values from low (dark) to high (bright). The table displays the grey-scale for each of the parameter maps. The red line shows a transition in angle coverage (see Fig. A3) that affects the parameter solutions (less coverage in the forward scattering direction). The area below the red line has the better angular coverage within the data set.

Figure A8. Mapping of the single scattering albedo (top left), surface roughness (top right), scattering function amplitude (bottom left), and scattering function partition parameters (bottom right) for area III. The grey scale represents values from low (dark) to high (bright). The table displays the grey-scale for each of the parameter maps.

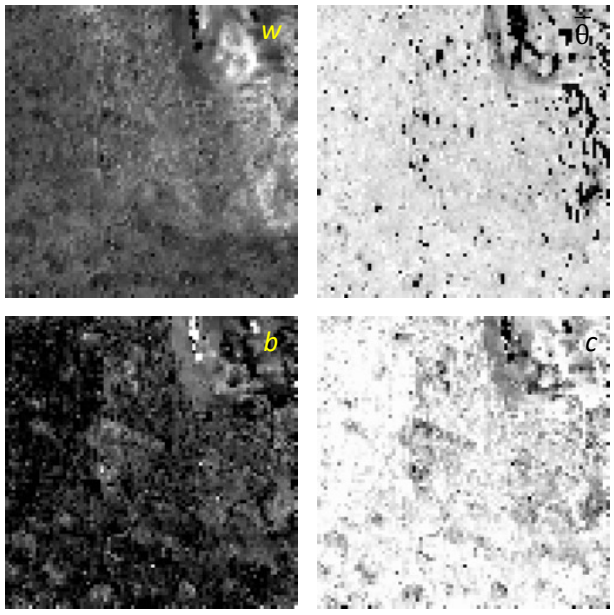

w	θ	b	c
0.61	40	0.32	0.7
0.52	30	0.24	0.425
0.43	20	0.16	0.15
0.34	10	0.08	-0.125
0.25	0	0	-0.4

Bayesian Model Solutions

Example Solutions

Area I

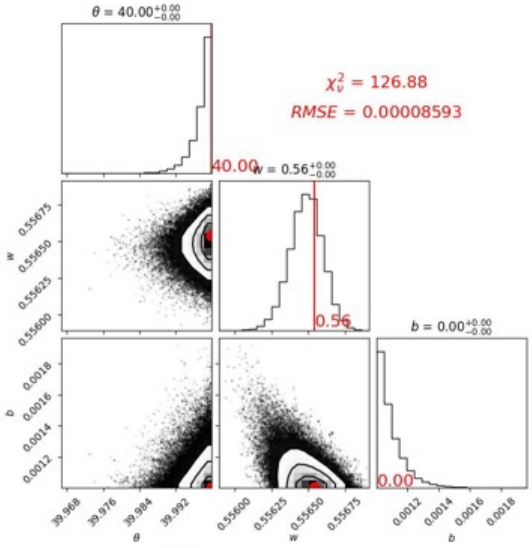

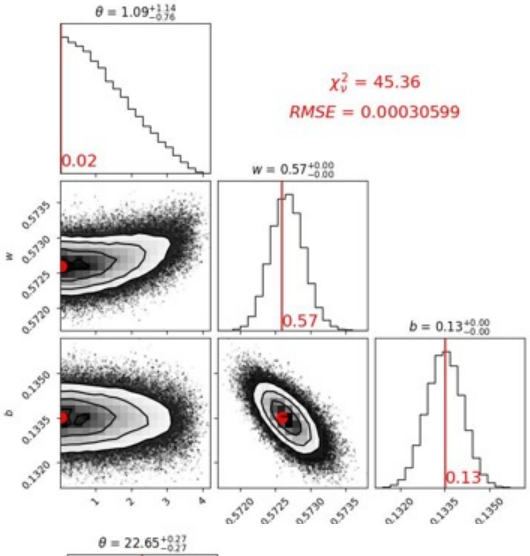

Area II

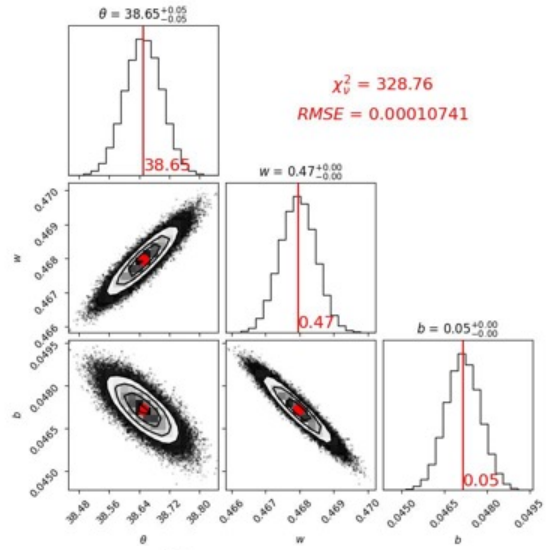

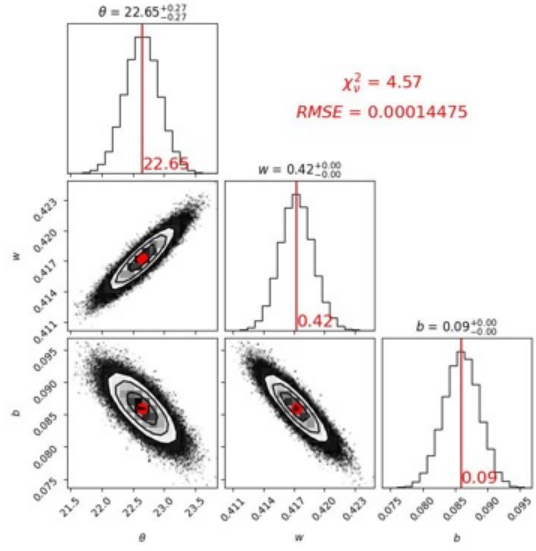

Area III

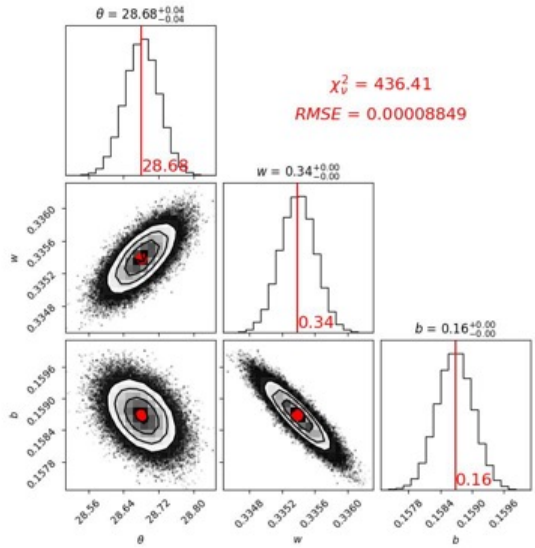

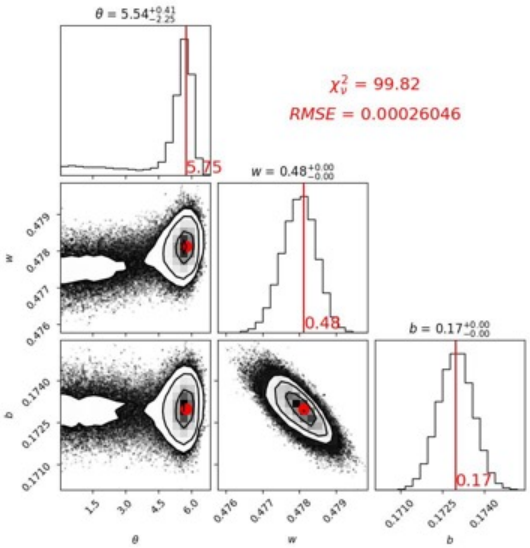

1803

*Figure **A9**. Examples of model solutions from locations in Area I (top), Area II (center), and Area III (bottom).*

Quality of Model Fits.

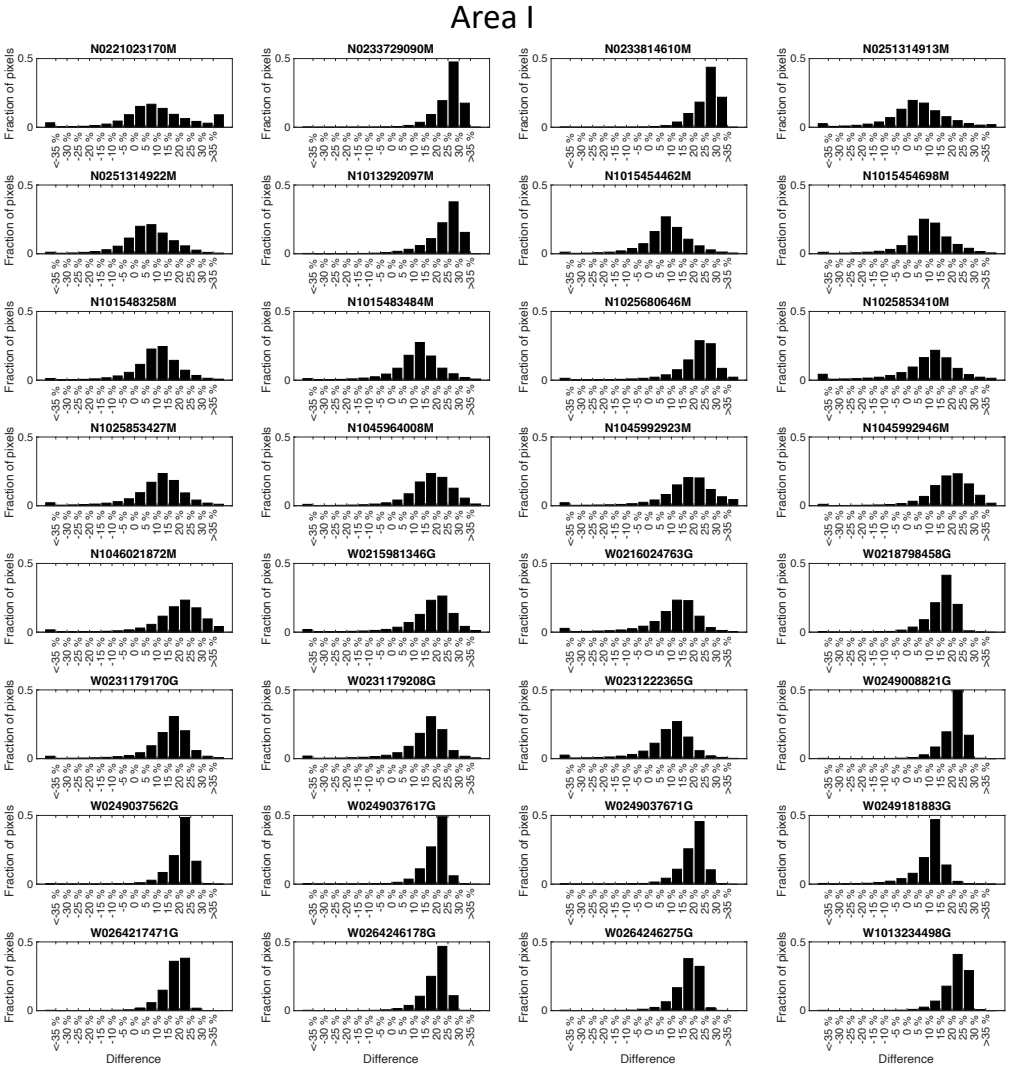

*Figure **A10**. Histograms of Area I showing the percent differences for all images all used to model the reflectance behavior in terms of the fraction of pixels from the total in each percent difference category.*

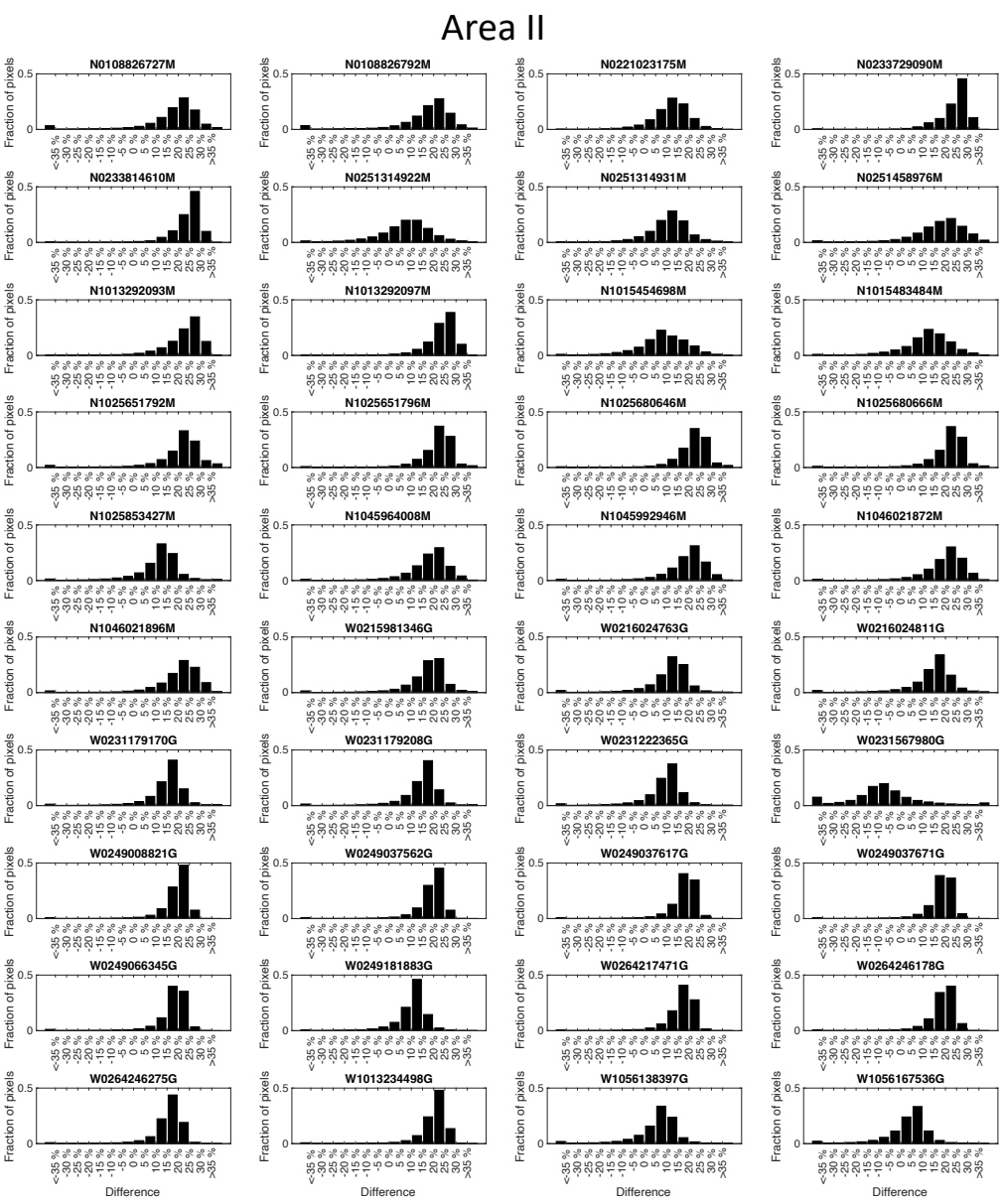

*Figure **A11**. Histograms of Area II showing the percent differences for all images all used to model the reflectance behavior in terms of the fraction of pixels from the total in each percent difference category.*

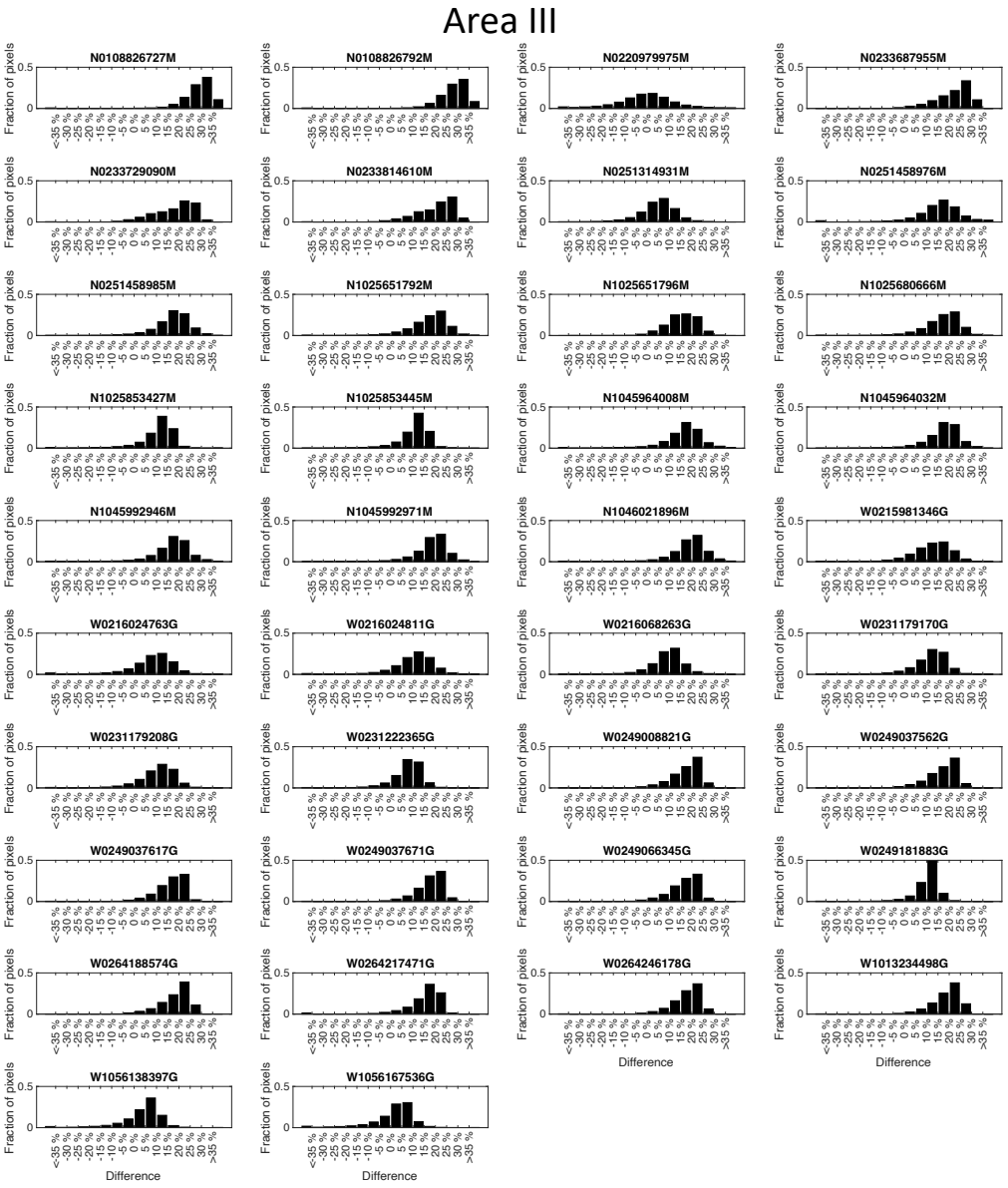

*Figure **A12**. Histograms of Area III showing the percent differences for all images all used to model the reflectance behavior in terms of the fraction of pixels from the total in each percent difference category.*

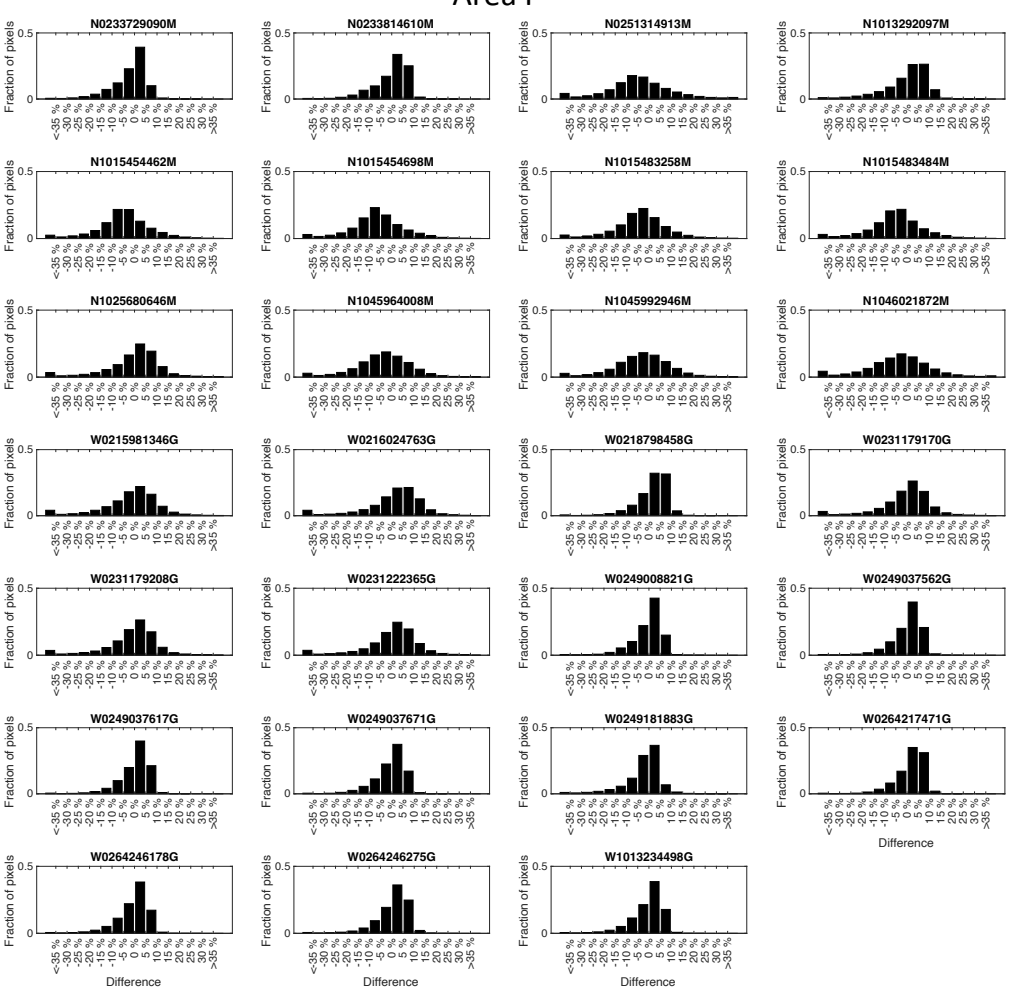

*Figure **A13**. Histograms of Area I showing the percent differences of normalized reflectance from all images used to model the reflectance behavior in each area in terms of the fraction of pixels from the total in each percent difference category.*

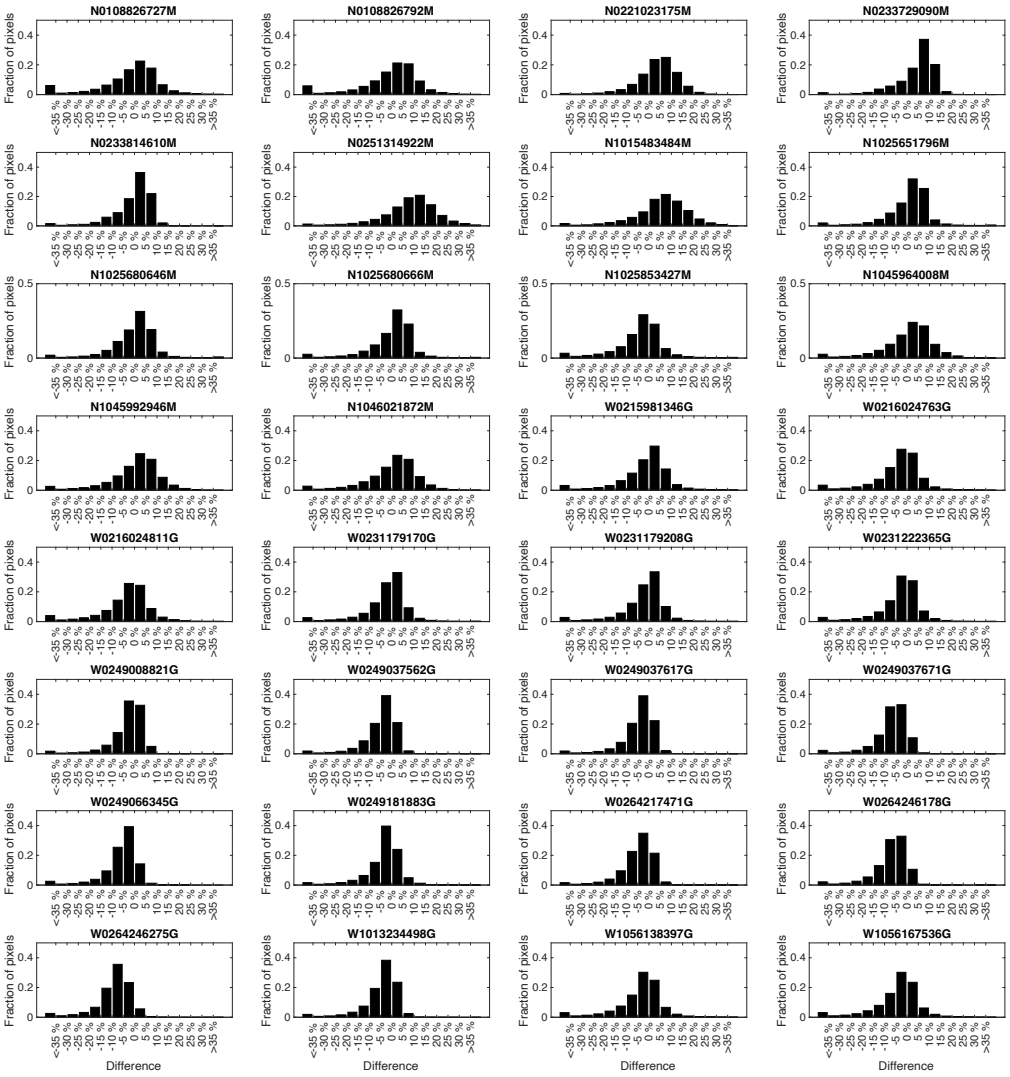

*Figure **A14**. Histograms of Area II showing the percent differences of normalized reflectance from all images used to model the reflectance behavior in each area in terms of the fraction of pixels from the total in each percent difference category.*

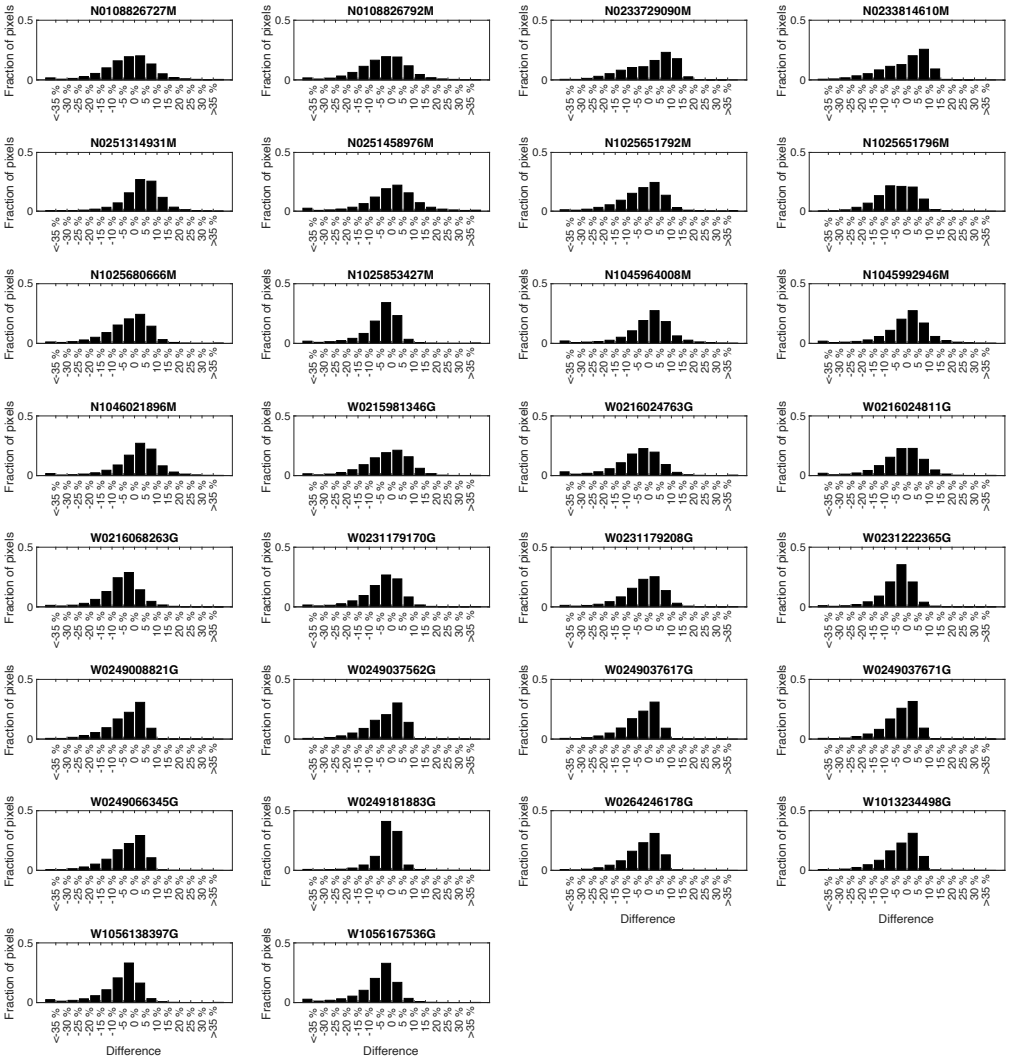

*Figure **A15**. Histograms of Area III showing the percent differences of normalized reflectance from all images used to model the reflectance behavior in each area in terms of the fraction of pixels from the total in each percent difference category.*